

Impact of severe convection on the water vapor mixing ratio in the extra-tropical stratosphere

Dissertation

zur Erlangung des Grades
Doktor der Naturwissenschaften (Dr. rer. nat.)

von
Dina Khordakova

vorgelegt am 11. Februar 2022 an der

Bergischen Universität Wuppertal
Fakultät für Mathematik und Naturwissenschaften
Institut für Atmosphären und Umweltforschung

Abstract

The emission of anthropogenic greenhouse gases leads to a continuous increase in average global surface temperatures. The radiative effect of the anthropogenic sources is amplified by feedback processes, like the water vapor feedback. The rapid change in climatic conditions is evident not only in the mean of the relevant weather parameters, but also in the severity and frequency of extreme events. Extreme convective events in the troposphere not only have immediate impacts on the surface, they can also influence the dynamics and composition of the stratosphere. One major impact is the moistening of the stratosphere by the transport of tropospheric air masses by overshooting convection and pyro-convection. This effect plays a crucial role in climate feedback as small changes of water vapor mixing ratios in the upper troposphere and lower stratosphere (UTLS) have a large impact on the radiative budget of the atmosphere and hence have an additional positive feedback on the changing climate.

In this thesis four cases are investigated in which water vapor was injected into the stratosphere. Two of them are cases of convective overshooting and two are cases of pyro-convection. In all of these cases, unusual values of water vapor were measured in the stratosphere and a persistent dynamical signature (potential vorticity anomaly) was produced. For the convective case, the measurements were made by the Cryogenic Frostpoint Hygrometer (CFH) which requires Trifluoromethane (R-23) as a cooling agent. Since the year 2020, R-23 has not been acquirable in Europe. Hence, an alternative cooling method for the instrument was successfully explored and tested.

The two cases of convective overshooting were investigated on two consecutive days in the European mid-latitudes in early summer of 2019. Using balloon-borne instruments, measurements of convectively injected water vapor in the stratosphere were performed. The magnitude of the affected stratospheric water vapor reached up to 12.1 ppmv with an estimated background value of 5 ppmv. The corresponding water vapor values measured by the Microwave Limb Sounder (MLS) satellite in the lower stratosphere (LS) are lower than the in-situ observations and the fifth generation of ECMWF atmospheric global reanalysis (ERA5) reanalysis overestimated water vapor mixing ratios. Backward trajec-

tories of the measured injected air masses reveal that the moistening of the LS took place several hours before the balloon launch. This is in good agreement with the reanalysis which shows a strong change in the structure of isotherms and a sudden and short-lived increase in potential vorticity. Similarly, further satellite data show low cloud top brightness temperatures during the overshooting event, which indicates an elevated cloud top height.

The two pyro-convective cases caused by the wild fires in the year 2017 in Canada and in the year 2019/2020 in Australia lead to water vapor mixing ratios of up to 19 ppmv and 20 ppmv at 100 hPa with background values at ≈ 5 ppmv. The plumes reached pressure levels of 38 hPa and 12 hPa, respectively, as measured by MLS. The impact of these fires is also evident in the ECMWF ERA5 reanalysis as an individual vortex (enhanced relative vorticity) which was continuously heated due to black carbon loading. This caused the strong rise of the plumes within the stratosphere and prevented the dilution leading to particularly long survival times. In contrast to the convective cases, ERA5 does not show elevated water vapor values associated with the air masses impacted by the forest fires.

Zusammenfassung

Der Ausstoß von anthropogenen Treibhausgasen führt zu einem kontinuierlichen Anstieg der durchschnittlichen globalen Temperaturen in Bodennähe. Die rasche Veränderung der klimatischen Bedingungen zeigt sich nicht nur im Mittelwert der relevanten Wetterparameter, sondern auch in der Schwere und Häufigkeit von Extremwetterereignissen. Extreme, konvektive Ereignisse in der Troposphäre haben nicht nur unmittelbare Auswirkungen auf die Erdoberfläche, sie können auch die Dynamik und Zusammensetzung der Stratosphäre beeinflussen. Eine wichtige Auswirkung ist die Befeuchtung der Stratosphäre durch den Transport von troposphärischen Luftmassen, verursacht durch überschießende Wärmekonvektion und Pyrokonvektion. Dieser Effekt spielt eine entscheidende Rolle bei der Klimarückkopplung, da bereits kleine Änderungen des Mischungsverhältnisses von Wasserdampf in der oberen Troposphäre und unteren Stratosphäre (UTLS) einen großen Einfluss auf den Strahlungshaushalt der Atmosphäre und somit eine zusätzliche positive Rückkopplung auf das Klima haben.

In dieser Arbeit werden vier Fälle untersucht, in denen Wasserdampf in die Stratosphäre injiziert wurde. Zwei davon sind Fälle von konvektivem Überschießen und zwei weitere sind Fälle von Pyrokonvektion. In all diesen Fällen wurden in der Stratosphäre ungewöhnliche Wasserdampfmischungsverhältnisse gemessen und anhaltende dynamische Signaturen (potenzielle Wirbelstromanomalien) erzeugt. Für die konvektiven Fälle wurden die Messungen mit dem Cryogenic Frostpoint Hygrometer (CFH) unter Verwendung von Trifluoromethan durchgeführt, auch bekannt als das Kühlmittel Fluoroform (R-23). R-23 ist in Europa seit dem Jahr 2020 nicht mehr erwerbbar. Daher wird in dieser Arbeit eine alternative Kühlmethode für das Gerät erfolgreich untersucht und getestet.

Die beiden Fälle von konvektivem Überschießen wurden an zwei aufeinanderfolgenden Tagen im Frühsommer 2019 in den mittleren Breiten Europas untersucht. Mit ballongetragenen Instrumenten wurden Messungen des konvektiv injizierten Wasserdampfs in der Stratosphäre durchgeführt. Die Größenordnung des betroffenen stratosphärischen Wasserdampfs erreichte bis zu 12.1 ppmv mit einem Hintergrundwert von ungefähr 5 ppmv. Die vom MLS-Satelliten gemessenen, entsprechenden Wasserdampfwerte in der LS

sind niedriger als die In-situ-Beobachtungen. Die ERA5-Reanalyse überschätzte die Wasserdampfmischungsverhältnisse. Die Rückwärtstrajektorien zu den gemessenen troposphärischen Luftmassen zeigen, dass die Befeuchtung der LS mehrere Stunden vor dem Ballonstart stattfand. Dies ist in guter Übereinstimmung mit der Reanalyse, die eine starke Veränderung der Isothermenstruktur und einen plötzlichen und kurzzeitigen Anstieg der potenziellen Wirbelstärke zeigt. Ebenso zeigen weitere Satellitendaten niedrige Wolkenobergrenzen-Helligkeitstemperaturen während des überschießenden Ereignisses, was auf eine erhöhte Wolkenobergrenze hindeutet.

Die beiden pyrokonvektiven Fälle, die durch die Waldbrände in den Jahren 2017 und 2019/2020 entstanden, führten zu Wasserdampfmischungsverhältnissen von bis zu 19 und 20 ppmv in 100 hPa und die betroffenen Luftmassen erreichten schließlich Druckniveaus von 38 hPa bzw. 12 hPa, wie vom MLS gemessen wurde. Die Auswirkungen dieser Brände sind auch in der ECMWF ERA5-Reanalyse als individueller Wirbel (erhöhter relativer Luftdruck) erkennbar, der durch die Aerosolbelastung kontinuierlich aufgeheizt wurde. Dies verursachte den starken vertikalen Anstieg in der Stratosphäre und verhinderte die Vermischung der Luftmassen mit der umgebenden Luft. Außerdem führte dies zu langen Lebensdauern der Wirbel. Im Gegensatz zu den konvektiven Fällen zeigt ERA5 keine erhöhten Wasserdampfwerte in Verbindung mit den Luftmassen, die von den Waldbränden betroffen waren.

Contents

1	Introduction	1
1.1	Water vapor in the lower stratosphere	5
1.2	Convective storms in the extra-tropics	6
1.3	Pyro-convection in the extra-tropics	9
2	Theoretical background of convective storms	11
3	Balloon-borne measurements	22
3.1	Vaisala Radiosonde RS41	25
3.2	Electrochemical concentration cell (ECC)	27
3.3	Cryogenic frost-point hygrometer (CFH)	30
3.4	Towards the development of a new CFH cooling agent	33
4	Enhanced water vapor in the LS caused by convective storms	44
4.1	Data and methods	46
4.1.1	Balloon measurements within MOSES	46
4.1.2	Aura Microwave Limb Sounder (MLS)	47
4.1.3	ECMWF ERA5	48
4.1.4	Trajectory calculation	49
4.2	Measurement results and analysis	49
4.2.1	Meteorological situation at the time of the case study	49
4.2.2	Water vapor injection captured by balloon profiles	51
4.2.3	Source of the ozone peak at 150 hPa	53

4.2.4	Comparison to the ERA5 reanalysis	56
4.2.5	Origin and evolution of the water vapor enhancement along the CLaMS trajectories	59
4.2.6	Overshooting events in satellite data	64
4.3	Discussion	68
4.4	Conclusions	73
5	Highly enhanced stratospheric water vapor caused by forest fires	75
5.1	Methods	78
5.1.1	Plume identification	78
5.2	Water vapor signal in the LS	79
5.3	Horizontal plume distribution	84
5.4	Vertical plume distribution	86
5.5	PV anomalies in ECMWF ERA5	88
5.6	Summary and conclusion	92
6	Summary and outlook	95
	List of figures	98
	List of tables	101
	List of abbreviations	102
	Bibliography	105
A	Theory of balloon-launching operations and buoyancy	124
B	Supplements for Chapter 3	127
C	Supplements for Chapter 4	129
D	Supplements for Chapter 5	130

Chapter 1

Introduction

The atmosphere of the Earth is structured in multiple layers which are defined by distinct characteristics. The layer closest to the surface is called the troposphere. Its temperature is decreasing with increasing height and it is in direct interaction with the Earth's surface, defining weather and air quality. A multitude of aerosols and trace gases vary in concentration spatially and over time in the troposphere. Relatively low ozone mixing ratios of 0 - 100 ppbv and high moisture levels of 100 - 50000 ppmv (Wallace and Hobbs, 2006) are prevailing there. Condensation of water vapor and cloud formation frequently occurs in ascending air masses, due to the negative temperature gradient, and falls out as rain or snow. This process is vertically limited by the tropopause, which is the transition region between the troposphere and the overlying layer of the atmosphere, called the stratosphere. In the stratosphere the temperature gradient reverses and causes the tropopause to be one of the coldest regions in the atmosphere. The tropopause is usually found at altitudes between 16 - 19 km in the tropics and between 6 - 9 km at the poles. Exchange of air masses between these two layers is prevented by the characteristic properties of the troposphere and stratosphere. The stable stratosphere creates a boundary for the periodically unstable and dynamical active tropospheric air. Gettelman et al. (2011) describe the tropopause as "a strong static stability gradient and dynamic barrier to transport". In contrast to tropospheric air masses, stratospheric air masses are rich in ozone, dry and have high potential vorticity values, which are a measure of the

absolute circulation of an air parcel between two isentropic surfaces. A vast majority of the stratospheric air masses enter the stratosphere through the tropical tropopause layer and join into the Brewer-Dobson circulation, where it gets distributed to higher altitudes deep into the stratosphere as well as to higher latitudes (Newell, 1963). Finally, the air masses descend over the polar regions and can reenter the troposphere.

Tropospheric air mass circulations lead to the different climate zones of the Earth. They are ultimately driven by the radiation from the sun, As the air closer to the equator is exposed to a stronger radiation and rises in the tropical regions. Combined with the Coriolis force this results in three cells on each hemisphere governing the global circulation pattern in the troposphere. These cells lead to the formation of the polar and sub-polar jets and separate the cold polar air from the warmer air at low and middle latitudes. Radiative properties of the air, defined by the amount and composition of greenhouse gases like water vapor (H₂O), carbon dioxide (CO₂) or methane (CH₄), hence influence the global warming. The trace gas CO₂ makes up only a fraction of the major air constituents and had mixing ratios between 180 and 300 ppmv over the past 800000 years (Pachauri and Meyer, 2014; Lüthi et al., 2008). Methane concentrations varied between 300 and 800 ppbv in the 400000 years before the year 1880, but strongly increased to 1756 ppbv in 2003 (Hansen, 2005). Nowadays, the CO₂ mixing ratio increased by 30% to 413.7 ppmv while methane mixing ratios more than doubled. Along with the increase of other greenhouse gases, this induces crucial changes in the climate on the entire globe (Pachauri and Meyer, 2014; Laboratory, 2021). The change in the concentration of greenhouse gases results in a change of the radiative balance in the atmosphere leading to increasing air temperatures. The ongoing climate change is responsible for an increase in the mean surface temperature warming of 1.2 °C above pre-industrial times and is projected to rise up to between 1.4 and 5.8 °C in the next century (Pachauri and Meyer, 2014; Masson-Delmotte et al., 2021; Berkeley Earth, 2021). These values reflect the mean global change including regional changes and the complex interactions between the different compartments (soil, vegetation, oceans, cryosphere and atmosphere) of the planet. While the change in the mean global temperature might impact the individual

climate variables on a longer term, short-term extreme weather events have a stronger influence on the ecosystem and on the population (Ummenhofer and Meehl, 2017). When events, which were previously considered extraordinary, become the new routine and increase in frequency and strength, the real extent of the global climate change can be felt. A warmer atmosphere can uptake a higher amount of water vapor which itself is a strong greenhouse gas and further fuels the increase in air temperature. But not only that, higher amounts of water vapor in the atmosphere lead to an intensification of the hydrological cycle and hence to more latent heat in the troposphere and the development of stronger storms. The insurance company MunichRE shows that the total number of natural catastrophes increased from 249 in the year 1980 to 820 in the year 2019 with the most significant increase seen in meteorological events (hail, tornadoes, thunderstorms, winter storms, cyclones) and hydrological (floods, flash floods, storm surges) events (MunichRE, 2021). From chaos theory one can learn that increases in the extreme values can be a precursor for a change of the system if thresholds are involved in the system (Walsh et al., 2020). Our climate system is full of thresholds which are strongly interconnected. And hence we can not expect any part of the globe to stay unaffected by the massive changes in the individual environment. Whether individual extreme events can be attributed to the increase in average global temperature has long been unclear. However, in the past years more and more cases could be attributed to anthropogenic climate change. Peterson et al. (2012) report of the analysis of 6 extreme weather events in 2011 and find that not all of the discussed events are driven by man-made climate change. When identifying 29 extreme events, Herring et al. (2015) find that the probability for extreme events which are directly linked to the increase in temperature, like heat waves, is significantly increased due to anthropogenic climate change. For other extreme events, like winter storms, the picture is more complex. While some specific events can clearly be linked to the rising temperature of the troposphere, it is unclear for others. With progressing time more and more extreme weather events can be attributed to climate change. The latest publication reports about 16 different extreme weather events and their link to global warming (Herring et al., 2021).

Most observations presented in this thesis were conducted in the framework of the Modular Observation Solutions for Earth Systems (MOSES) platform. MOSES is a long-term initiative established by multiple Helmholtz Centers who are involved in the research field of "Earth and Environment". Its objective is to improve the understanding of short-term extreme events on the long-term climate (Weber and Schuetze, 2019). The deeper insight of extreme events shows that the impact of one extreme event is never limited to one Earth compartment or even one research field. Atmospheric conditions have an effect on the state of soil and water bodies in turn have an effect on biota and also vice versa. Hence, it is indispensable to define the necessary parameters which are relevant for this interaction and to collaborate with experts from different research fields. To structure the collaboration of a large amount of research groups, four different event types were identified: Heat waves and droughts, hydrologic extremes, abrupt permafrost thaw and ocean eddies. All of these topics have two major aspects in common: firstly, all of these event types include a variety of research topics and secondly, they are hard to predict and hence it is a challenge to organize multiple research groups from multiple institutes to operate on demand using mobile observation stations.

The aim of this thesis is to show the importance of convective overshooting and the related transport of moist tropospheric air masses into the Lower Stratosphere (LS). In particular three goals were formulated: Firstly, to capture and analyze a water vapor injection into the LS caused by overshooting convection. Secondly, to analyze the impact of forest fires on the water vapor distribution in the stratosphere within two case studies. And lastly, to develop an alternative to the cooling system for the stratospheric balloon-borne water vapor instrument which is currently influenced by the cut in supply of Trifluoromethane, also known as Fluoroform (R-23).

The thesis is divided into 6 chapters. The first chapter introduces the topic of water vapor injections into the LS by convective overshooting caused by thunderstorms as well as by forest fires. Chapter 2 describes the theoretical background of convective storm formation followed by the 3rd chapter, which describes the used methods and instruments. Chapters 4 and 5 show two case studies of water vapor injection into the stratosphere. Chapter

4 presents two different thunderstorm events observed during a measurement campaign performed by the working group of the hydrological event chain within the MOSES initiative and is published in Khordakova et al. (2022). Chapter 5 discusses the transport of water vapor into the LS caused by two forest fires in summer 2017 in Canada and 2020 in Australia. Chapter 6 gives a summary and conclusion of the thesis.

1.1 Water vapor in the lower stratosphere

Stratospheric water vapor is determined by the entry mixing ratio of H₂O at the tropopause and a chemical contribution by the oxidation of CH₄ to H₂O (Randel et al., 1998). A large fraction of air masses in the LS has previously passed the Tropical Tropopause Layer (TTL) or has been transported horizontally into the extra-tropics. Zahn et al. (2014) and Krebsbach et al. (2006) describe the water vapor distribution in the extra-tropical LS throughout the annual cycle. In mid-latitudes during winter the gradient in water vapor mixing ratios around the tropopause is steepest when the LS is rather dry with water vapor mixing ratios of 4 - 6 ppmv. During summer, not only highest mixing ratios are reached, but also the variation of water vapor mixing ratios maximizes. Through the analysis of multiple data sets, the water vapor background value in the LS is found to be ≈ 5 ppmv (Pan et al., 2000; Hegglin et al., 2009); any stronger enhancements of water vapor in the LS are likely caused by in-mixing of tropospheric air masses (Smith et al., 2017; Wang, 2003). Stratospheric water vapor influences the climate and the chemistry of the atmosphere and plays a significant role in the positive feedback of global climate warming (Smith et al., 2017; Dessler et al., 2008, 2013, 2014). The feedback effect of water vapor in the stratosphere is about 0.24 W m^{-2} for each 1 ppmv increase assuming an equal distribution globally (Solomon et al., 2010; Forster and Shine, 1999). Even small changes of the water vapor mixing ratio in the Upper Troposphere / Lower Stratosphere (UTLS) result in large radiative effects (Solomon et al., 2010; Riese et al., 2012). While the water vapor in the LS was found to increase by 1% (or 0.05 ppmv) per year throughout the time period between 1954 and 2000 (Oltmans et al., 2000; Rosenlof and Kley, 2001), Solomon et al. (2010) report an increase of about 1 ppmv between 1980 and

2000 and a strong decrease of about 10% between 2000 and 2010. This decreasing trend is also found by Hegglin et al. (2014) for the lower and mid-stratosphere. However, a good trend estimation in the LS is difficult and with further progress in climate change other feedback mechanism like overshooting convection can even contribute to stronger moistening of the LS. A moistening of the lowermost stratosphere also has an impact on the chemistry of this region. Water vapor is a source of OH_x radicals and enhances the reactivity of stratospheric sulphate aerosol particles. Anderson et al. (2012) have hypothesized that the moistening of the lowermost stratosphere by convective overshooting can lead to severe ozone depletion in summer in the mid-latitudes via heterogeneous chlorine activation. However, in a detailed analysis of the relevant chemical processes, Robrecht et al. (2019, 2020) conclude that convective moistening only has a minor impact on stratospheric ozone and the mid-latitude ozone column. It was shown in previous work that deep convective events can penetrate the tropopause and have a significant impact on the water vapor concentration in the lower stratosphere (Dessler et al., 2008, 2013, 2014; Smith et al., 2017).

1.2 Convective storms in the extra-tropics

Extra-tropical convective storms are a common phenomena especially during spring and early summer season. They appear in a variety of structures and severity. The investigation of severe convective storms has a long history (Doswell III, 2007) and still a lot of questions remain unanswered. Browning and Ludlam (1961) and references therein describe the variety of convective storms. While single cells can dissipate within 10 minutes, a severe thunderstorm may last up to 12 hours or more and can destroy entire landscapes. As average tropospheric temperatures rise due to climate change, it is also expected that the amount of water vapor in the troposphere will increase as warmer air can hold more water vapor compared to colder air (described by equation 2.4 in Chapter 2). Following the rate of change given by the Clausius–Clapeyron equation (CC) one can assume a water vapor increase by 7% for every degree of increase in temperature (Trenberth et al., 2003; Pall et al., 2007; Lenderink and Van Meijgaard, 2008). Boer (1993)

shows with a global circulation model, that overall the average precipitation is expected to rise by 3% - 15% in a scenario with a doubling of the CO₂ mixing ratio. However, multiple studies show that the relative rate of change for precipitation exceeds the one for temperature. Berg et al. (2013) find that this is especially the case for convective storms in contrast to stratiform precipitation.

Feng et al. (2016) use observational data to show that in the United States the rate of precipitation increase from mesoscale convective systems (MCS) is exceeding the increase of overall precipitation. While precipitation from MCS increased by 28% per decade between 1997 and 2014 (25% per decade between 1979 and 2014), the overall increase in precipitation reached 4% per decade (3% per decade between 1979 and 2014). A possible explanation for this observation is the strengthening of the low-level jet coupled with a transport of moisture. Additionally, it is shown that in large parts of Europe precipitation rates increase to almost 14% per degree change in temperature. One possible explanation is the change in atmospheric conditions leading to convective storms, for example a change in the atmospheric moist adiabatic lapse rate (Berg et al., 2013). Romps (2011) argue that due to the change in moist adiabatic lapse rate, the amount of water precipitated while moving from cloud base to a given higher level can be described as the difference of saturation water vapor mixing ratio between both levels. Del Genio et al. (2007) find that updrafts strengthen by 1 m s⁻¹ in the same modeling scenario, caused by a displacement of the freezing level towards higher altitudes. They further find that in the western United States the frequency of lightning-producing storms that induce forest-fires decrease, but when considering the most severe storms the occurrence increases by 26%. Taszarek et al. (2020) perform a climatology of convective storms in the extratropics, above the United States and Europe. While they find that extreme events are more frequent in the United States, the destructive effects might lead to fiercer damage in Europe due to higher population density. They find that over continental Europe the most frequent convective events can be found in spring and over Mediterranean Europe in fall. The peak activity is found to take place over mountains and over Italy. The total duration of convective storms is ranging between 5 h and 100 h. These studies indicate

1.2. Convective storms in the extra-tropics

the need for reinforced attention to the ongoing change in the occurrence of convective storms. However, the impact of convective storms reaches beyond the local impact on landscapes and immediate hazard to the population. The influence of convective storms on long-term climate has to be considered. Severe convective events can also influence the local UTLS by moistening the otherwise dry stratosphere. If convection penetrates the tropopause and transports air masses into the LS, it is referred to as overshooting convection.

Cooney et al. (2018) analyze a 10 year data set of overshooting convection for the eastern two thirds of the United States. They find that most overshooting events take place in May - July and are most common in the central United States. Further, 45% of the overshooting events exceeded the 380 K potential temperature level and thus can strongly impact the composition of the LS. Phoenix and Homeyer (2021) simulate two kinds of convection - one representing spring time convective events and one representing convective events typical for summer time. The study shows that the spring time convective events lead to an increase of about 20% in the average water vapor mixing ratio in the UTLS while the summer time convection leads to a lower increase.

The contribution of overshooting convection to the moisture budget of the lower stratosphere and a potential increase of overshooting convection with global warming is still under discussion. It was shown that the primary region for direct convective hydration of the extra-tropics is located over North America (Jensen et al., 2020). These direct injections over the North American continent (NA) have been evaluated in several case studies including an analysis of long-term behavior of injected air masses (Weinstock et al., 2007; Homeyer and Kumjian, 2015; Homeyer et al., 2017; Smith et al., 2017). Currently, only limited amount of studies have been performed on the topic of overshooting cloud tops produced by extreme convective events over Europe, although the necessity to improve the understanding of the long-term impact of the water vapor transport into the LS is crucial. Fischer et al. (2003) show data displaying troposphere to stratosphere transport of tropospheric trace gases caused by convective storms over Italy. Furthermore, Hegglin et al. (2004) analyze a case study of tropospheric air injection into the LS

by a large convective system over the Mediterranean area.

1.3 Pyro-convection in the extra-tropics

Wild forest fires are common events in late summer at high latitudes and are part of the natural cycle which controls multiple ecosystem processes. With increasing global temperatures, the frequency and intensity of forest fires is expected to increase especially on the North American and the northern part of the Asian continent. The area affected by forest fires in Canada has increased in the past decades and it was shown to be influenced by anthropogenic climate change (Stocks et al., 1998; Gillett et al., 2004; Kasischke and Turetsky, 2006; Balshi et al., 2009; De Groot et al., 2013; Clements et al., 2018).

Similar to normal deep convection, pyro-convection also depends on favorable atmospheric conditions. But the favorable conditions are greatly amplified by forest fires, due to the heat released by the fire itself (Damoah et al., 2006). Additionally, the microphysical and radiative conditions are different due to the large amount of aerosols produced by the fire. The aerosols suppress precipitation formation by reducing the cloud droplet size and hence shifting the onset of precipitation to higher altitudes. This leads to a higher amount of ice formation in higher altitudes as compared to regular convection. Therefore, the amount of latent heat in higher altitudes increases (Andreae et al., 2004; Rosenfeld et al., 2007). Rodriguez et al. (2020) report updrafts of up to 60 m s^{-1} and downdrafts of 30 m s^{-1} in pyro-convective storms which compares to tornadic supercell storms. Additionally, the fire plume of air is subject to further heating due to the absorption of radiation by the black carbon particles leading to a further lifting and possible entering the UTLS region. Multiple observations have shown that a transport of tropospheric air originating from wild forest fires reached above the tropopause with potential temperatures of 380 K penetrating the LS (Jost et al., 2004). Once the pyro-plume has crossed the tropopause it can be horizontally transported throughout the hemisphere where it can have significant radiative influence on climate (Fromm et al., 2010). However, not all forest fires reach these altitudes and favorable meteorological conditions have to be met like the preceding of a cold front.

Recently, it was shown that pyro-convection can not only transport large amount of aerosols into the UTLS (Soo Lee et al., 2020) but also water vapor (Pumphrey et al., 2011a; Kablick et al., 2018). The water vapor is produced by the fire itself, due to the release of water stored in the soil and vegetation. The fire also transports the water vapor aloft by the updrafts. Pumphrey et al. (2011a) report water vapor enhancements at pressure levels of 100 and 147 hPa as a consequence of the Australian bush fires in February 2009 (increasing from ≈ 2 ppmv to ≈ 5 ppmv at 100 hPa). Pumphrey et al. (2020) describe elevated water vapor mixing ratios caused by a forest fire reaching a pressure level of 21 hPa and Lestrelin et al. (2021) show a formation of a local vortex in the stratosphere caused by the wild fire in Australia. While the immediate injection of carbon monoxide (CO) into the stratosphere is significantly more dramatic in terms of relative values, the impact of water vapor can be seen on a longer time scale due to the short lifetime of CO in the stratosphere (Minschwaner et al., 2010). The plume in the stratosphere produced by the forest fire can be traced for an extended period of time when considering elevated water vapor values due to the longer lifetime of water vapor in the stratosphere which has only sink regions in the mesosphere and at the stratospheric winter pole. The methods used in these studies are also applied in Chapter 5.

Chapter 2

Theoretical background of convective storms

"Convection" by itself describes the transport of one quantity by a fluid - a gas or a liquid. In most cases this quantity is heat. In meteorology this is mostly applied to the vertical transport of heat in contrast to the global circulation when heat is transported horizontally from the equator to the poles. Therefore, in atmospheric sciences convection refers to the spatially limited local upward movement of air including transport of heat. On shorter timescales one can assume that air parcels travel adiabatically through the atmosphere if the air parcel is not exposed to external energy sources. This results in the assumption that air travels along lines of equal potential temperature, the isentropes. Potential temperature is defined as the temperature an air parcel would have if it was transported adiabatically to the surface and can be calculated as:

$$\theta = T \cdot \left(\frac{P_0}{P} \right)^{\frac{R}{c_p}} \quad (2.1)$$

where θ is the potential temperature, P_0 is the ambient pressure at surface level, P is the pressure at any given level, R is the universal gas constant and c_p is the specific heat at constant pressure for dry air. Throughout the troposphere θ only shows a slight increase with altitude and can be considered almost constant relative to the steep increase that oc-

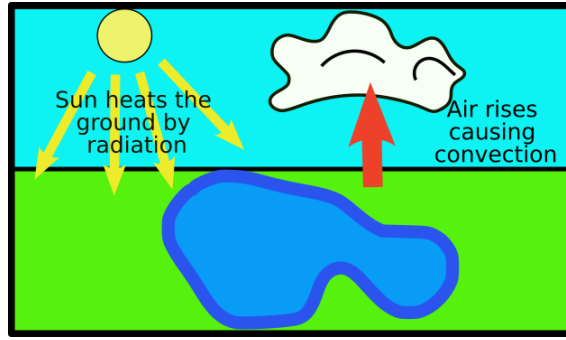


Figure 2.1: Schematic illustration of radiative influence on air movement. Radiation from the sun heats the air. Air above a water body contains more moisture compared to dryer air above land. Both air parcels are lifted upon being heated, but at different rates which results in different lifting rates.

curs above the tropopause, resulting in periodically unstable conditions where air parcels can ascend and descent. In the stratosphere on the other hand, θ has a steep increase resulting in very stable conditions where air parcels are inhibited from rising (Wallace and Hobbs, 2006). This upward movement within convection is caused by a change of buoyancy driven by the difference in density of an air parcel compared to its surroundings. Buoyancy B is described as (Doswell III, 2001):

$$B = g \cdot \frac{T - T'}{T'}. \quad (2.2)$$

Here, g is the gravitational acceleration, T the temperature of the air parcel and T' is the temperature of the surrounding environment.

Convection is usually driven by the radiation from the sun, as an external source of energy. Air in proximity to the ground is heated by sunlight and decreases its density (schematically shown in Fig. 2.1). It is then lifted following the hydrostatic equation, which is given as:

$$\frac{\delta p}{\delta z} = -g \cdot \rho \quad (2.3)$$

where z is the altitude, p is the pressure which decreases with altitude, g is the gravitational acceleration and ρ is the density of air. It is evident that as ρ decreases δz increases and the air parcel is lifted (Wallace and Hobbs, 2006).

Convection can be distinguished in either dry or moist convection. In the first case, the

heated air is lifted without a relevant amount of moisture and would follow an isentrope during ascent if no further radiation impacted the temperature or density. This type of convection is not related to the appearance of storms and is rather relevant to aviation. In the second case, water vapor in the air parcel is involved. First of all, humid air is less dense than dry air leading to a stronger gradient in density and strength of the convection. Further, as the air ascends and cools, water vapor condensates and latent heat is released, caused by the phase transition from vapor to liquid cloud droplets. Water vapor condensates when the relative humidity above 100% is reached and Cloud Condensation Nuclei (CCN) are available. These are aerosol particles with a size of about $0.2 \mu\text{m}$ and are abundant in the troposphere. The relative humidity depends on the temperature of the air parcel which cools as it ascends. The dependence of relative humidity on temperature is given by the Clausius-Clapeyron equation (CC) which is described as:

$$\frac{\delta p}{\delta T} = \frac{\Delta H_{vap}}{T \cdot (v_1 - v_2)} \quad (2.4)$$

where p is the partial pressure of water vapor, T is the temperature of the air parcel, ΔH_{vap} is the enthalpy of vaporization (latent heat) and v_1 and v_2 are the molar volumes of both phases.

Neglecting the molar volume of the liquid phase and assuming that in the relevant temperature range the latent heat ΔH_{vap} remains constant, one can use the following formula, 2.5, to describe the change in partial pressure in dependence on the change in temperature as compared to a reference state T^* and p^* :

$$p = p^* \cdot \exp\left(-\frac{\Delta H_{vap}}{R} \cdot \left(\frac{1}{T} - \frac{1}{T^*}\right)\right). \quad (2.5)$$

The saturation water vapor $e_s(T)$ can be approximated by the integration of equation 2.5 which results in the August–Roche–Magnus formula as:

$$e_s(T) = 6.1094 \exp\left(\frac{17.625T}{T + 243.04}\right) \quad (2.6)$$

which is valid for ambient temperatures from -50 °C to 100 °C (Wiegleb, 2016).

When the water vapor condensates, latent heat is released and the air parcel is further lifted. This leads to the difference between dry convection and moist convection which is associated with thunderstorms, severe convection or deep convection. As the air rises with strong updraft, a low pressure area develops at ground level leading to strong surface wind gusts. Furthermore, downdrafts transport cold air from higher altitudes to the surface reinforced by precipitation and the displacement of air at higher altitudes. The change in buoyancy depends on the air parcel moisture and the lapse rate difference between ambient air and the lifted air parcel. The lapse rate is the vertical temperature gradient and depends on the relative humidity. The buoyancy can be rewritten as

$$B = -\frac{g}{T'} \cdot \left(-\frac{\delta T}{\delta z} + \frac{\delta T'}{\delta z'} \right) \quad (2.7)$$

which equals to

$$B = -\frac{g}{T'} \cdot (\Gamma - \gamma) \quad (2.8)$$

where γ is the lapse rate of the ambient air, Γ is the lapse rate of the air parcel, T' is the ambient temperature and T is the temperature of the air parcel. If the lapse rate of the ambient air (γ) is higher than the lapse rate of the air parcel (Γ), the ambient air cools faster than the air parcel and, thus, it is continuously transported upwards as buoyancy B remains positive. The altitude at which an air parcel starts to be lifted adiabatically is referred to as the Level of Free Convection (LFC). The level at which the buoyancy of an air parcel becomes neutral and the air parcel is rising at the same rate as the ambient air is called the Equilibrium Level (EL). At any given point on the surface, buoyancy can be integrated vertically as it is shown exemplarily in Fig. 2.2. When the integration from the LFC to the EL is performed, the result is known as Convective Available Potential Energy (CAPE) which is given in units of J kg^{-1} . This value is frequently used to predict how severe a convection may get if it is initiated. Figure 2.2 shows exemplarily one arbitrary Skew-T diagram. The dashed red line corresponds to the dry adiabatic cooling which is the isentrope where potential temperature is constant and the dashed dark blue

line shows the moist adiabatic lapse rate. The solid dark green line represents the actual humidity profile and the solid red line shows the actual temperature profile at the given location. The air parcel follows the dry adiabatic lapse rate until the LFC and then further follows the moist adiabatic lapse rate. The LFC may be found in a Skew-T diagram at the intersection of the the dry adiabatic lapse rate of the air parcel at ground level and the isohume (constant saturation mixing ratio, shown in Fig. 2.2 with green dashed lines). The integral between the LFC and the EL, enclosed by the real temperature profile and the moist adiabat starting at the LFC, yield the actual CAPE value (integrated buoyancy of the air parcel, red area in Fig. 2.2). High CAPE values are expected with high moisture at ground level and steep lapse rates conditions. Approximately at CAPE values greater than 1000 J kg^{-1} a development of strong convection can take place. In this case a considerable maximal vertical velocity W_{max} of around 44 m s^{-1} can be reached by using the approximation in dependence on CAPE:

$$W_{max} = \sqrt{2 \cdot CAPE}. \quad (2.9)$$

However, high CAPE values alone cannot trigger convection by themselves but are an indicator for strong updrafts in case of an initiation of convection. Multiple factors can prevent the development of a convective storm. One of these factors is possible intrusion of dry air into the convective cell, which is illustrated in Fig. 2.3. As convection develops, dry air is mixed into the moist buoyant air which suppresses further convection development, due to the reduction in relative humidity and thus less latent heat release. An additional factor is Convective Inhibition (CIN) which is also illustrated in Fig. 2.2 as the blue area below the red area in terms of altitude. The CIN prevents the initiation of a convective storm as an air parcel needs to be lifted above that level to initiate the development of convection. Possible causes for such a lift are fronts or convergence zones, orography or boundary layer circulation. Therefore, lower CIN values and higher moisture in the lower-level layers provide favorable conditions for the initiation of strong convection in combination with strong CAPE values. Further, the wind speed and wind shear play

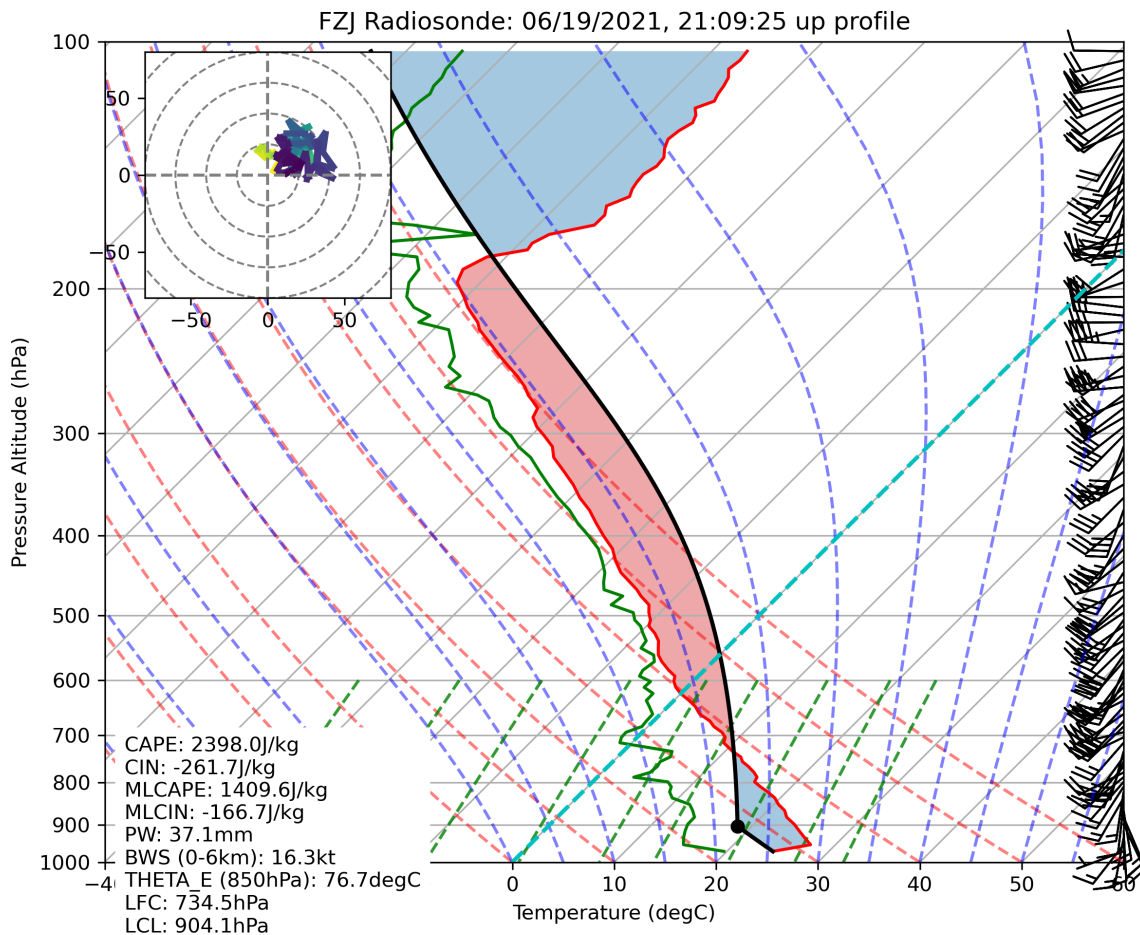


Figure 2.2: Arbitrary Skew-T diagram with a high CAPE value, represented with the red area and stable areas represented by the blue areas. The solid lines depict the measured relative humidity (green line), and temperature (red line). The solid black line indicated the theoretical ascend profile of a air parcel measured at the ground. The dashed lines show the dry adiabatic cooling lines (dashed red lines), moist adiabatic lapse rate (dashed blue line), and constant saturation mixing ratio (dashed green line). The barbs show the wind speed and direction at each pressure level. In the upper left corner a wind hodograph is given, indicating the wind speed and direction with increasing altitude.



Figure 2.3: Picture of a convection cell with a dissolving cloud top due to dry air entrainment. Picture taken by Bernhard Muhr.

an important role in the development of a convective storm. On the one hand vertical wind shear can inhibit the lift of an air parcel over the LFC. On the other hand the vertical wind shear above the LFC leads to organized convective storm cells. A severe convective storm is build up from individual cells, where one cell typically consists of one updraft and one downdraft. After the updraft is initiated, the air mass reaches condensation level and a downdraft with strong precipitation is produced leading to a local equilibrium state of the atmosphere. The cold air in the downdraft sinks due to the difference in density. Combined with ongoing evaporation and sublimation of hydrometeors throughout the descent the air mass is further cooled accelerating the downdraft velocity. Upon reaching the surface, the cold air scatters at the ground creating a cold pool. In a single cell the downdraft inhibits the development of further updrafts and ,hence, the convective storm is terminated. However, in the presence of a vertical wind shear the precipitation is transported outside of the updraft area and does not mitigate further updraft. This way the convective cell can survive much longer then a single cell. The downdraft of a convective cell at the presence of vertical wind shear further produces an outflow area which in

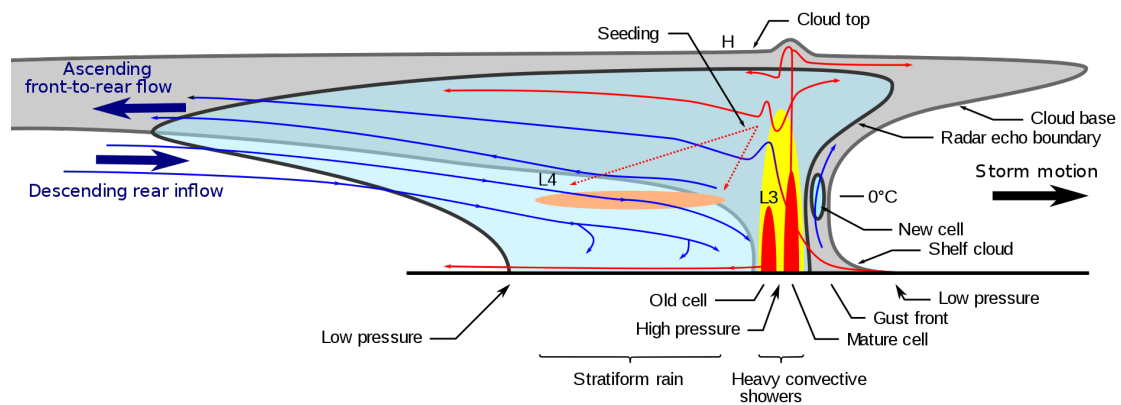


Figure 2.4: Schematic of a squall line. Image adapted from Whidou (2015), CC BY-SA 4.0

turn can initiate new convective cells through the creation of meso-heights. This leads to multi-cell clusters where multiple cells exist simultaneously at different stages of development. Multi-cell storms can be distinguished by their different structures. The first option is the squall line structure where the multi-cells are organized linearly, typically along or ahead of cold fronts. A squall line can persist over multiple hours. Eventually, the cold pool outruns the area of new cell formation and the squall line is slowly dissipating. Figure 2.4 displays the structure within a squall line. When the cold pool is preceding the squall line, it lifts the warmer air which can lead to a shelf cloud.

Another type of convective storm development is a bow echo. Fujita (1978) first uses this term to describe a Mesoscale Convective System (MCS) that appears like an archers bow on radar images. Bow echos typically have a lifetime of 3 - 6 hours and are smaller in their horizontal extend as squall lines. The descending rear inflow (referred to as rear inflow jet) plays a crucial part in the formation of the bow echo. A strong rear inflow jet strengthens the cold pool at surface level, resulting in a local high pressure area at the surface and a local low in the middle levels, which further enhances the rear inflow jet. The rear inflow jet reaches the convective edge and bows the storm system. As the jet hits the front, on both ends of the squall line vortices develop. However, throughout the lifetime of a bow echo the Coriolis force enhances the cyclonic rotation and decelerates the anticyclonic rotation (Fujita, 1978).

Another type of multi-cell structure is the super-cell. The term "super-cell" was estab-

lished by Browning (1962) where it is defined as "[a] large cell which cannot be subdivided into smaller units even when viewed at reduced gain: it develops from an amalgamation of smaller cells. It is associated with a single extensive updraft." and has a the spacial spread of "[a]bout 10 miles in diameter". Super-cells develop in the presence of extra strong updrafts and intense vertical wind shear. In the presence of a strong wind shear in speed and direction, a vertical tilt in the vorticity takes place which acquires the rotation of up- and downdraft around each other. Due to the rotating convection, a persistent low pressure system can enhance the updraft and maintain the updraft's strength. A mesocyclone develops which is shown by a schematic in Fig. 2.5. The updraft is drawn into the mesocyclone which transports the air upwards to the highest level of the convection. There it gets distributed between the front and back side of the storm. A rear-flank and a forward-flank downdraft develop (Fig. 2.5). The forward-flank downdraft forms from high water loading which evaporates during descend, creating a cold pool and pushing the warm air in front of it up and hence producing precipitation. Rear-flank downdraft is caused by the inflow of dry mid-level air which is blocked by the mesocyclone and is forced to descend. The gust front caused by the rear-flank downdraft is moving towards the gust front created by the forward-flank downdraft, which leads to a reduction of the updraft area and can result in the formation of a tornado as the cyclonic flow speeds up with decreasing inflow area. If the updraft of the convection is strong enough, the convection is producing an Overshooting Top (OT); an area of the higher-most clouds which penetrates the tropopause reaching into the lower stratosphere.

The tropopause can be defined with different approaches:

- Cold Point Tropopause (CPT): The cold point tropopause is defined as the coldest temperature level in the vertical profile between the troposphere and the stratosphere.
- Lapse Rate Tropopause (LRT): The World Meteorological Organization (WMO) defines the lapse rate tropopause as the lowest level at which the lapse rate decreases to 2 K km^{-1} and the average lapse rate from this level to any level within the next higher 2 km does not exceed 2 K km^{-1} .

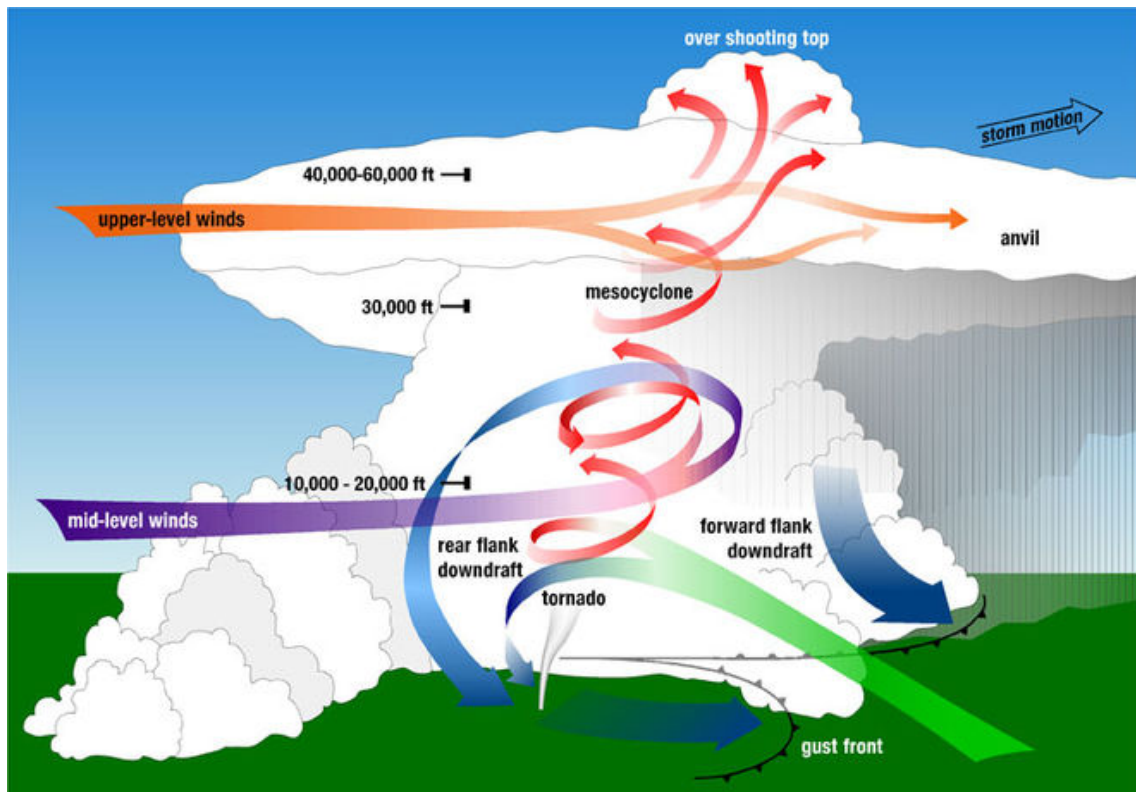


Figure 2.5: Schematic of the structure of a super-cell. Source: Mersereau (2014).

- Chemical Tropopause (CT): The chemical tropopause, also called ozone tropopause, is defined by the rapid increase of the ozone mixing ratio from the tropospheric to the stratospheric regime (Zahn et al., 2004; WMO, 1985).
- Dynamical Tropopause (DT): A threshold value of Potential Vorticity (PV) is defined in order to separate the two regimes. Usually values between 2 and 4 Potential Vorticity Units (PVU) are defining the tropopause while higher values are found in the stratosphere (Hoinka, 1997; Kunz et al., 2011b; Reed, 1954).

The tropopause, which acts as a barrier between the two distinct atmospheric regimes, can be disrupted when the air in this part of the convective storm is transported extremely fast from the lower part of the troposphere to the LS above the level of neutral buoyancy (Cooney et al., 2018; Homeyer and Kumjian, 2015). Whenever a convective storm is strong enough to produce an overshooting top it is referred to as overshooting convection. The air masses in this OT are typically colder compared to their surroundings and contain significantly more ice water. The overshooting top causes a disruption in the isotherms of

the atmospheric structure (Homeyer et al., 2017; Qu et al., 2020). This frequently leads to gravity wave breaking behind the overshooting top allowing the intrusion and mixing of tropospheric air into the stratosphere. There, ice particles evaporate in the warmer air masses and moisten the LS. Air masses within the overshooting top contain a high amount of ice water and tropospheric trace gases which can then be mixed into the LS (Fischer et al., 2003). If this process is visible as a single cloud vertically exceeding the anvil of the storm, it is referred to as a jumping cirrus (Fujita, 1982; Wang, 2003).

Chapter 3

Balloon-borne measurements

The use of air-balloons is dating back to the brothers Montgolfier, who performed the first balloon flight in 1782 still believing that smoke was the driving agent for their ascent. Only shortly after that, Jacques Charles disproved their hypothesis by performing a balloon ascent using hydrogen. Since then balloons were used for a variety of applications. Gustave Hermite introduced the use of unmanned weather balloons which carried a self-recording thermometer and barometer in 1892. Already in the very beginning of the use of weather balloons, the recovery of the payloads after landing relied on the help of the public and was rewarded. Although a flight already in 1893 reached 14.7 km and recorded an increase in temperature above 12.5 km, it took several more years until the stratosphere was discovered. The discovery of the stratosphere was first presented in 1902 at the International Aeronautical Congress in Berlin (Hoinka, 1997; von Ehrenfried, 2021; Labitzke, 1999). Since then and until today the use of weather balloons in atmospheric science is inevitable.

Today, weather services around the globe perform regular weather balloon soundings in order to acquire data for weather prediction. The German weather service alone performs 30 balloon launches every day (Reinartz, 2020). Hereby, the size of the balloon and instrumental equipment (referred to as "payload") can vary as well as the gas used to lift the balloon. Usually, Helium is used to fill the balloon. For information on the procedure to fill the balloon with the right amount of gas to achieve the desired ascend rates see

Appendix A.

In the framework of this work, two kinds of weather balloons were used. The first version is a 200 g latex balloon equipped with a Vaisala radiosonde RS41-SGP, which measures the location of the balloon as well as the altitude, pressure, temperature and humidity of the atmosphere and transmits the data to the ground station at the measurement site. The second version is a 1500 g balloon additionally equipped with a payload carrying multiple in-situ instruments. An Electrochemical Concentration Cell (ECC) instrument (Smit et al., 2007) measuring ozone concentration is used together with a Cryogenic Frostpoint Hygrometer (CFH, Vömel et al. (2007)) which measures the low water vapor concentrations prevailing in the tropopause region and in the stratosphere. The payload also contains a Compact Optical Backscatter Aerosol Detector (COBALD) to measure the back-scattered light from different types of particles during nighttime (Brabec et al., 2012). The COBALD instrument is not further described in this work as no data of the instrument are shown. The combination of the RS41, ECC, CFH and COBALD is referred to as 'large payload' in the following. The large payload is adapted from the setup used by the Global Climate Observing System Reference Upper-Air Network (GRUAN) setup (Dirksen et al., 2014). Each instrument, which is part of the payload, is individually packaged in a styrofoam container in order to thermally isolate the instrument from the cold conditions in the upper troposphere and stratosphere during the flights. The individual containers are connected with durable tape. Figure 3.1 shows a picture of a typical large payload. During the flight, the payload is separated from the balloon by more than 60 m by using an unwinder. This reduces the influence of the balloon itself on the sampled air mass in particular by outgassing of water vapor. Directly to the balloon a rope of 2 - 4 m length is attached, which connects on one side the parachute and on the other the unwinder. The unwinder is a metal spool with 60 m of rope. It is constructed in a way that the rope unwinds slowly and controlled after the launch of the balloon, which simplifies the balloon launch. The unwinder is connected to the payload.

Several considerations must be taken into account when preparing a balloon launch. Firstly, the air traffic regulation in Germany, where the balloon launches within this work

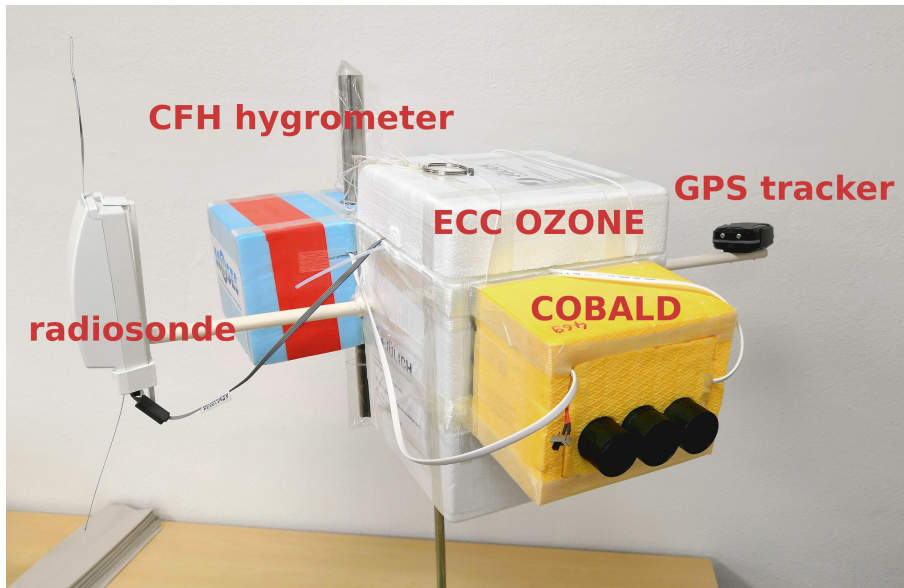


Figure 3.1: "Large payload" used for balloon measurements. The individual instruments are packed in styrofoam boxes and held together by tape. Through the white styrofoam box of the ECC a white painted wooden stick is installed on each end carrying the radiosonde and GPS, respectively. The instruments are connected electrically in line to the radiosonde which transmits all data to the ground station.

took place, limits the maximum total weight of the payload to 4 kg. The weight of the payload shown in Fig. 3.1 is ≈ 1.928 kg. In addition, the parachute used has a weight of 200 g and the unwinder has a weight of 160 g. Further, additional weight is caused by the cooling liquid of the CFH (further addressed in Section 3.3), but this has not to be accounted for as it evaporates throughout the flight.

Furthermore, precautions have to be made for the recovery of the payload after the flight. The radiosonde transmits the data measured by the in-situ instruments to the ground using a radio-signal. These data also include the GPS altitude and location of the balloon during the flight. However, when the payload approaches the ground after the balloon bursts, the radiosonde typically loses the radio connection at about 3 km above ground level due to obstacles within the long distance of the ground antenna and the radiosonde. This leaves a very wide area at which the payload could have landed. Hence, an additional independent Global Positioning System (GPS) tracker is attached to the payload which uses iridium satellites for communication and provides an accurate position of the payload after landing.



Figure 3.2: Weather balloon and payload as used during the measurements described in Chapter 4. The weather balloon with a parachute, unwinder and the large payload. The picture was taken shortly after the launch. The unwinder is slowly increasing the distance between the parachute and the payload, eventually reaching up to 60 m length.

The balloon trajectory during ascent and descent cannot be controlled but it can be predicted using wind models. A trajectory and landing position forecast is performed before each launch in order to prevent payload landing in the area of dense population or air traffic control areas. An information and contact note is attached to the payload for anyone who might find the landed payload, quite similar to the notes added during the first launches at the end of the 19th century. A balloon with a large payload shortly after the launch is depicted in Fig. 3.2. In the following sections the individual measurement instruments used in the frame of this work are described.

3.1 Vaisala Radiosonde RS41

The Vaisala Radiosonde RS41-SGP was introduced in 2014 and completely replaced the RS91 precursor model in 2017. The temperature sensor is based on resistive platinum technology. The manufacturer states that there is a combined uncertainty of 0.3 K below and of 0.4 K above 16 km height. The response time of the temperature sensor

3.1. Vaisala Radiosonde RS41

is < 1 s and, thus, does not need to be considered in the following. The temperature range is given as -95°C to 60°C with a resolution of 0.01°C (Jauhiainen et al., 2014; Vaisala, 2020). The humidity sensor is a thin-film capacitor. The combined uncertainty of the humidity sensor is given as 3% of the prevailing Relative Humidity (RH) with a resolution of 0.1%. Analogous to the temperature sensor, the response time of the humidity sensor is < 0.3 s at 20°C and < 10 s at -40°C . The pressure sensor is a silicon capacitor and is defined for a pressure range between surface pressure and 3 hPa while the resolution is given as 0.01 hPa. Dirksen et al. (2020) found in experimental work that the humidity sensor of the RS41 has an uncertainty of $< 1.5\%$ and a temperature uncertainty of $< 0.2\%$. Survo et al. (2014) also validated the uncertainty of the RS41 temperature and humidity data. No systematic drifts due to storage reasons were found either in temperature or in humidity measurements. However, an increase of the temperature uncertainty from 0.13°C in the troposphere up to 0.3°C at 30 km was found. A relative humidity uncertainty below 1% relative humidity was found in the stratosphere. Kawai et al. (2017) perform a comparison study of RS41 radiosonde data and its precursor radiosonde model RS92 and find that the difference for pressure and temperature was smaller than the nominal uncertainty, but asserted a dry bias of the RS92 humidity measurements above 17 km in the tropics, likely caused by an insufficient solar irradiation correction of the RS92 which was improved for the RS41. Figure 3.3 displays all water vapor profiles between 2018 and 2021 (26 profiles) which were measured and are available for this work, with the RS41 and the CFH as a reference instrument (see Section 3.3). When considering data up to 18 km altitude the correlation coefficient of the RS41 and CFH data is 0.975. However, the deviation between both instruments increases above ≈ 18 km and the correlation coefficient of data is reduced to 0.52 for data points measured between 18 km and 35 km. In the mid-stratosphere the low humidity in combination with low pressure and low temperature does not allow the RS41 to conduct reliable measurements. Survo et al. (2014) show a temperature dependency of the humidity sensor uncertainty, which does not exceed 3% RH at temperatures below -80°C and RH below 30%. Therefore, these astonishingly good results offer reliability in acquiring accurate

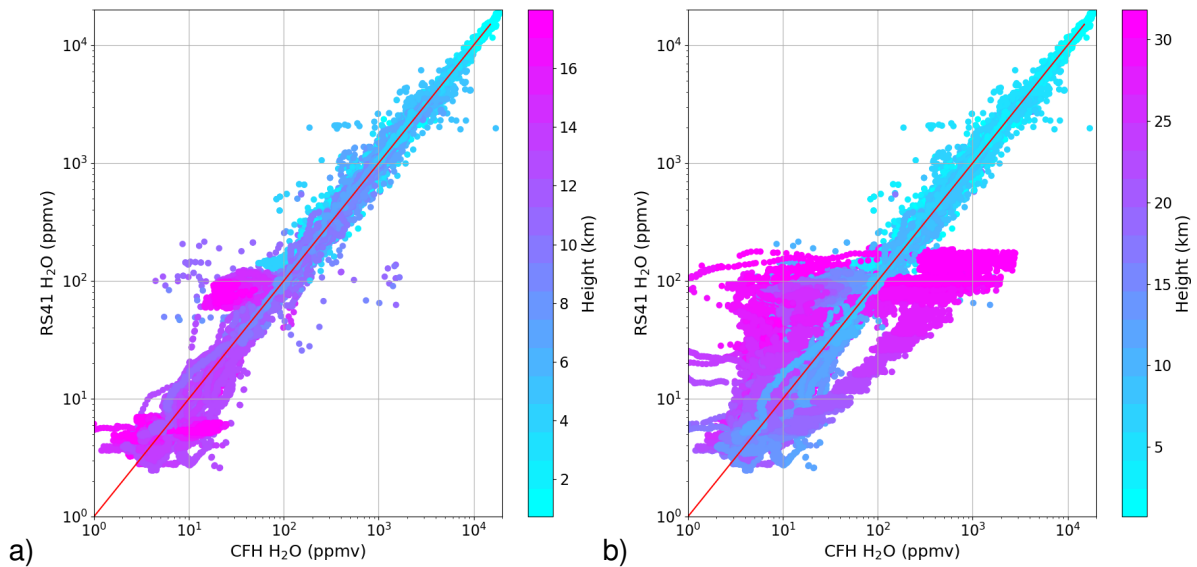
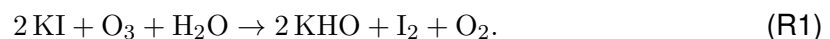


Figure 3.3: a) Correlation of water vapor mixing ratios measured simultaneously by the RS41 and the CFH. The color code represents the altitude of the measurement. All data available for this work between 2018 and 2021 are used (26 flights). Altitudes up to 18 km are used in panel a, while all altitudes are used in panel b.

RS41 humidity measurements up to a height of 18 km which are used in this study in the case of flights without the CFH instrument.

3.2 Electrochemical concentration cell (ECC)

Electrochemical concentration cells (ECCs) are light weight in-situ ozone sondes that have been used for multiple decades on weather balloons in order to investigate ozone mixing ratio profiles and to monitor long-term ozone trends, for example in the southern hemisphere within the Southern Hemisphere ADditional OZonesondes (SHADOZ) network, (Thompson et al., 2019). The ambient air is pumped through a Teflon tube into the reaction cell, which is filled with a potassium iodide (KI) solution, at a speed of about 29 s/100 ml at ground conditions. In the reaction cell of the device, a chemical reaction of the ambient ozone with KI produces iodine and two electrons for each ozone molecule as follows:



3.2. Electrochemical concentration cell (ECC)

Thus, the resulting current is proportional to the partial pressure of ozone in the sampled air and, hence, the partial pressure of the ambient ozone can be calculated from the current produced by the cell as:

$$P_{O_3} = 4.307 \times 10^{-4}(I - I_{BG}) \cdot T_p \cdot t_{100} \cdot PCF \quad (3.1)$$

where P_{O_3} is the partial pressure of ozone in the sampled air, I is the current output by the ECC, I_{BG} is the background current of the ECC, T_p is the temperature of the ECC pump, t_{100} is the flow rate time of the sampled air in seconds per 100 cm^{-3} and the Pump flow Correction Factor (PCF), which is the inverse of the pump efficiency. Therefore, the ECC does not need a calibration procedure prior to the balloon launch. However, a conditioning procedure a few days before the launch is required in order to gain high quality data. Komhyr et al. (1995) describe the ECC in detail. The pump efficiency was provided originally by Komhyr (1986). The data was later updated in Komhyr et al. (1995) which was used until recently and referred to as the "standard" PCF. Deshler et al. (2008) evaluate the influence of different solution concentrations on the measurement precision compared to a Dobson-spectrometer. They find the precision of all ozone sondes < 2 - 3%, but while the 1.0% solution overestimated the photometer and the ozone column, the 0.5% solution agreed well with the photometer but underestimated the total ozone column. Johnson et al. (2002) reevaluate this standard procedure for the ECC. New measurements reveal PCF values between 2 and 15% higher at pressure levels of 100 and 5 hPa, respectively. In the same work, a new composition of the solution is recommended as the additional buffers in the iodine solution were found to cause side reactions which lead to an increase of the ozone sonde current output. The PCF given by Komhyr et al. (1995) partly compensates this effect with smaller pump efficiency values. Johnson et al. (2002) recommend using the provided new PCF values in combination with a solution which consists of a 1% iodide solution and $1/10^{\text{th}}$ buffer solution leading to the following composition: 1 L pure water with $\Omega = 18.2 M\Omega \cdot \text{cm}$, 10 g KI, 25 g potassium bromide (KBr), 0.125 g sodium hydrogen phosphate hydrate ($\text{Na}_2\text{HPO}_4 \cdot \text{H}_2\text{O}$), and 0.5 g Disodium phos-

phate hydrate ($\text{Na}_2\text{HPO}_4 \cdot 12\text{H}_2\text{O}$). Vömel et al. (2020) evaluate the impact of a second reaction in the ECC involving the buffers. This second reaction is taking place on slow time scales compared to the main ozone-iodine reaction (R1). The contribution of the second reaction was considered constant and was referred to as I_{BG} previously. Hence, the current output is rather a sum of two reactions and can be described as:

$$I(t) = I_0 e^{-\frac{t}{\tau}} + I'_0 e^{-\frac{t}{\tau'}} \quad (3.2)$$

where $I(t)$ is the current output in dependence of time, I_0 is the current produced by the fast reaction R1 and I'_0 the current produced by the second slow reaction. τ and τ' are the respective reaction times, determined in laboratory experiments to be ≈ 20 s for τ and ≈ 25 min for τ' . Vömel et al. (2020) provide an algorithm to eliminate the contribution of the secondary reaction from the total current output of the ECC. While no change in the total ozone column is reported, in the UTLS area ozone concentrations increase by up to 7% and above 30 km decrease by 7%.

To emphasize the difference between both methods, Fig. 3.4 displays the results exemplary for one flight performed on the 11 June 2019 at midnight. The absolute difference between both methods can be neglected in the troposphere but increases with altitude as shown in the lower left panel for the entire profile. It is especially visible in the UTLS (upper left panel) that the strongest deviations take place at tipping points of the ozone profile. Here, the relative change can even exceed 40%. Firstly, the strongest spikes in relative change are at the transition from the tropospheric to the stratospheric regime and slightly above a tipping point of a stronger ozone filament around 14 km. In both cases, the newer method by Vömel et al. (2020) shows a faster reaction to an abrupt change in ozone mixing ratios. As the focus of this study is on the fast, small scale variations of ozone, we use a solution composition of $1/10^{\text{th}}$ and a full buffer suggested by Johnson et al. (2002) together with the data analysis proposed by Vömel et al. (2020). This is in contrast to the long-term measurement series that consistently uses one solution combination suggested by Komhyr et al. (1995) and Smit et al. (2007).

3.3. Cryogenic frost-point hygrometer (CFH)

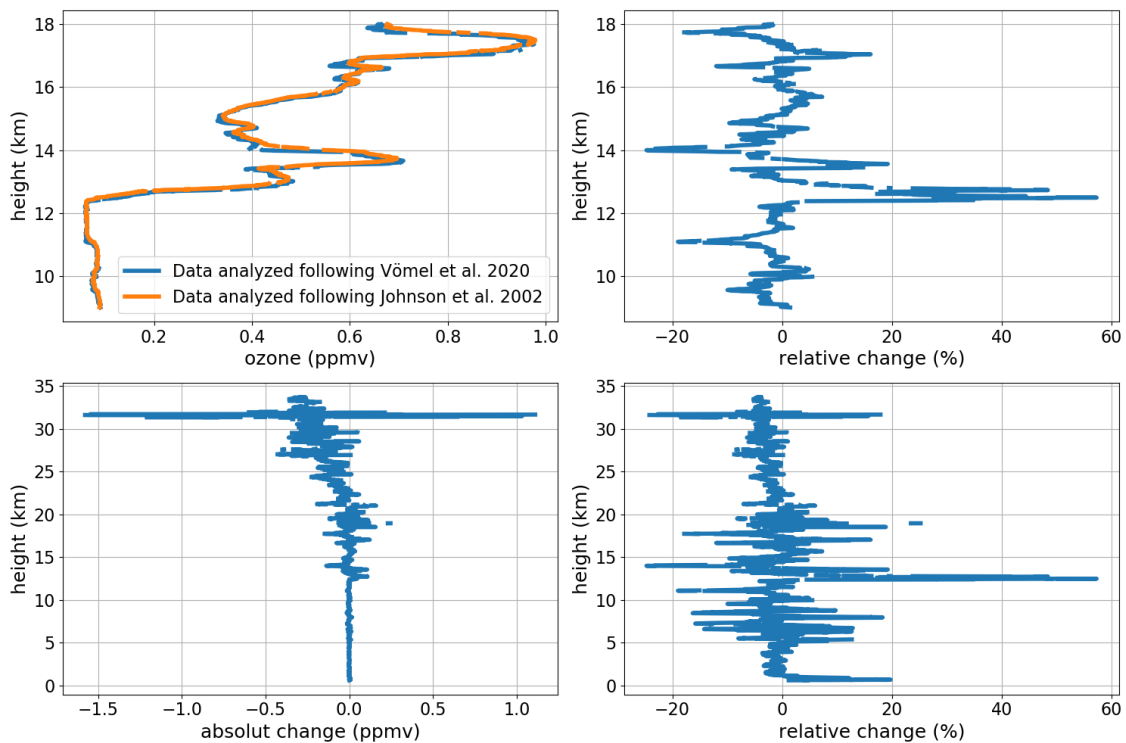


Figure 3.4: Effect of different data processing methods for an ozone profile. Upper left panel shows the data set analyzed with the two methods explained by Johnson et al. (2002) (orange) and Vömel et al. (2020) (blue). The upper right panel shows the relative difference of both methods in the UTLS. The lower panels show the absolute change (left) and relative change (right) of the entire profile.

3.3 Cryogenic frost-point hygrometer (CFH)

The Cryogenic Frost-point Hygrometer (CFH) is a balloon-borne instrument based on the cold mirror principle, which regulates the temperature of a mirror to the frost-point temperature of the ambient air (Vömel et al., 2007). Like most frost-point hygrometers it does only need calibration of the temperature sensor, which is typically long-term stable. However, a short conditioning, which includes a mirror cleaning and adjusting the set point of the mirror reflectivity prior to the flight, is necessary. The CFH is considered to be one of the few instruments capable of measuring both the tropospheric and stratospheric water vapor mixing ratios (Nash et al., 2010). The setup of the CFH is schematically displayed in Fig. 3.5. As the CFH rises after launch, lifted by the Helium balloon, the ambient air flows through a 34 cm long inlet tube. Halfway through this tube a mirror is located and on the opposite side an Light-Emitting Diode (LED) with a detector is positioned. The

temperature of the mirror is regulated to match the dew or frost-point temperature of the ambient air. This is achieved when the mirror is covered with a constantly thin dew or ice layer. An LED-light source emits infrared light toward the mirror, which is reflected and detected by a photo-diode. The percentage of the light reflected back to the detector depends on the thickness of the ice layer coverage on the mirror. Without the presence of an ice layer, the reflectivity is set to 88% in the lab prior to the start in order to ensure a stable background. During the flight this reflectivity is measured and kept constant by regulating the mirror temperature by a Proportional–Integral–Derivative controller (PID). Attached to the gold coated mirror a copper cold finger extends into a container with a cooling agent. The cooling agent would keep the temperature of the mirror at -80°C if there were not the counteraction of the heating coil, which is wrapped around the cold finger. The PID controller links the detector signal to the heating coil and hence it defines the reaction time of the mirror temperature to changes in the ambient humidity. The thermistor, which is attached 2 mm to the side of the mirror center, registers the change in temperature and is individually calibrated. The uncertainty of the thermistor is reported to be less than 0.02 K (Stuefer and Gordon, 2018). The total uncertainty of the CFH is described in Vömel et al. (2016) and summarized in Stuefer and Gordon (2018). The highest share of the CFH total uncertainty is assigned to the stability of the controller and is estimated to be less than 0.1 K. This results in a total uncertainty of less than 0.2 K under good conditions, including systematic errors. This leads to a relative uncertainty below 4% in the troposphere and below 10% in the stratosphere (Nash et al., 2010; Vömel et al., 2016). Klanner et al. (2021) use the CFH in comparison with the water vapor lidar system at the Zugspitze summit and find a very good agreement within their respective uncertainties throughout the entire atmospheric profile. Further, the CFH was used for the validation of the Far-Infrared Radiation Mobile Observation System (FIRMOS) instrument which is a demonstrator instrument for a new European Space Agency (ESA) space mission, the Far-infrared Outgoing Radiation Understanding and Monitoring (FORUM), aiming to investigate the Far-Infrared Range (FIR) spectral radiances (Palchetti et al., 2021). A potential additional uncertainty source of the instrument can be induced by liquid droplets

3.3. Cryogenic frost-point hygrometer (CFH)

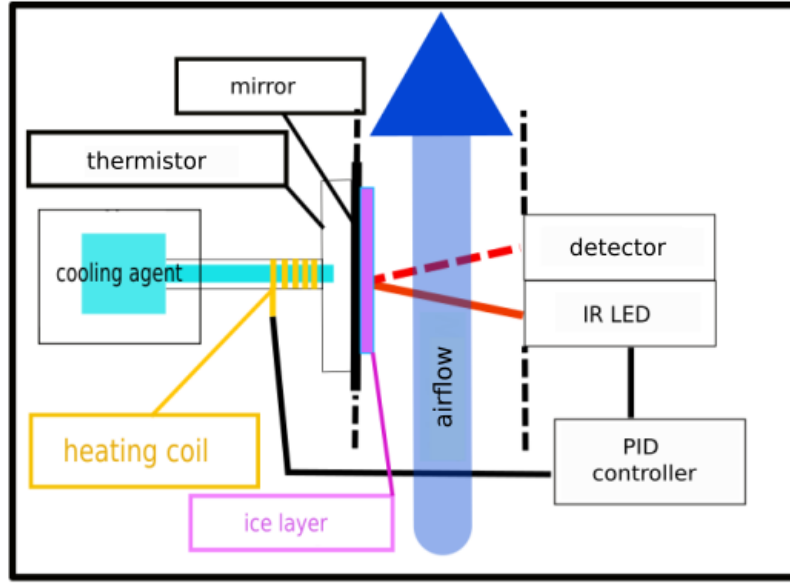


Figure 3.5: Schematic setup of the CFH instrument adapted from Vömel et al. (2007).

covering the detector, the mirror, or the light source leading to a strong oscillating behavior. Furthermore, liquid drops inside the inlet tube can distort measurement results by outgasing. It is therefore recommended that the CFH is not launched during rain. The CFH provides the dew-point or frost-point temperature which in turn is used to calculate the partial pressure of liquid water or ice by applying the equations from Murphy and Koop (2005), which is a numerical approximation of the CC and is given as:

$$\begin{aligned} \ln(e_{w,sat}) = & 54.842763 - \frac{6763.22}{T} - 4.210 \cdot \ln(T) + 0.000367 \cdot T \\ & + \tanh(0.0415 \cdot (T - 218.8)) \\ & \cdot (53.878 - \frac{1331.22}{T} - 9.44523 \cdot \ln(T) \\ & + 0.014025 \cdot T) \end{aligned} \quad (3.3)$$

for temperatures between 123 K and 332 K and

$$\log(e_{i,sat}) = 9.550426 - \frac{5723.265}{T} + 3.53068 \ln(T) - 0.00728332 \cdot T \quad (3.4)$$

for the frost-point with temperatures above 110 K. The $e_{w,sat}$ is the saturation water vapor pressure over water, T is the ambient temperature, and $e_{i,sat}$ is the saturation water

vapor pressure over ice. As the CFH is designed to operate under conditions of low pressure and low temperature, multiple aspects have to be considered. The insulation of all electronic parts is achieved by the styrofoam housing.

Additionally, the above mentioned cooling agent must fulfill a number of criteria. Firstly, it must not be flammable and not toxic for save operation procedures. Secondly, it must remain in liquid state during the whole flight, at pressure levels ranging from surface pressures down to at least 10 hPa and at temperatures ranging from the surface with up to 40 °C to -60 °C, which is prevailing in the extra-tropical UTLS region. Further, the liquid must maintain the cold temperature throughout the entire flight period which might take as long as 2.5 hours. The desired cooling temperature at which the cooling agent has to remain in liquid state is at least -80 °C at surface conditions and as low as -90 °C in the UTLS region. Currently, the only substance fulfilling this criteria is the haloform gas R-23. The transparent gas condenses at -82.1 °C releasing heat of evaporation, also know as evaporation enthalpy, during the phase change. The evaporation enthalpy of R-23 at its boiling point at normal conditions is relatively high with 16.7 kJ/mol. However, R-23 has a very strong greenhouse warming potential of 13856 which means that it has the ability to trap energy in the atmosphere 13856 times stronger compared to CO₂. Therefore, it is now strongly regulated and banned from the open market starting at 1 January 2020. Since then it is impossible to purchase R-23 in the European Union (EU) (EU, 2014). Due to this legislation a new cooling method had to be developed in the framework of this thesis and will be discussed in the following section.

3.4 Towards the development of a new CFH cooling agent

With the legal validity of the R-23 ban in the EU, a new method for the mirror cooling has to be developed. The requirements for a suited cooling alternative are summarized in the following:

- Preserve liquid state throughout the flight in order to maintain a good heat conduction and maintain the general setup of the instrument.

3.4. Towards the development of a new CFH cooling agent

- The cooling agent must be neither flammable nor toxic for a safe handling.
- The cooling efficiency must be large enough to keep the mirror at the frost-point temperature of the dry air masses in the stratosphere for the duration of the flight. Hence, a high enthalpy of evaporation of the cooling liquid is favorable.

The evaporation enthalpy is not constant and depends on the ambient temperature and can be calculated using the Watson equation as follows:

$$\Delta H_{v2} = \Delta H_{v1} \left(\frac{1 - \frac{T}{T_{crit}}}{1 - \frac{T_{sp}}{T_{crit}}} \right)^n \quad (3.5)$$

with ΔH_{v1} being the evaporation enthalpy at the boiling point, ΔH_{v2} the evaporation enthalpy at the needed temperature, T_{crit} is the critical temperature, T_{sp} is the temperature at the boiling point and n can be calculated according to

$$n = \left(0.00264 \cdot \frac{\Delta H_{v1} \cdot M}{R \cdot T_{sp}} + 0.8794 \right)^n \quad (3.6)$$

with R as the gas constant and M the molar mass of the investigated substance (Watson, 1943). Using this equations the evaporation enthalpy in dependence on temperature was calculated for a number of different cooling agent candidates in the relevant range of temperatures (see Fig. 3.6). Finally, we found three possible candidates for replacing R-23: frozen CO₂, ethanol, and liquid nitrogen. While ethanol has a very high heat capacity, it does not evaporate at the temperatures of interest with a boiling point at 78.32 °C. CO₂ on the other hand has a very similar evaporation enthalpy as R-23 but is in a solid state at the temperatures and pressures of interest. As a result of this conditions, only two possible solutions were identified. The first solution focuses on liquid nitrogen as a cooling agent. At surface pressure nitrogen has its boiling point at -195.8 °C and remains liquid until a temperature of -209.86 °C. However, with decreasing pressure the possible temperature range for the liquid phase decreases until its triple point at a pressure of 125 hPa which equals to 0.1 atm (see Fig. 3.7). This leads the nitrogen to congeal during the balloon flight in higher altitudes and thus disabling a good heat conduction between the CFH cold finger and the solid nitrogen. Thus, this solution requires a closed vessel

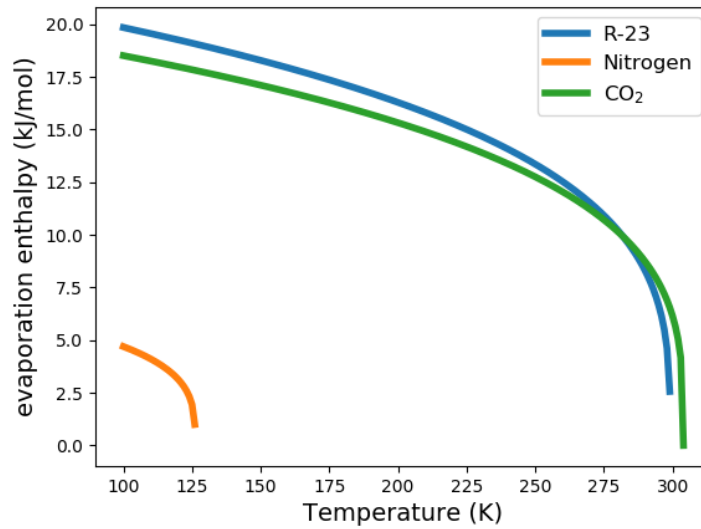


Figure 3.6: Enthalpy for R-23 (blue), CO₂ (green) and nitrogen (orange) in the temperature range between 100 K and 300 K according to equation 3.5 and 3.6.

for the liquid nitrogen with additional pressure valves allowing the container to be relieved from excessive pressures and preventing the container to burst, but keeping the pressure in the container higher than 125 hPa. This would allow nitrogen to remain at liquid state at ambient pressures as low as 10 hPa. This setup was tested in an environmental simulation chamber and showed promising results, but will not be further discussed in the framework of this thesis, as the second approach was preferred.

Another solution would be solid CO₂ (dry ice) placed in an ethanol bath, taking advantage of its high heat capacity. In contrast to water, ethanol remains liquid in the temperature range of -114.5 °C and 78.32 °C at surface pressure. This approach does not require further modification of the CFH instrument. This method was also tested in the climate chamber at the institute. The CFH was placed inside the atmospheric simulation chamber and filled with ethanol and dry ice. A temperature sensor was placed in the CFH cooling agent container and a pressure and temperature profile representing the atmosphere was set for the experiment. The results can be seen in Fig. 3.8. As expected the temperature of the ethanol decreased with decreasing pressure due to the reduction of the dry ice sublimation temperature which in turn cools the ethanol. The temperature of the CO₂-ethanol mixture decreased continuously for 2.5 h reaching the lowest temperature at

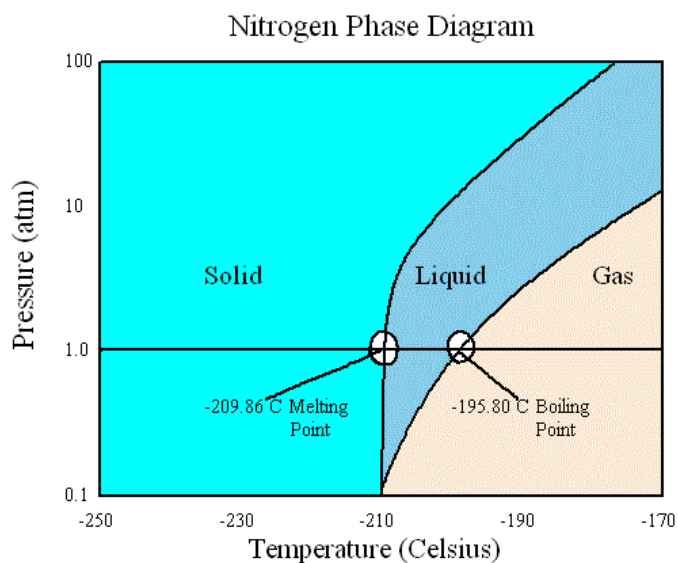


Figure 3.7: Phase diagram of N₂. Image from CHEMIX Chemistry Software.

-98.3°C before the temperature started to increase again with increasing chamber pressure. Based on these promising results, tests were performed on several balloon-borne flights. These test flights were performed with two CFHs attached to the payload together with an ECC (see Section 3). The payload can be seen in Fig. 3.9a. Two CFHs were attached to the ECC sonde in the middle. One of the CFHs was using R-23 as a cooling agent and the other one was filled with the CO₂-ethanol mixture. In each of the cooling liquid containers a thermometer was placed (PT100-thermistor) in order to record the temperatures of both cooling liquids. Figure 3.9b shows a close up picture of the cooling liquid container with the CO₂-ethanol mixture. Already within the previous experiments in the atmospheric simulation chamber it was realized that the size and the density of the dry-ice had an influence on the cooling efficiency. Too large pieces of dry ice did not have enough surface contact to the ethanol bath and hence the cooling efficiency was not strong enough. Too small parts of dry ice or even dry ice snow evaporate too fast and the cooling effect did not last throughout the presumed flight time of 2.5 hours. For the measurement using the CO₂-ethanol cooling agent some adjustments of the PID controller were necessary, as the temperatures of the dry ice-ethanol mixture do not reach as low temperatures as R-23 and hence have a lower cooling efficiency. Therefore it is necessary to adjust the PID circuit to react to temperature changes at the mirror. This

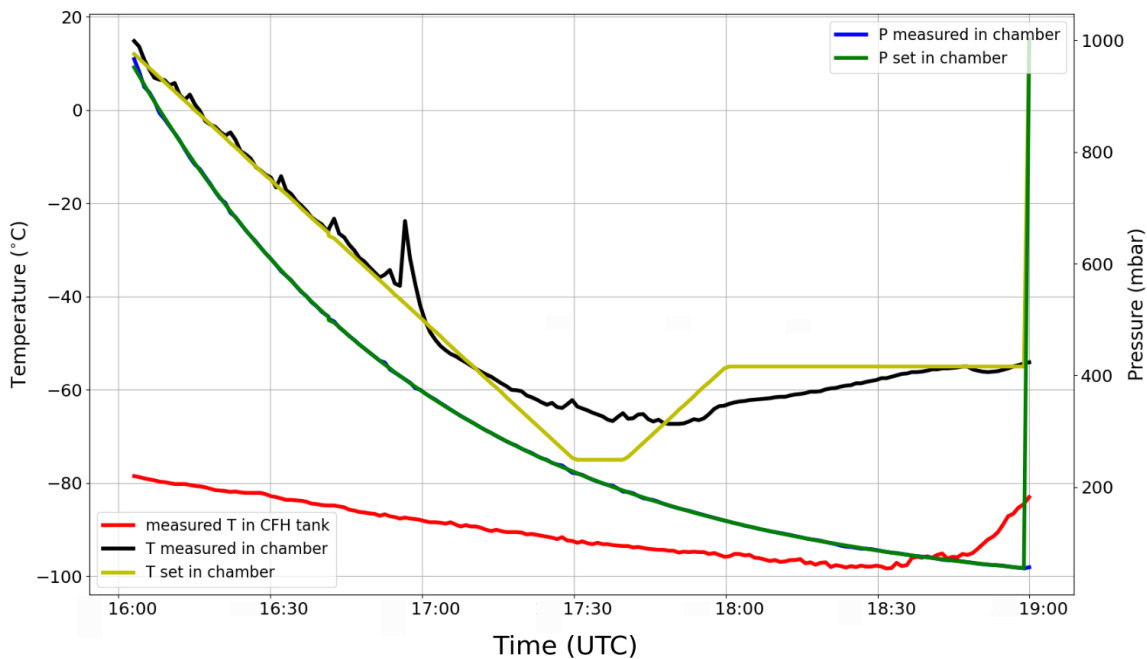


Figure 3.8: Measurement results of the atmospheric chamber experiment with CO₂-ethanol cooled CFH instrument. The blue line shows the pressure set in the chamber and the green line the pressure measured in the chamber. The yellow line shows the temperature set in the chamber and the black line shows the actual temperature measured in the chamber. The red line shows the temperature of the CO₂-ethanol in the CFH measured with a PT100-thermistor.

was performed in close collaboration with H. Vömel at National Center for Atmospheric Research (NCAR). The results of the first comparison flight can be seen in Fig. 3.10. The upper left panel shows the entire profile of both CFHs throughout the flight. One can see minor disagreements in the altitude levels between 5 and 15 km. The upper right panel shows the absolute deviation between both CFHs. While rather large deviations are predominant in the troposphere, values around 0 can be seen above the tropopause. This clearly results from high water vapor values in the troposphere, while the low water vapor values in the stratosphere, around 5 ppmv, explain the low deviation in the stratosphere. The mean absolute deviation throughout the profile is -1.1 ppmv and the standard deviation 125.6 ppmv. The median is -0.4 ppmv which indicates that no significant systematic bias by one of the CFHs is evident. In contrast, the relative deviation (lower right panel) exhibits a more constant range throughout all altitudes with some exceptions between 4 and 10 km. The average difference between both CFHs is 26.9% with a standard deviation of 97.1%, however the deviations at about 9 km have a strong influence on these

3.4. Towards the development of a new CFH cooling agent

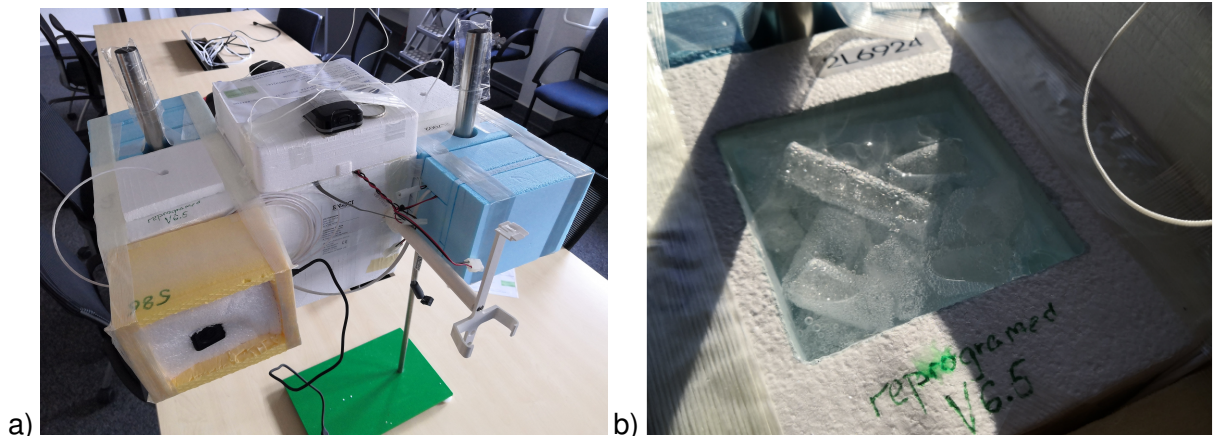


Figure 3.9: Payload of a CFH test flight. a) Two CFHs are attached to both sides of the ECC box. In the cooling agent container temperature sensors were placed to record the temperature of the R-23 (right CFH) and CO₂-ethanol mixture (left CFH). In the yellow Styrofoam box a camera is placed to film the flight. b) Close up picture of the dry ice size and density in the cooling liquid container shortly before the test flight.

values. Due to this bias the median is more representative, which is -1.5% . There is no strong bias evident in the correlation between both instruments throughout all altitudes with a correlation coefficient of 0.985 (lower left panel in Fig. 3.10). The analysis of the flight data revealed that the cooling effect is not sufficient for fast changes of the water vapor mixing ratio and thus fast changes of the mirror temperature. In particular, this is evident on a closer look on the frost point time series of the flight (see Fig. 3.11). At ambient temperatures of -15°C and of -52°C the CFH performs a reconditioning of the ice layer to ensure a good coverage on the mirror surface. Therefore, the CFH first removes the ice layer by performing a strong heating pulse and afterwards a strong cooling to build a new ice layer. The data around the peak are usually excluded from the water vapor measurements. However, for the characterization of the cooling efficiency at the heating peak, it reveals how fast the CFH is returning back to equilibrium, where the mirror is covered with a thin layer of ice again. The CFH-R23 achieves its equilibrium 17 s after the first heating peak at -15°C ambient temperature and 30 s after the second heating peak at -52°C ambient temperature. The CFH-CO₂ needs significantly longer time with 77 s after the first and 292 s after the second heating peak. This demonstrates that the heating rate of the CFH-CO₂ is not sufficient to react fast enough to a small scale variation of water vapor in the UTLS which is a crucial point for the CFH. The temperature

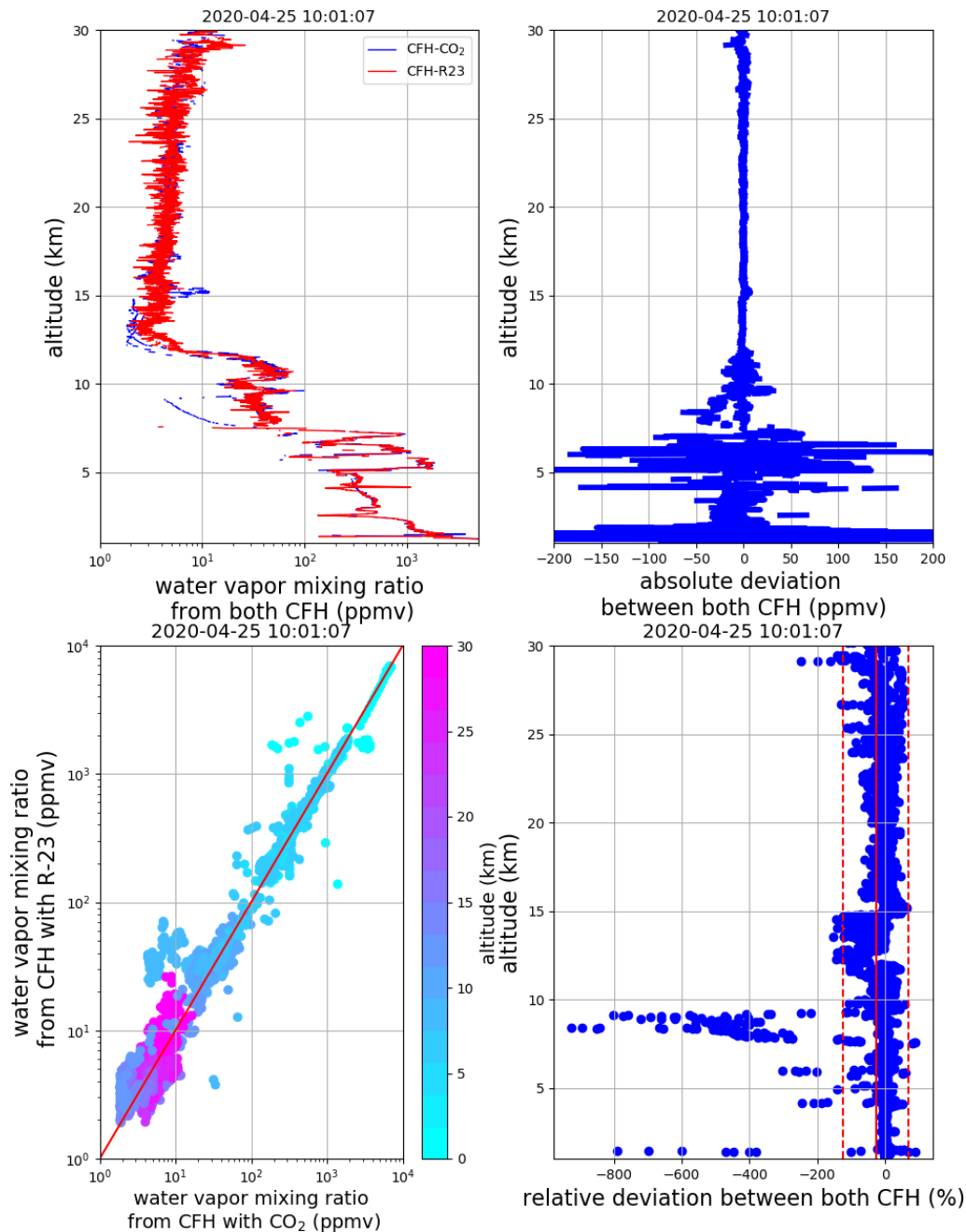


Figure 3.10: Comparison of CFH-R23 and CFH-CO₂ from the flight on 25 April 2020. In the upper left panel the whole profile of the flight is presented, showing the water vapor mixing ratios measured by both CFHs. In the upper right panel the absolute deviation between both instruments is shown. The lower left panel shows the correlation plot of both CFHs with altitude color-coded. The lower right panel shows the relative deviation between both instruments with the average (red solid line) and standard deviation (red dashed lines).

of the cooling agent mixture itself can be seen in Appendix B Fig. B.2. The ethanol-CO₂ mixture reaches lower temperatures as previously measured in the atmospheric chamber

3.4. Towards the development of a new CFH cooling agent

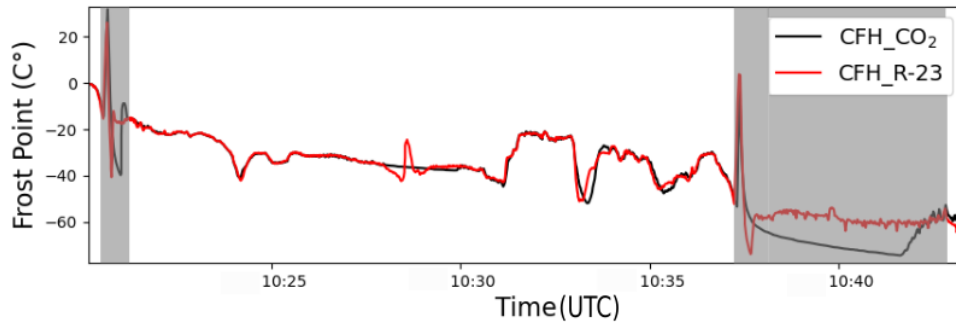


Figure 3.11: Timeseries of the CFH-R23 and CFH-CO₂ frost-point temperature from the flight on 25 April 2020. The shaded regions mark the response times of the CFH-CO₂ after the initial heating pulses.



Figure 3.12: Picture of the copper plate mounted to the cold-finger of the CFH-CO₂. with a minimum temperature of $-116.18\text{ }^{\circ}\text{C}$, $17.88\text{ }^{\circ}\text{C}$ less than inside the chamber. In order to improve the efficiency of the cooling agent, a copper plate was mounted at the CFH cold finger as shown in Fig. 3.12. Copper has a high heat conductivity of $386\text{ W m}^{-1}\text{ K}^{-1}$ at standard conditions which increases with decreasing temperatures (Carvil, 1993). The temperature heat conductivity dependence of copper is shown in Appendix B in Fig. B.1. Within the temperature range relevant for atmospheric balloon profiles, the thermal conductivity of copper slightly increases to $413\text{ W m}^{-1}\text{ K}^{-1}$ at $-73\text{ }^{\circ}\text{C}$. By enlarging the contact area of the cold finger to the cooling agent with the copper plate, the cooling efficiency is expected to increase. With this modified CFH a second test flight was performed. The results can be seen in the Fig. 3.13 and Fig. 3.14. As expected, the performance of this test flight shows improved cooling efficiency of the CFH-CO₂. The temperature of both

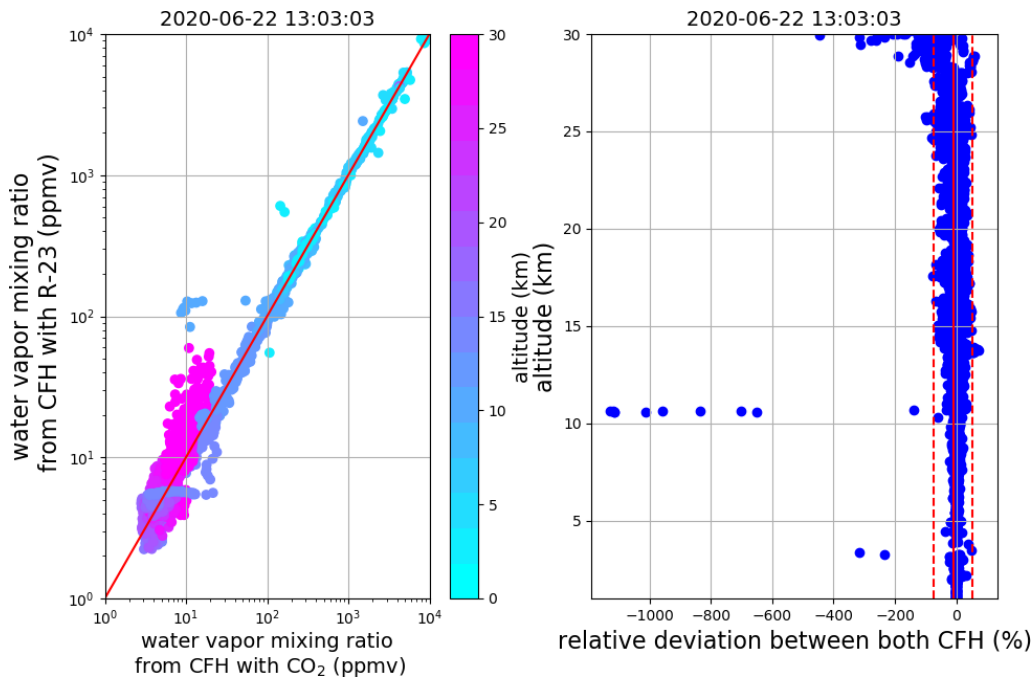


Figure 3.13: Comparison of CFH-R23 and CFH-CO₂ from the flight on 22 June 2020. The left panel shows the correlation of both CFHs with altitude color-coded. The right panel shows the relative deviation between both instruments with the average (red solid line) and standard deviation (red dashed lines).

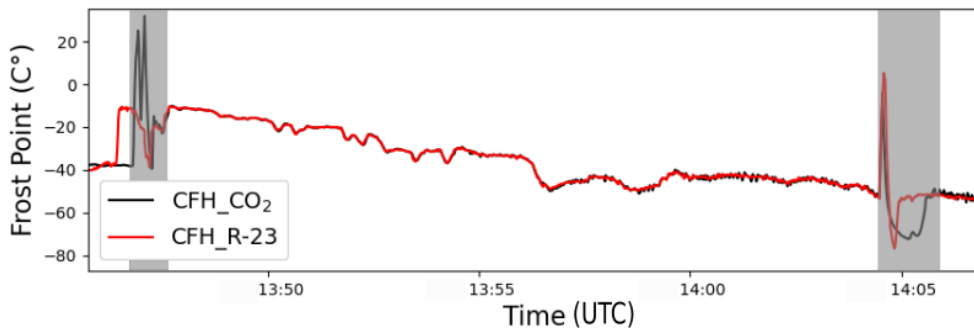


Figure 3.14: Timeseries of the CFH-R23 and CFH-CO₂ frost-point temperature from the flight on 22 June 2020 for comparison of the cooling efficiency. The shaded regions mark the response times of the CFH-CO₂ after the initial heating pulses.

cooling agents throughout the flight is shown in the Appendix B Fig. B.3. The correlation of both CFHs can be seen in Fig. 3.13 lower left panel with a correlation coefficient of 0.994. The relative deviation values are shown in the lower right panel. The variation of the relative deviation decreased significantly with relative mean deviation of -10.3%, a median of -0.8% and a standard deviation at 62.35%. The statistical parameters clearly show an improvement by the use of the copper plate and are summarized in Table 3.1.

3.4. Towards the development of a new CFH cooling agent

Table 3.1: Statistical evaluation of the comparison flights on 25 April 2020 and 22 June 2020. With the exception of the mean absolute deviation, all parameters improved on the second flight when the copper plate was attached to the cold finger of the CFH-CO₂.

	Flight without copper plate	Flight with copper plate
mean of absolute deviation	-1.1	5.1
std of absolute deviation	125.6	70.8
median of absolute deviation	-0.4	-0.2
mean of relative deviation	-26.9	-10.3
std of relative deviation	97.1	62.4
median of relative deviation	-1.5	-0.5
correlation coefficient	0.985	0.994

Figure 3.14 demonstrates, similar to Fig. 3.11, the frost-point temperatures of both CFH mirrors with the two reconditioning peaks. The recovery time to equilibrium conditions of the CFH-CO₂ is again slower compared to the CFH-R23, however, it is much faster compared to the first flight without the copper plate (Fig. 3.11). For the first heating peak at a temperature of -15 °C, the CFH-R23 returns to equilibrium 13 s after the heating peak is initiated, while the CFH-CO₂ still needs 60 s. For the second heating peak at -52 °C, the CFH-R23 returns to equilibrium 30 s after the reconditioning peak is initiated, while the CFH-CO₂ needs about 70 s. For the first heating peak the performance has improved by 17 s and for the second peak by 222 s.

While the cooling efficiency still needs further improvements to match the performance of the CFH-R23, the addition of the copper plate already brought large and also promising improvements. The CFH-CO₂ relative deviation of $\approx 10\%$ is in the range of relative error of the CFH in the stratosphere. Further improvement could be achieved by a larger copper plate or the use of a metal with a higher heat conductivity (e.g. silver) and a better contact between the copper plate and cold finger by using cryogenic high vacuum grease. A redesign of the cold finger as a whole with a larger surface within the cooling agent would be another solution. Overall, it can be concluded that the experiment with the ethanol-CO₂ mixture as a replacement for R-23 was successful, but further modifications of the copper plate design and a PID controller adjustment are necessary before a complete transition to this method can be implemented. As the purchase of R-23 is already unfeasible in many parts of the world, this transition is unavoidable. However, it

has to be mentioned that the minimum temperature reached by the ethanol-CO₂ mixture is $\approx 10^\circ\text{C}$ warmer at the tropopause compared to the temperature reached by the R-23 as can be seen in Appendix B, Fig. B.3. This might not be sufficiently low for the lower tropopause temperatures in tropical regions.

Chapter 4

Case study of the impact of severe convective storms on the water vapor mixing ratio in the lower mid-latitude stratosphere observed in 2019 over Europe

In this study data collected during a MOSES measurement campaign in 2019 to investigate the impact of convection on the lower stratospheric humidity is analyzed. The content of this chapter is published in Khordakova et al. (2022).

The campaign took place from the middle of May to the end of July as part of a collaboration of 8 Helmholtz Association research centers. The objective of the measurement campaign was to capture extreme hydrological events throughout the different Earth compartments: atmosphere, ground and running waters. In the Eastern Ore Mountains (Osterzgebirge) in Germany, close to the city of Dresden, a 3-month measurement campaign with Intense Operational Phase (IOP)s, was performed. During these IOPs the

teams operated on demand to capture the development and cycle of convective events. The main measurement site was located adjacent to Börnchen village in the low mountain range at 50.805°N and 13.80°E . The team from Forschungszentrum Jülich (FZJ) focused on small-scale deep convective events and their impact on the stratosphere. As showed in previous studies extreme convective events can transport moist and ozone rich tropospheric air masses into the LS (Smith et al., 2017). The objective was to capture such an event in order to better understand the impact of convective storms on the LS especially over Europe. During the campaign period two of these events occurred and were observed with balloon-borne measurements. In this chapter a case study of the water vapor transport into the extra-tropical lower stratosphere is presented. Water vapor was injected by deep convective events over Europe. The analysis is based on balloon-borne light-weight instruments, which recorded water vapor, ozone, temperature and pressure immediately before and after a thunderstorm with strong convection that passed the measurement site. Such observations can be rarely made due to the difficulty to predict such events. Two cases of overshooting convection on two consecutive days (10 and 11 June 2019) are discussed in this study. Both cases show that significant amounts of water vapor can be transported into the lower stratosphere by deep convective events over central Europe and not just in the North American and Asian Monsoon regions. It is shown that water vapor mixing ratios in the same order of magnitude as the data recorded over North America can also be found deep in the extra-tropics over central Europe. Using back trajectories as well as fifth generation of ECMWF atmospheric global reanalysis (ERA5) and Microwave Limb Sounder (MLS) data, the entry point of the tropospheric air masses transported into the stratosphere is analyzed. Section 4.1 introduces the instruments and methods used, while sections 4.2.1, 4.2.2, and 4.2.3 describe the two events and the results of the balloon profile measurements. In section 4.2.4 the data are compared to ERA5 reanalysis, while in section 4.2.5 the time and location of the origin is discussed using backwards trajectories and satellite data. In section 4.3 the results are discussed, and section 4.4 concludes the outcome of the study.

4.1 Data and methods

4.1.1 Balloon measurements within MOSES

Figure 4.1 schematically shows the measurement procedure. As a convective cell was approaching the measurement site, two weather balloons were launched to measure the state of the atmosphere. The first balloon was launched just before the convective cell reached the measurement site; the second balloon was launched immediately after the storm cell passed the measurement site as soon as the rain stopped. Two kinds of measurement balloons were used. The first version is a 200 g latex balloon equipped with a Vaisala radiosonde RS41-SGP, which recorded the location of the balloon as well as the altitude, pressure, temperature and moisture of the atmosphere and transmitted the data to the ground station at the measurement site. The temperature sensor of the radiosonde has an uncertainty of 0.3 K below 16 km and 0.4 K above. The uncertainty of the humidity sensor is given as 3% and the pressure sensor has an uncertainty of 1.0 hPa at ambient pressure above 100 hPa; 0.3 hPa between 10 and 100 hPa and 0.04 hPa below 10 hPa. Survo et al. (2014) report a temperature dependency of the humidity sensor uncertainty, which does not exceed 3% RH at temperatures below -80°C and RH below 30%. The second version is a 1500 g balloon additionally equipped with a payload carrying multiple in-situ instruments. An ECC (Electrochemical Concentration Cell) instrument (Smit et al., 2007) was used to measure ozone mixing ratios with an uncertainty of $\approx 5\%$ below 20 km (Smit et al., 2007; Thompson et al., 2019; Tarasick et al., 2021), and a CFH (Vömel et al., 2007) was used to measure the low water vapor concentration prevailing in the tropopause region and in the stratosphere. The uncertainty of the CFH instrument is given as 4% in the troposphere and below 10% in the stratosphere. The payload also contained a COBALD to measure backscatter from different types of particles during nighttime (Brabec et al., 2012). This is referred to as "large payload" in the following. However, the measurements taken by the COBALD instrument were not used for the analysis presented here. A picture of the entire payload with radiosonde, ECC, CFH and COBALD is shown in Fig. 3.1. The payload is adapted from the setup used by the

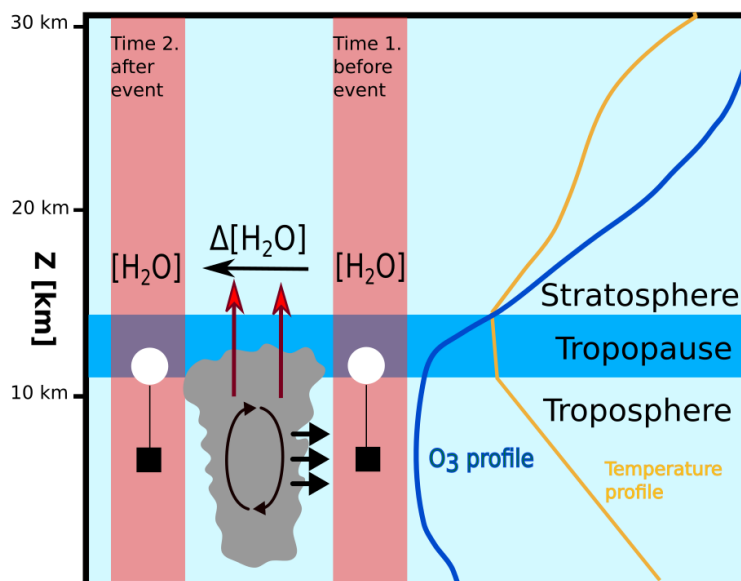


Figure 4.1: Schematic of the measurement strategy. A balloon is started right before and immediately after a deep convective event has passed the measurement site. On the right hand side the approximate ozone (blue) and temperature (yellow) climatological profiles are shown. The amount of water vapor transported into the stratosphere is investigated by the difference between the two profiles above the lapse rate tropopause according to the WMO definition.

GRUAN setup (Dirksen et al., 2014). A more detailed description of the instruments can be found in the Chapter 3. During the first event, on 10 June 2019, one radiosonde and one large payload was launched, while only 5 radiosondes were used during the second event, on 11 June 2019 due to logistical reasons. In most cases, the balloons reached far into the stratosphere reaching altitudes of up to 22 km with radiosondes only and up to 35 km with larger balloons, which were equipped with the above-mentioned instruments and captured the entire UTLS region during ascent and descent. During the first balloon launch of the first convective event the connection to the radiosonde was lost for about 20 minutes, and the data between 11 km and 18 km altitude were lost during the ascent, but all other sounding data were complete.

4.1.2 Aura Microwave Limb Sounder (MLS)

The Microwave Limb Sounder is an instrument operating onboard the Aura satellite. The sun-synchronous polar orbit satellite has an inclination of 98° and an equator-crossing

time of 13:45 Coordinated Universal Time (UTC) ± 15 min. It was launched on 15 July 2004 and has been operating ever since. The measurements are in limb-viewing geometry on the A-Train orbit and are in the spectral range of thermal emission, thus day- and night-time measurements are available. Temperature and pressure are retrieved from the 118 Gigahertz (GHz) band, water vapor from the 190 GHz band and ozone and CO from the 240 GHz band (Schoeberl et al., 2006; Waters et al., 2006). In this work, data from the version 4 retrieval algorithm was used to obtain the data presented. In this study ozone, water vapor and CO mixing ratios are shown. MLS Version 4 data is provided on 36 different pressure levels ranging from 316 hPa to 0.002 hPa as described in Livesey et al. (2017) and the data quality is described in Pumphrey et al. (2011b). One of the main improvements of Version 4 is improved cloud detection, excluding cloudy radiances causing corrupted profiles. This improvement increases the quality of the data set as the area of interest is covered with clouds.

4.1.3 ECMWF ERA5

The European Centre for Medium-Range Weather Forecasts (ECMWF) produces numerical weather forecasts and provides a meteorological data archive. In this study, ERA5 which is a global reanalysis covering the period from 1979 until present (Hersbach et al., 2020) is used. The spatial resolution is about 30 km and contains 137 vertical levels from the surface to an altitude of 80 km. In this work ERA5 reanalysis data from May to June 2019 was used with hourly temporal resolution. The reanalysis data set was interpolated to isentropic levels and potential vorticity (PV) was added to the individual isentropic levels (Ertel, 1942). In the Northern Hemisphere PV values above 2 PVU are typical for the stratosphere, while values below 2 PVU are typical for the troposphere, where $1 \text{ PVU} = 1 \cdot 10^{-6} \text{ km}^2 \cdot \text{kg}^{-1} \cdot \text{s}^{-1}$ (Kunz et al., 2011a). Additionally, the vertical gradient of potential temperature, which is part of the PV definition, defined as:

$$PV = -g \cdot (\zeta + f) \cdot \frac{\partial \theta}{\partial p} \quad (4.1)$$

is calculated, where g is the gravitational acceleration, ζ the relative isentropic vorticity, f the Coriolis parameter, θ is the potential temperature and p is the pressure. The vertical gradient of potential temperature is $\frac{\partial\theta}{\partial p}$ and is hereafter referred to as $d\theta$. $d\theta$ is negative by definition, as with decreasing pressure the potential temperature increases in a stable atmosphere. In the troposphere, potential temperature shows only a slight increase and can thus be considered constant relative to the steep increase that occurs above the tropopause.

4.1.4 Trajectory calculation

In order to calculate backward and forward trajectories of the measured air masses the trajectory module of the three-dimensional chemistry transport model Chemical Lagrangian Model for the Stratosphere (CLaMS) (McKenna et al., 2002) was used. The trajectories were initialized at pressure levels between 135 hPa and 175 hPa in steps of 5 hPa which encompasses the pressure level of the maximum water vapor enhancement measured for both cases using the same method as described in Rolf et al. (2018). Each trajectory was calculated both for 100 hours backward and forward in time. The trajectory calculation with CLaMS is based on the ERA5 horizontal wind fields and diabatic heating rates with an hourly output. In addition, temperature, pressure, PV, water vapor and ozone mixing ratios as well as CAPE are interpolated from ERA5 onto the coordinate of the trajectories.

4.2 Measurement results and analysis

4.2.1 Meteorological situation at the time of the case study

From 10 to 12 June 2019 multiple severe convective storms developed over Germany. During these events, hail with a diameter of up to 6 cm was observed and heavy rain with a daily amount of 100 mm was measured. Wilhelm et al. (2020) describe this series of convective storms in detail. In this study, the events that precede the measurements taken on the evening of 10 June 2019 are defined as Case 1 and the ones preceding

4.2. Measurement results and analysis

the measurements taken in the evening of 11 June 2019, as Case 2. The storm of Case 1 passed the measurement site at approximately 20:00 UTC on 10 June 2019. On the previous day, a low pressure system with warm and humid air was brought to Central Europe while a strong wind shear caused by a lee depression was located over the Czech Republic. A first convective storm developed in the north-eastern part of Italy and progressed westwards until it started dissipating at around 08:00 UTC over the north-eastern part of Italy. Later in the day, in combination with strong solar radiation, these storm precursors caused the first significant convective cell over Memmingen (southern Germany) at around 16:00 UTC. This cell developed into a super cell and caused severe damage in northern Munich at around 17:45 UTC. Multiple super cells subsequently formed, combined over eastern Germany, and later moved towards Poland and the Baltic Sea. The formation of super cells passed the measurement site in the Eastern Ore Mountains and balloon profiles were taken before and after the storm cell passed. The first balloon was launched at approximately 18:00 UTC (hereinafter referred to as "profile before") equipped only with a radiosonde. The second balloon launch, with a large balloon payload, took place at 01:00 UTC the next day, shortly after the thunderstorm passed.

On 11 June 2019, the already warm and humid air mass was heated up to 33 °C at ground level in the afternoon. At 12:00 UTC a first convective cell developed over the Slovenian/Austrian border and further developed over the next 7 hours to a mesoscale convective system (MCS) covering almost all of Austria and Slovenia. With an offset of approximately 1 hour another convective cell emerged over the center of northern Italy and multiple smaller cells developed over the German-Czech border starting at around 15:00 UTC. All these convective cells increased spatially throughout the day and unified to an MCS covering the entirety of eastern Germany. At around 17:39 UTC a first cell developed between Dresden and Bautzen. Hail with particles reaching a diameter of up to 4 cm was observed. This event, subsequently referred to as Case 2, was captured only with radiosondes that were launched every 3 hours starting from 13:00 UTC until midnight when the last radiosonde was launched after the storm had passed the measurement site.

4.2.2 Water vapor injection captured by balloon profiles

The measurement results of Case 1 and Case 2 can be seen in Fig. 4.2 and 4.3. The measurements before and after the respective extreme convective event (hereinafter referred to as "the event") are displayed with ascending and descending profiles, where available. The UTLS intercept is shown with pressure levels between 240 hPa and 90 hPa and potential temperatures ranging between 320 K and 420 K. A sharp transition from the characteristics of tropospheric to stratospheric air masses is clearly discernible in all figures. The lapse rate tropopause (LRT), as defined by the World Meteorological Organization (WMO), is at a pressure level of 203 hPa before and at 196 hPa after the convective event for Case 1 (see Fig. 4.2) and at 194 hPa before and at 200 hPa pressure level after the event for Case 2 (see Fig. 4.3). In all cases, the cold point tropopause (CPT) is slightly (4-20 hPa) above the LRT. For Case 1, the sharp transition from the troposphere to the stratosphere is discernible by a distinct change in the course of the temperature. Additionally, an abrupt increase in ozone and a decrease of the water vapor mixing ratio towards the stratospheric background level below 5 ppmv show the difference between the two regimes. Between pressure levels of 180 hPa and 162.5 hPa, which correspond to potential temperature levels of 345 K and 357.5 K, the water vapor mixing ratio fluctuates between 5 ppmv and 7.4 ppmv and between 6 ppmv and 14.5 ppmv as measured by the radiosonde and the CFH respectively, before it attains the stratospheric background value of $\approx 4-5$ ppmv, which is reached within all Case 1 profiles below the 160 hPa/360 K level. A background value of ≈ 5 ppmv agrees well with results of previous studies (Pan et al., 2000). The ascent profile measured after the event shows a strong increase in water vapor measured by the radiosonde as well as by the CFH above the level of 155 hPa/365 K. The maximum value measured by the RS41 is $7.0 (\pm 10\%)$ ppmv and the maximum value measured by the CFH is $8.6 (\pm 6\%)$ ppmv. The lagging response time of the RS41 may explain most of the difference between the CFH and the radiosonde observations as described in Chapter 3. Above the water vapor enhancement, at 143 hPa/375 K, the mixing ratio decreases rapidly again to the background value below 5 ppmv. This peak is only apparent in the ascending profile of the measurement. The descending profile shows

no peak signatures either in the CFH or in the RS41 water vapor measurements. As the horizontal distance between the location during ascent and descent at this altitude is only 60 km and about 2 hours (00:59 UTC/02:49 UTC) time difference, the enhancement in the water vapor mixing ratio observed during ascent, is a localized feature. In Fig. 4.2a and b, the vertical extent of the discussed water vapor peak are framed with a gray background. A striking peak in the ozone profile is evident at a similar level as the peak in water vapor. With a lower edge at 162 hPa/359 K and an upper edge at 145 hPa/373 K the ozone peak starts at a lower level compared to the water vapor enhancement, but is limited by the same upper edge. This ozone peak is not associated with the overshooting event and the cause is discussed in Section 4.2.3. Within this peak a steep decrease of the ozone mixing ratio occurs very sharply at the same potential temperature level as the sudden appearance of the water vapor peak, which becomes especially evident in Fig. 4.3b. This is a major indicator of the in-mixing of tropospheric air into this level, which has a low concentration of ozone and a high amount of water vapor. Figure 4.2b clearly demonstrates that the air mass with increased water vapor also has diluted mixing ratios of ozone as the ozone mixing ratio decreases sharply at the same level as the strong increase in water vapor appears. Further evidence of the tropospheric origin of the air mass can be seen when considering the temperature profile. The temperatures typically increase with altitude throughout the stratosphere. In the measured ascent profile, after the temperature dropped to 207.9 K at the CPT, it increases until it reaches 220.4 K at a potential temperature level of 365 K where it declines sharply to 218.63 K. In Fig. 4.2b it becomes evident that the larger temperature dip of ≈ 2 K occurs suddenly at 365 K, the same level as the strong decrease within the ozone peak. The temperature drop within the water vapor enhancement might be a result of mixing with the strongly adiabatic cooled tropospheric air within the overshooting top and the warmer stratospheric air masses in the surrounding. In addition, evaporation/sublimation of cloud particles in this warmer and dryer mixing area around the overshooting top can also lead to further cooling.

Case 2 presents a slightly different background atmosphere than Case 1. The transition

from the tropospheric to the stratospheric regime proceeds less abruptly as is depicted in Fig. 4.3a and b (the water vapor mixing ratios of the flight launched at 13:14 UTC with the RS41 was corrected for an off-set bias). The CPT is further above the LRT and the CPT temperature minimum is less distinct. For Case 2 multiple background profiles exist, launched throughout the day, before the occurrence of the convective event in the night. To simplify the figure, only the tropopause of the last profile before the event is shown in Fig. 4.3a and b. The water vapor profile shows a similar feature as Case 1. As the water vapor mixing ratio converges to the background value, it is first disrupted by a peak reaching a value of 6.5 ppmv and returning to the background value at a pressure/potential temperature level of 153 hPa/365 K, respectively. At this elevation a second peak is discernible with water vapor mixing ratios of 12.1 ppmv ($\pm 10\%$) at 143 hPa/371 K. As multiple balloon launches were performed throughout the day, an increase of background water vapor mixing ratios with progressing launch time is evident. Balloon profiles launched at 19:00 UTC and 22:00 UTC show a slight water vapor enhancement up to 5.5 ppmv ($\pm 10\%$) at the same level as the main peak measured in the ascending profile after the event. The descending profile also shows an increase in water vapor mixing ratio at the same pressure altitude as the ascending profile. However this peak is wider and only about half the amplitude. Similar to Case 1 the temperature measured during ascent shows a sharp decrease of 2 K at the potential temperature level of the highest water vapor mixing ratio value of the peak. In Case 2 the water vapor peak is more spiked compared to the rectangular profile visible in Case 1 (shown in Fig. 4.2a and b). It is of further interest that all temperature profiles measured on 11 June 2019 clearly show a second tropopause at about 110 hPa while the temperature profiles of Case 1, measured only a couple of hours before do not show such a structure.

4.2.3 Source of the ozone peak at 150 hPa

Figure 4.2a shows the profile measured after the event of Case 1. A strong ozone peak with values of up to 696 ppbv can be seen starting somewhat below the water vapor peak at a pressure level of 150 hPa. Usually, it is expected to find a negative correlation be-

4.2. Measurement results and analysis

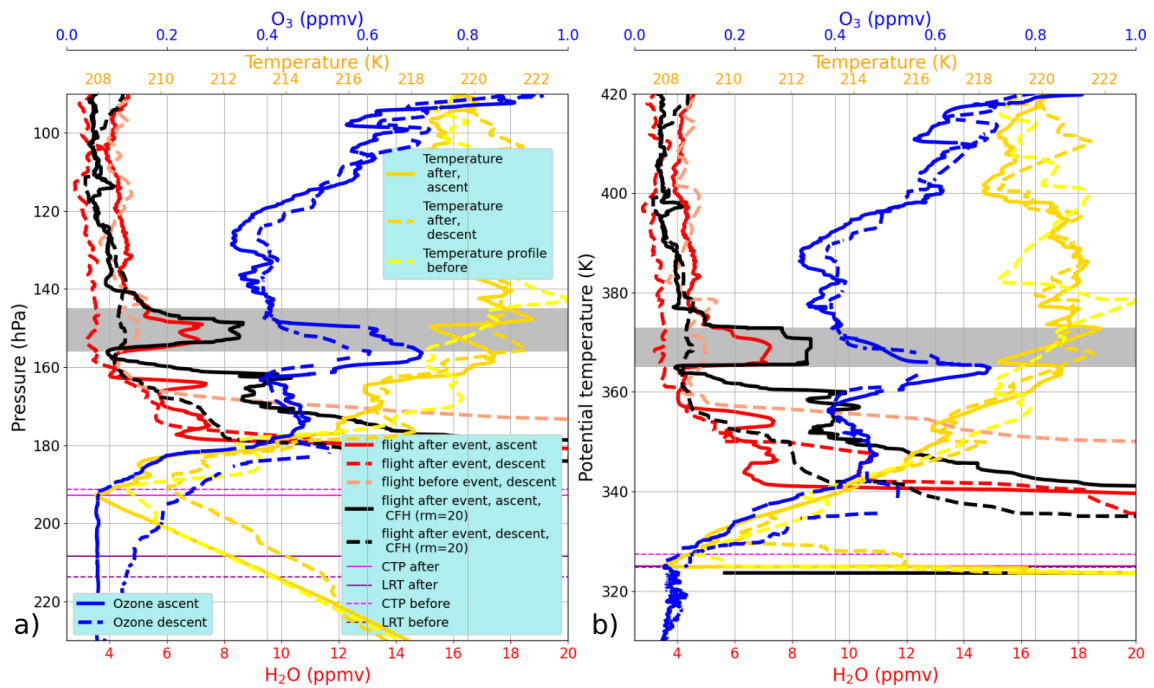


Figure 4.2: Profiles measured immediately before and after the convective event (Case 1) at 18:00 UTC on 10 June 2019 and 00:00 UTC on 11 June 2019 in the UTLS region. The water vapor measurements are shown in reddish colors for the RS41 and in black for the CFH instrument. Ozone measurements are depicted in blue. Temperature is shown in yellowish colors. a) Pressure is used as vertical coordinate. b) Potential temperature is used as a vertical coordinate. The different tropopauses (LRT, CPT) are shown as horizontal lines. The gray regions mark the level between 145 hPa and 165 hPa in a) and between 365 K and 370 K in b) in which the water vapor enhancement is observed.

tween water vapor and ozone when tropospheric air masses are injected by overshooting convection into the stratosphere. It is therefore unexpected to find such a strong increase (about 300 ppbv) in ozone at the same level as the water vapor injection. Figure 4.2b shows a steep decrease of ozone mixing ratios at potential temperature levels between 365 K and 375 K. This indicates a dilution of the ozone-rich stratospheric air with ozone-poor tropospheric air. However, the origin of the ozone peak between the 160 K and 375 K potential temperature level, has to be clarified. Multiple possible explanations might be considered. One suggestion linked strong increase in ozone to the injection of increased NO_x produced by severe lightning (Seinfeld and Pandis, 2016; Bond et al., 2001; Cooray et al., 2009). NO_x is controlling the O₃ concentration in the troposphere and is mainly responsible for the development of photochemical smog in the troposphere. However, the increase of ≈ 300 ppbv cannot be explained by that because model simulations show that

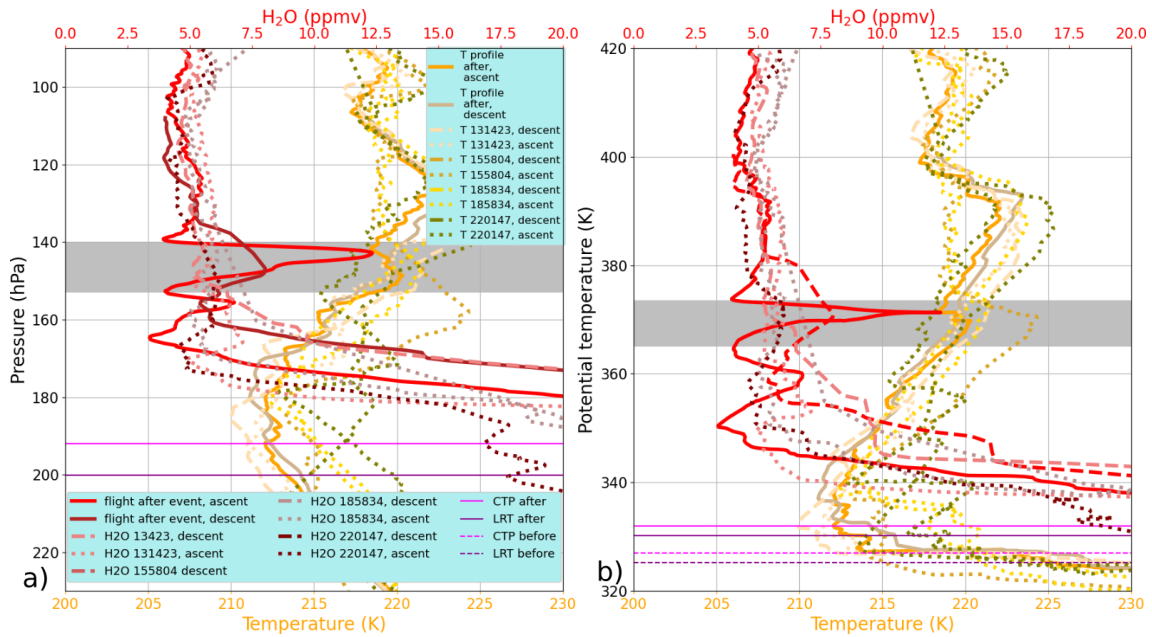


Figure 4.3: Same as Fig. 4.2 but for profiles measured immediately before and after the convective event on 11 June 2019 (Case 2) that passed the measurement site in the UTLS region. The water vapor mixing ratios is shown in red, measured by the radiosonde before and after the event. a) Pressure is used as a vertical coordinate. b) Potential temperature is used as a vertical coordinate.

the potential increase due to NO_x would be in the order of 10 ppbv (DeCaria et al., 2005). Another ozone source can be direct corona discharge during lightning leading to ozone formation (Minschwaner et al., 2008; Bozem et al., 2014; Kotsakis et al., 2017). However, the enhancement of ozone due to this process is reported to be in the order of about 50 ppbv and thus cannot explain the increase in the observed range. Figure 4.4a shows the ozone profile measured after the event during Case 1 in comparison to the mean of all ozone profiles (8 available profiles) with multiple balloon measurements in Germany during spring and summertime measurements between 2018 and 2020. It is evident that although the profile of Case 1 clearly exceeds the mean ozone profile at this altitude, it is not out of the observed range analyzed here. Figure 4.4b displays the H_2O - O_3 distribution of the same data as in the left panel. Here, the data from Case 1 (red dots) with the high amount of ozone and water vapor diverge prominently from the typical L-shaped data set (gray dotted data), which marks the tropospheric and stratospheric regimes. It is not unusual that vertically thin filaments of ozone-rich stratospheric air masses are transported horizontally causing local ozone enhancements in vertical profiles. A model run

4.2. Measurement results and analysis

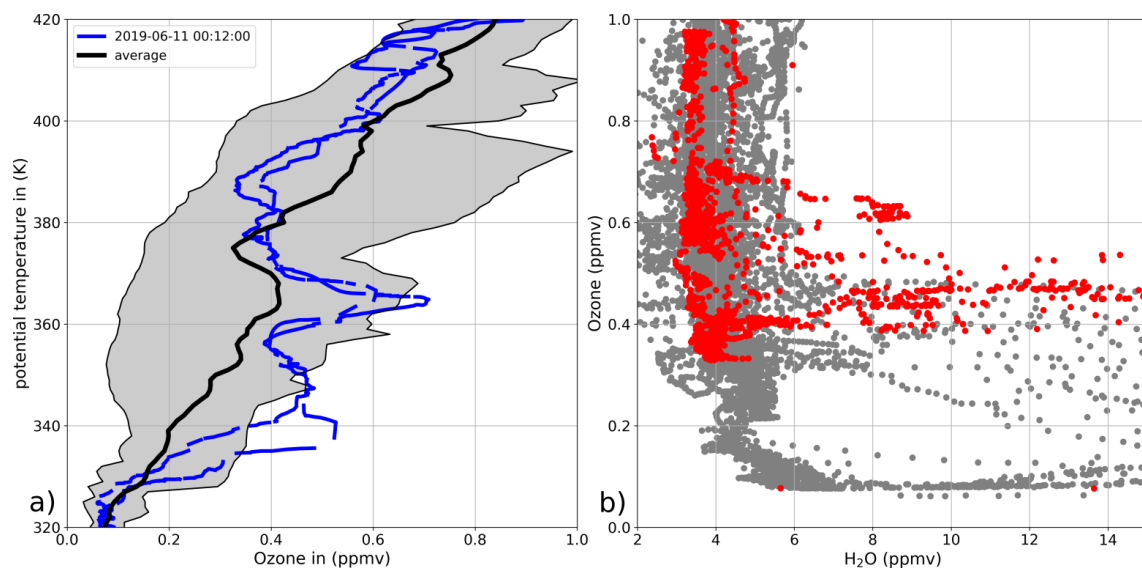


Figure 4.4: Climatology of 8 ozone profiles measured during spring and summer 2018-2020 a) Ozone profiles within the UTLS altitude range from 2018 to 2020 launched in the mid-latitudes in potential temperature coordinates. The shaded area marks the measured range of ozone mixing ratios. The blue line shows ascent and descent data from the from Case 1 b) Tracer-tracer correlation of water vapor and ozone mixing ratios within the UTLS altitude range for the data obtained from 2018 to 2020 in the mid-latitudes. The red dots show the data from the ascent and descent from Case 1

with CLaMS using two different ECMWF reanalysis sets as input, shows an enhancement of ozone between 100 hPa and 200 hPa (See Appendix C). This indicates the horizontal transport of ozone-rich stratospheric air, as the CLaMS model does not account for overshooting events. Figure 4.5 presents the ERA5 reanalysis at the time and approximate altitude of the observed ozone peak. A narrow ozone-rich filament extends eastward from air masses with stratospheric origin towards the measurement location. Hence, there is strong evidence that the ozone-rich stratospheric filament was transported horizontally to the location where water vapor was injected by overshooting convection into the lowermost stratosphere. The location and development of the overshooting convection is discussed in Sections 4.2.4 and 4.2.5.

4.2.4 Comparison to the ERA5 reanalysis

ERA5 is used to place the measured data in a wider context and to evaluate the events. While ERA-Interim does not show any local signatures of the measured convection, the

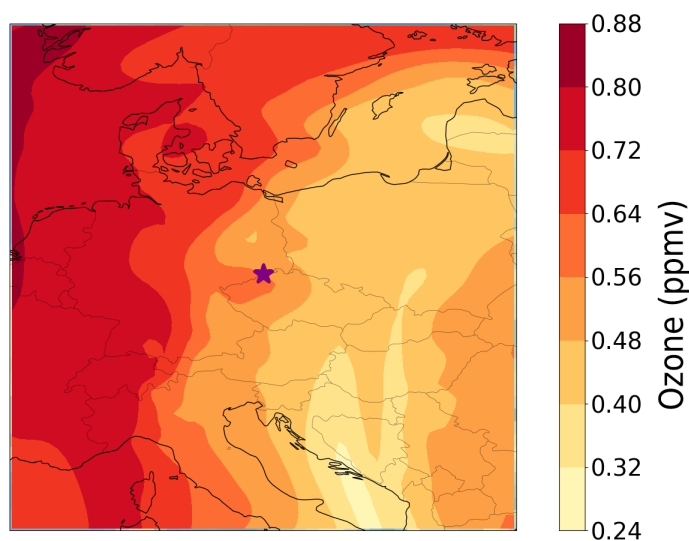


Figure 4.5: Horizontal map of ERA5 ozone mixing ratio at a pressure level of 148 hPa on 11 June 2019 at 01:00 UTC (Case 1). The measurement site is denoted by a purple star.

ERA5 reanalysis reveals the signature of a convective overshooting with multiple parameters. Here CAPE, PV, potential temperature, and the water vapor mixing ratio are considered, starting at midnight on 10 June 2019 until midnight on 14 June 2019. CAPE is the integrated amount of energy that the upward buoyancy force would act on a air parcel if it moves vertically. High CAPE values above 1000 J/kg show an increased probability of strong convective storm development in the case that convection is initiated. Figure 4.6 panels a-c and Fig. 4.7 panels a-c display the distribution of CAPE at three chosen points in time across Central Europe for Cases 1 and 2 respectively. The white line marks the backward and forward trajectories which were initiated at the time and location of the measured water vapor peak for Case 1 (discussed in Section 4.2.5), and the black dot marks the location of the sampled air mass at the given time point according to the calculated trajectories. Very high CAPE values at the coast of Slovenia and Croatia as well, as the east coast of Italy and northern Italy, are evident in all chosen time frames. Figure 4.6 panels a-b show that the air mass measured after the event of Case 1 is located just above a strong maximum in CAPE over north Italy on the morning of 10 June 2019. Throughout the day, the air parcel moves close into regions of enhanced CAPE on multiple occasions along the way to the measurement site, and finally reaching the center of a region with high CAPE close to the measurement site (Fig. 4.6, panel c). Figures 4.7

panels a-c depict the same scenario for Case 2. Here, the air masses crosses a location with high CAPE for the first time at 06:00 UTC on 11 June 2019 over Slovenia. It remains within the region of high CAPE until 13:00 UTC before it crosses the measurement site at midnight. In contrast to the persistent wide-ranged horizontal distribution of elevated CAPE values, a different structural evolution is observed in the PV and dTheta. When considering dTheta at the altitude of the measured air parcel with enhanced water vapor, a strong minimum can be seen, which coincides with the signature of PV for Case 1 and Case 2. For Case 1, on the day before the measured event, no profound signature in the dTheta structure is seen until 09:00 UTC on the morning of 10 June 2019 (Fig. 4.6d). However, at 10:00 UTC (Fig. 4.6e) a spot signature in dTheta is apparent, leading to PV values of up to 25 PVU in the region of high CAPE values over northern Italy. This is more than twice as high as the surrounding PV values. The air mass later sampled is located at the edge of the strong dTheta enhancement with still strong values remaining throughout the next 10 hours. This signature subsequently weakens (Fig. 4.6e) but reappears with increased intensity (Fig. 4.6f) and moves northwards until it dissolves at midnight. The trajectory of the air parcel moves only slightly westward of this structure but remains inside the enhancement of PV over the entire time, although never in the center. A similar course of events can be observed for Case 2, as shown in Fig. 4.7. In comparison to Case 1, the trajectory of the air mass measured in Case 2 approaches further from the south. In the early morning hours of 11 June 2019, no significant structure or signal can be seen in the area of interest (Fig. 4.7d). At 10:00 UTC a dipole structure in dTheta appears leading to PV values of up to 30 PVU (Fig. 4.7e). Similar to Case 1, the signal does not develop gradually nor is it transported horizontally into the considered area, instead emerging on a very short timescale. The anomaly appears over Austria, northern Italy and over the Czech Republic and therefore has 3 central points. The enhancement over the Czech Republic dissolves in the following hour while the other two increase in strength over the next few hours. However, all three centers dissolve until midnight when the air parcel reaches the measurement site. In Case 2, the air parcel is also constantly in the vicinity of at least one of the peaks in dTheta but never enters areas of the extraor-

dinary high values. This signature in $d\Theta$ can be explained with the displacement of the isentropes upward by strong updraft winds and local diabatic heating, which cause an increase in the gradient of potential temperature, as has been shown by Qu et al. (2020). In both cases considered here, the map of the $d\Theta$ is homogeneous before convection appears until 09:00 UTC (Fig. 4.6 panels g-i). However, only 1 hour later, a spot signal with values of up to -2.7 K hPa^{-1} appears, which is more than 3 times higher than the surrounding values. In both cases, the peak in $d\Theta$ moves along the PV enhancement and also dissolves at the same time. Furthermore, the specific humidity in ERA5 was analyzed. Figure 4.6 panels g-i show the specific humidity of ERA5 for Case 1. Figure 4.6g shows the hour before the first appearance of the signature of the convective storm for Case 1 at 09:00 UTC on 10 June 2019. In total, two peaks can be seen on the map but not close to the path of the air mass. Then, 1 hour later, at 10:00 UTC, a water vapor peak emerges in the vicinity of the air mass (Fig. 4.6h) at the same location as the enhancement in PV and $d\Theta$. For Case 2 a similar picture is seen. While no local enhancements in water vapor mixing ratios can be seen in the considered area at 09:00 UTC, only 1 hour later, at 10:00 UTC, a strong enhancement in water vapor is evident in the vicinity of the considered air mass. This signature of the local enhancement is almost twice as high as the peak seen for Case 1. Similar to Case 1, the enhancement is transported towards the measurement site throughout the day and remains close to the measured air mass.

4.2.5 Origin and evolution of the water vapor enhancement along the CLaMS trajectories

In order to determine the origin and evolution of the measured air masses containing the water vapor enhancement, 100 h backward and 100 h forward trajectories were calculated for both cases, as described in Section 4.1.4. The backward trajectories are not shown before 06:00 UTC on 9 June 2019 as the points do not contain any relevant information related to the measurements. The upper panel of Fig. 4.8 displays the water vapor mixing ratios along the trajectory and the data points measured by MLS within 5 degrees of

4.2. Measurement results and analysis

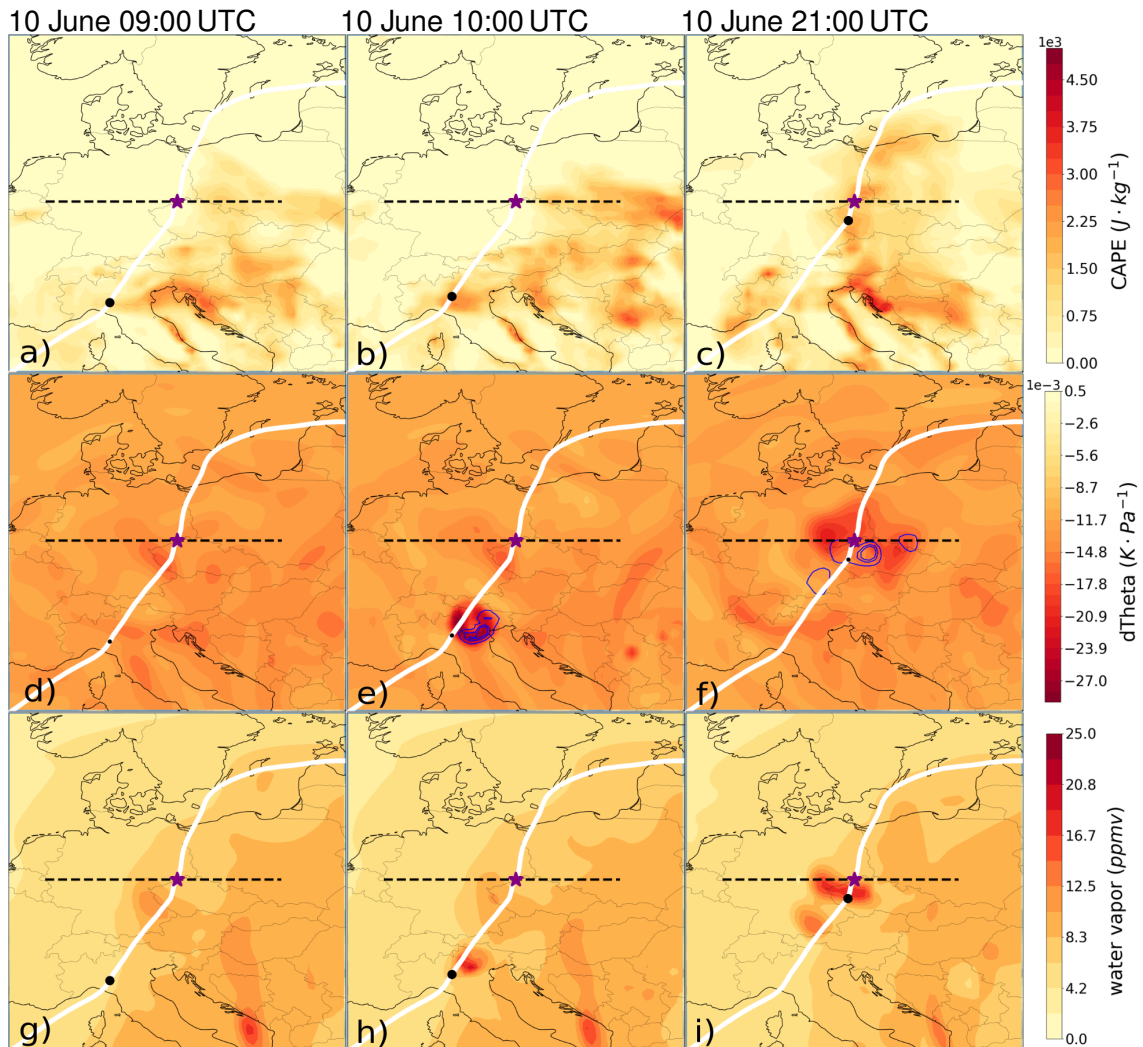


Figure 4.6: CAPE from ERA5 (a-c) vertical gradient of potential temperature ($d\Theta$, d-f) with PV contours at 12, 17, 20, 30 and 35 PVU, and specific humidity (g-i) at three chosen time points for Case 1 (09:0 UTC and 10:00, UTC on 10 June 2019 and 21:00 UTC). $d\Theta$ and specific humidity are displayed at a pressure level of 148 hPa. The horizontal black dashed line denotes the latitude of the measurement site and the purple star denotes the exact measurement location. The white line shows the trajectory of the measured air parcel as described in Section 4.1.4. The black dot on the trajectory line represents the calculated location of the air mass at the given point in time.

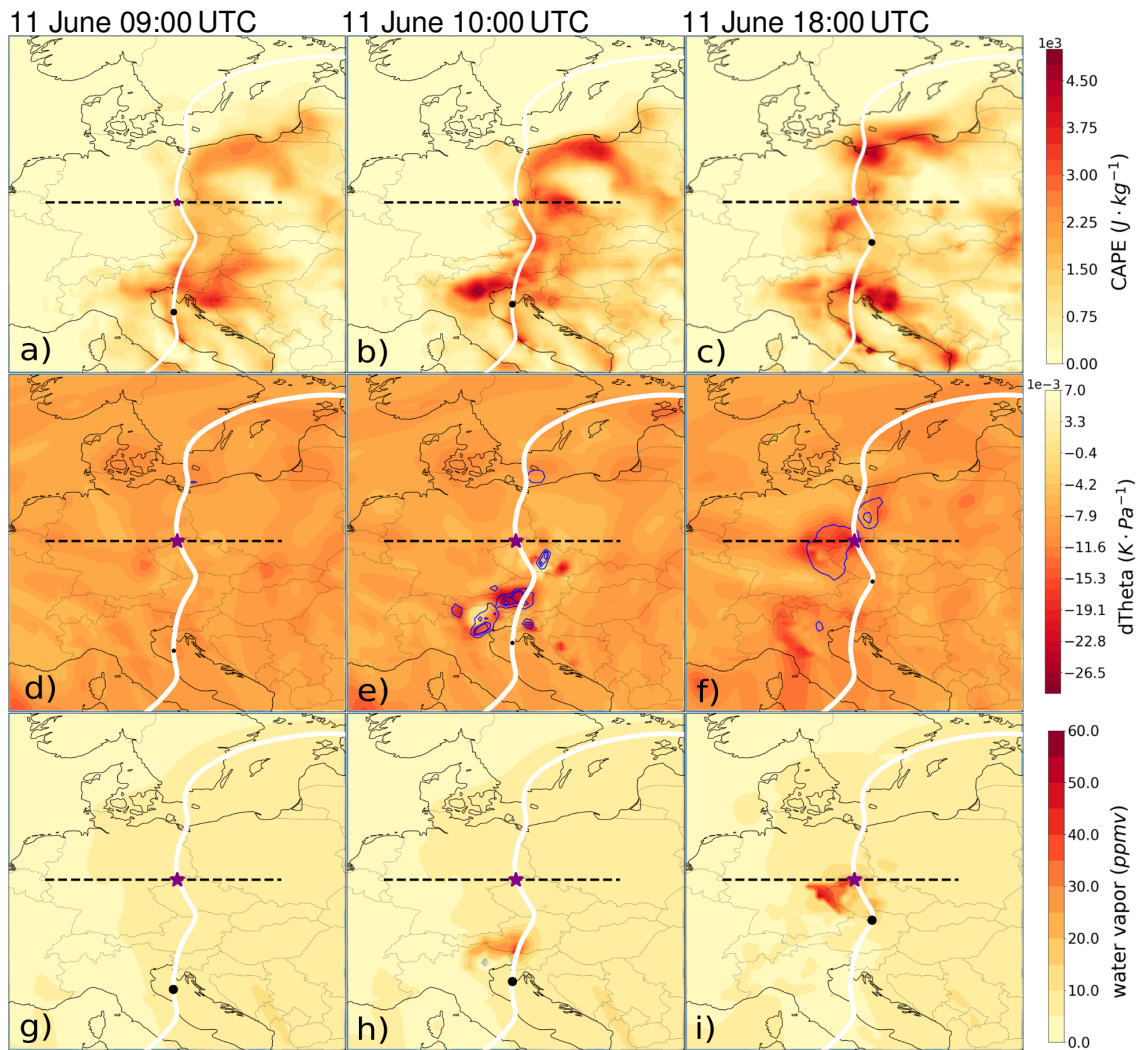


Figure 4.7: The same as in Fig. 4.6 but for Case 2 with three chosen points in time (09:00 UTC, 10:00 UTC and 18:00 UTC on 11 June 2019).

4.2. Measurement results and analysis

latitude and longitude and an hour before or after the trajectory point (star symbols). The ERA5 water vapor mixing ratio shows a sharp increase along the trajectory from values around 7 ppmv to values up to 15 ppmv \approx 10 hours before the balloon measurement took place. The middle panel shows the mixing ratios of ozone and water vapor as well as PV and CAPE values from ERA5 along the trajectory. The trajectory encounters high CAPE values shortly before a steep increase in water vapor and PV appears on 10 June 2019 at around 10:00 UTC. The peak in CAPE is followed by a peak in PV almost doubling the preceding values of around 8 PVU. This peak is in good agreement with an increase in water vapor mixing ratios by 10 ppmv, which remains at the level between 12.3 ppmv and 17.5 ppmv throughout the following 4 days of the trajectory (in contrast to the PV enhancement which decreases shortly before the balloon observations to a background value of 8 PVU). With a water vapor mixing ratio of 10 ppmv measured by the CFH at the peak, the values obtained with the balloon payload are lower than the ERA5 values. The ozone mixing ratios do not show an impact by the convective event but steadily decrease throughout the trajectory. The lower panel of Fig. 4.8 shows MLS water vapor, ozone, and CO mean mixing ratios for the nearest MLS point for each time step within 300 km along the trajectory. Only seven measurement points were found to match the criteria. Although multiple MLS data points were available, a clear increase in water vapor cannot be seen in the available data. Overall, the values measured by MLS are much lower compared to the ERA5 water vapor values, which range from 2 ppmv to 6 ppmv along the calculated trajectory, while the ERA5 values vary between 5 ppmv and 18 ppmv. CO and water vapor act as a tropospheric tracer, with sources at the surface and background values in the stratosphere (Ricaud et al., 2007), and were considered here as a potential additional tracer for convective overshooting. The nearest values of the individual data sets do not show any increase in relation to the proposed convective event. This emphasizes the small scale of the overshooting event and the local scale of the water vapor enhancement, as MLS only has a very coarse spatial resolution in the LS. While the vertical extent of the water vapor peak is 800 m (600 m for Case 2), the vertical resolution of MLS H₂O measurement is 1.5 km. A similar picture appears for Case 2, as shown in

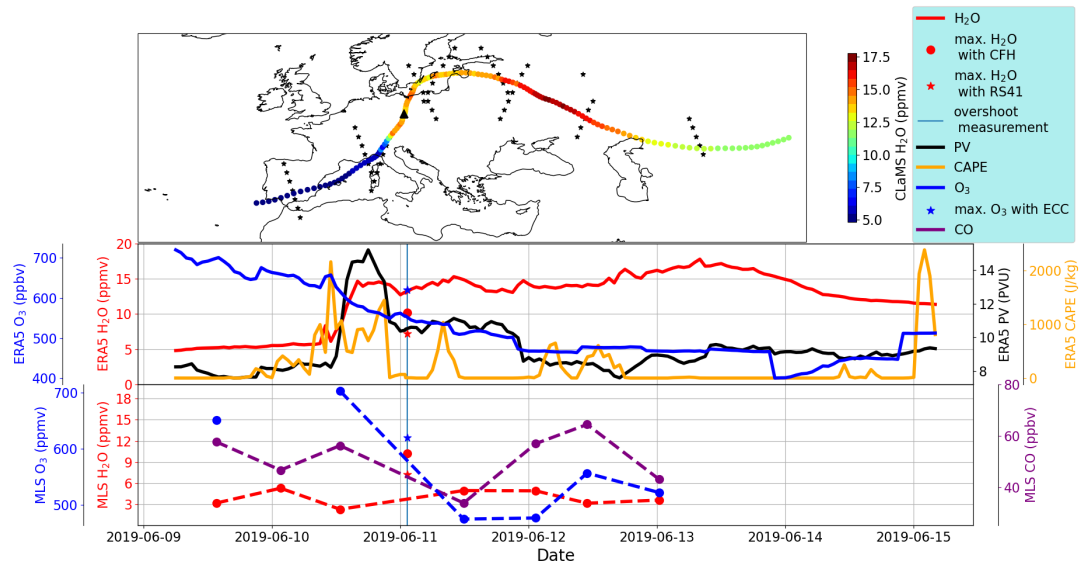


Figure 4.8: Trajectory of the measured air mass for Case 1 with MLS data taken within 5 degrees of latitude and longitude of the trajectory. The upper panel shows the trajectory on a map, with the color-coded water vapor mixing ratios along the trajectory. Additionally, all MLS data points within a longitude and latitude of 5° degrees as well as within 1 hour before and after the individual trajectory points are shown as star symbols. In the second panel, the water vapor from ERA5 along the trajectory is displayed in red, ozone in blue, PV in black and CAPE in orange. The time of the measurement and the observed maximum water vapor mixing ratio from CFH and RS41 within the pressure levels of 145 hPa and 165 hPa are shown at the vertical blue line and with blue and red symbols, respectively. The third panel displays the same time frame, with the nearest MLS measurements of ozone in blue, water vapor in red, and CO in purple, within a radius of 300 km of each trajectory point and 1 hour before or after the trajectory point.

Fig. 4.9. It must be noted that the scales differ in comparison to Fig. 4.8. In Case 2, at midday on 10 June 2019 a series of peaks in CAPE emerge and persist throughout the next 4 days. Shortly before the start of these variations in CAPE, a slight increase in PV is evident and PV values subsequently show enhanced values although not exceeding 9.5 PVU at a background of 7.5 PVU. Water vapor along the trajectory remains constant until midday on 11 June 2019 when it is slightly enhanced from approximately 6 ppmv to 10 ppmv shortly after CAPE and PV reach maximum values ≈ 11 hours before the measurement took place. Similar to Case 1, the water vapor continuously remained at the elevated mixing ratios throughout the end of the trajectory. For Case 2, only four MLS measurement points were found within 300 km of the trajectory. A slight enhancement of

1 ppmv in the water vapor mixing ratio in the MLS data after the overshooting convection and a 30 ppmv increase in CO, which remains enhanced between 55 ppmv and 65 ppmv, together with a slight decrease in ozone mixing ratio by 20 ppbv can be seen. Here it is emphasized that the overshooting event of Case 2 likely has a wider horizontal extent, which makes it more suitable for detection by the MLS instrument. This is supported by the fact that, in contrast to Case 1, both the ascending and descending profiles show enhancements of tropospheric air in the lower stratosphere. The trajectories for the two cases show an increase in the water vapor before the air parcel arrived at the measurement site. The increase in water vapor is accompanied by an increase in PV and high CAPE values. While in Case 1 the steadily decreasing ozone values along the trajectory seem to be unrelated to the changes in the other trace gases, in Case 2, an increase in ozone mixing ratios by 150 ppbv occurs at the same time as the increase in the PV values. In contrast to Case 1, where the peak in PV initially decreases shortly before reaching the measurement site and returns to background values 1 day later, in Case 2 the PV values keep increasing but never reach the high values of Case 1. In both cases, the water vapor mixing ratios remain enhanced after the overshooting convection in the model and shortly before reaching the measurement site. However, Case 2 shows lower values at around 10 ppmv in comparison to 15 ppmv for Case 1. With these values, the ERA5 water vapor value is greater than the measured value in Case 1 but is slightly below the values measured in Case 2.

4.2.6 Overshooting events in satellite data

The satellite measurements of Brightness Temperature (BT) from geostationary Meteosat-10 rapid scan data support the above-indicated tropospheric origin of the measured water vapor enhancement in the lower stratosphere. Figures 4.10a-d show Meteosat-10 BT data using the Infrared (IR) 10.8 μm channel for two chosen times in Case 1. Figure 4.10a shows the data at 05:29 UTC on 10 June 2019. A cloud structure reaching a BT as low as 205 K surrounds the air mass along the trajectory at this time. For Case 1, a CPT of 208 K was measured and confirmed by the surrounding cloud-top BT between

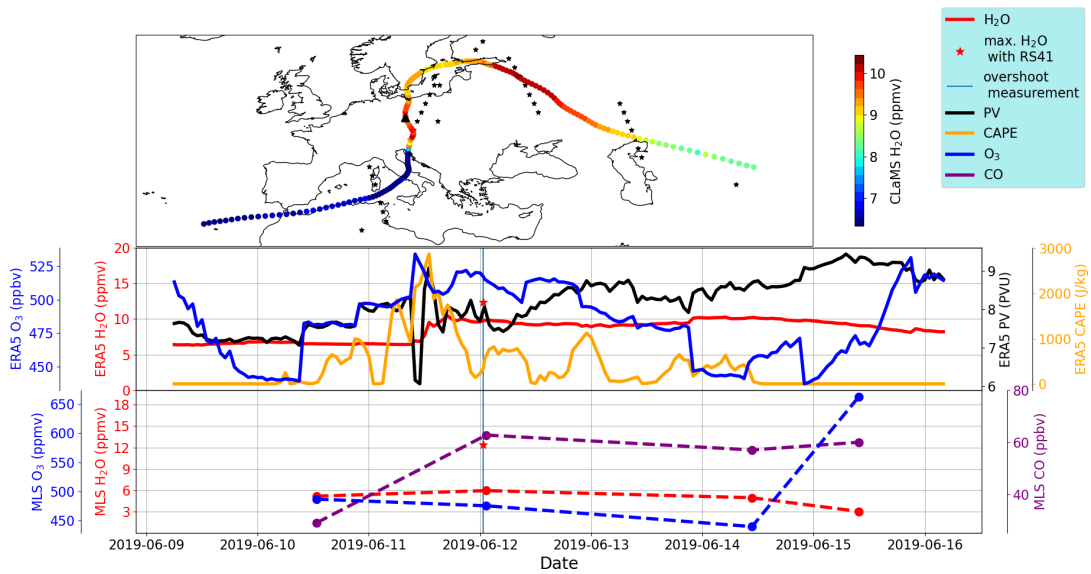


Figure 4.9: Same as in Fig. 4.8 but for Case 2. The time of the measurement is marked with a vertical blue line and the observed maximum water vapor mixing ratio from RS41 within the pressure levels of 139 hPa and 155 hPa, is shown with red star in each panel.

210 K and 216 K. It is, therefore, most likely that areas with a BT below 205 K resemble areas of overshooting tops. These areas are circled in pink in Fig. 4.10. In addition to the trajectories discussed in Section 4.2.5, further trajectories were calculated starting at the same location but, at lower pressure levels, as both balloon profiles not only exhibited a main peak at a pressure level of 149 or 144 hPa but also covered an underlying water vapor enhancement at 165 or 155 hPa respectively, for Cases 1 and 2 (Fig. 4.2 and 4.3). Trajectories initialized at 149, 155 and 165 hPa and at 144, 153 and 155 hPa, respectively, for Case 1 and Case 2 were calculated and added to the satellite image. The air mass on the trajectory starting at 149 hPa is located closest (only 50 km northeast) to the coldest and therefore, highest point of the convective cloud, as can be seen in detail in Fig. 4.10a. Considering the slight uncertainties in the trajectory calculation and in the meteorological fields, this point in time is most likely responsible for the water vapor enhancement detected later. However, the satellite images display the coinciding of the air mass and the convective event 4 hours earlier compared to ERA5 and, therefore, further southwest. Later in the day, the air mass location coincides with another overshooting cloud at around 21:09 UTC (see Fig. 4.10b). Multiple areas exceed the tropopause height in the convective clouds but none of the air masses on the trajectories seem to be very

4.2. Measurement results and analysis

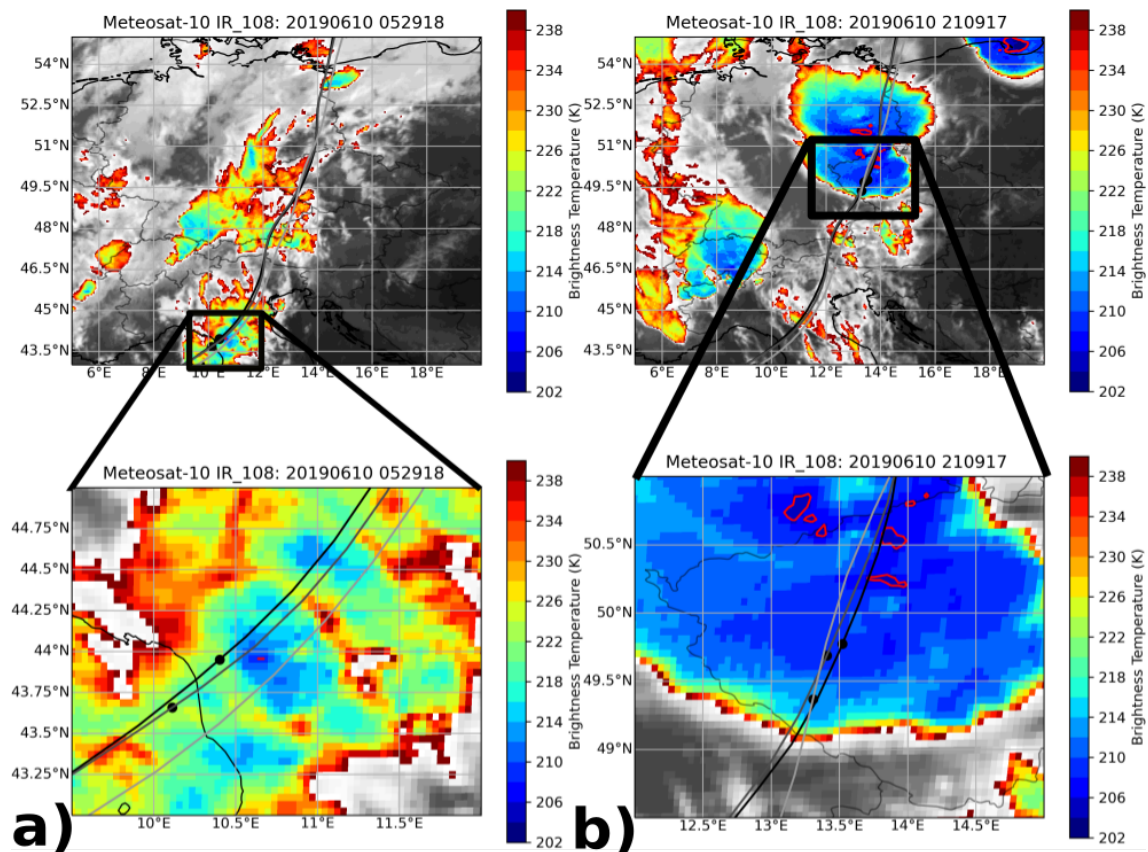


Figure 4.10: Brightness temperatures from geostationary Meteosat-10 satellite using the IR 10.8 μm channel along trajectories for Case 1 during two different times (panel a at 05:59 UTC and panel b at 21:09 UTC on 10 June 2019). Air mass trajectories initiated at different pressure levels (149 hPa, 155 hPa, and 165 hPa) are shown with gray to black lines. Air masses with BT < 205 K are depicted with pink contours.

close to these areas. The trajectories for Case 2 pass by near to the convective events as well; however these are at a greater distance from the overshooting tops (Fig. 4.11a and b). For Case 2, Fig. 4.3b shows a temperature of 214 K at the tropopause height. Trajectories initialized at pressure levels of 145 hPa, 150 hPa, and 155 hPa can be seen in Fig. 4.11 and encounter the cloud-top height with temperatures 6 K below the tropopause temperature. Similar to Case 1, in Case 2, an additional convective storm develops over eastern Germany with overshooting tops. However, the air masses along the trajectories do not encounter this convective cloud (see panel Fig. 4.11a and b). Thus, it is very likely that the observed water vapor enhancement resulted from the overshooting event that occurred over Austria on 11 June 2019 at around 14:24 UTC or 15:49 UTC.

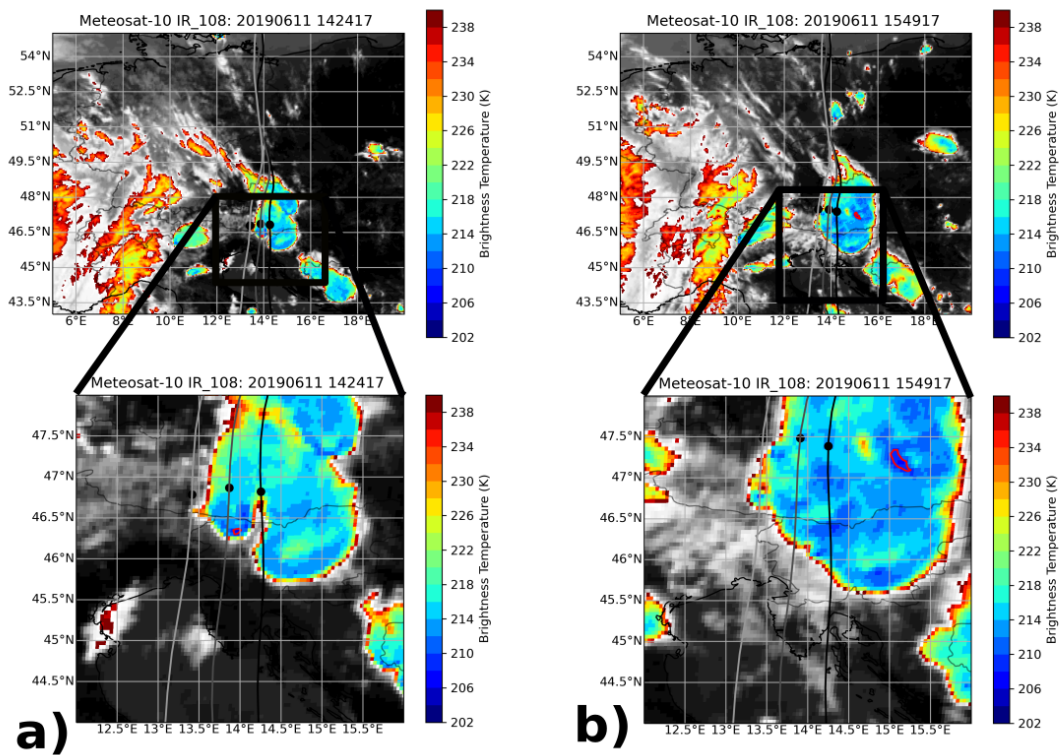


Figure 4.11: Same as Fig. 4.10 but for Case 2. Air mass trajectories initiated at different pressure levels (144 hPa, 153 hPa and 155 hPa) are shown with gray to black lines. Air masses with BT < 209 K are denoted with pink contours. Panel a shows the satellite image at 14:24 UTC, and panels b at 15:49 UTC on 11 June 2019

4.3 Discussion

The measurements presented here show a strong enhancement in water vapor above the tropopause on two consecutive days, i.e., 10 and 11 June 2019. Both cases originate from gravity waves breaking behind the overshooting top leading to in-mixing of tropospheric air into the lower stratosphere several hours before the balloon launch. The water vapor mixing ratio enhancement measured in Case 1 is located 40 K above the thermal tropopause when using potential temperature as a vertical coordinate. This is comparable to a study by Smith et al. (2017) where water vapor mixing ratio enhancements were measured during multiple airborne missions above the North American continent. Smith et al. (2017) use 370 K as a typical tropopause altitude and discuss water vapor enhancements at a level between 400 and 410 K with values up to 6 ppmv above the background values. Similarly, the water vapor values measured in Case 2 are of the same order of magnitude. The maximum of the peak is approximately 40 K above the tropopause potential temperature and reaches 7.5 ppmv above the background value. The same order of magnitude was observed during the Studies of Emissions, Atmospheric Composition, Clouds and Climate Coupling by Regional Surveys (SEAC4RS) aircraft measurement campaign with elevated water vapor mixing ratios of up to 10.6 ppmv in the lowermost stratosphere at ≈ 100 hPa (Robrecht et al., 2019). The local injection of water vapor was detected within a larger-scale peak in ozone for Case 1. This peak results from a horizontal transport of stratospheric air masses with a strong stratospheric signature from west to east. An edge of a filament from a front with high ozone values is stretched over the measurement location. A map of ERA5 ozone at 145 hPa, as given in Fig. 4.5, shows that the balloon measurement was at the edge of a front with higher ozone mixing ratios. This explains the lower ozone values at the same pressure or potential temperature level in the descending profile which was located further north. This is also supported by the sparse data from MLS, which show higher ozone mixing ratio values westward of the measurement site and lower values of about 200 ppbv east of the measurement site (see Fig. 4.8). The ERA5 ozone values along the calculated trajectory of the measured air mass further support this assessment. The moistening of the ozone-rich air mass lead

to an unusual feature in the tracer-tracer correlation, as shown in Fig. 4.4b. Case 1 not only shows a strong enhancement of water vapor mixing ratios in the ascending profile of the balloon-borne measurement, but further expected indications of a tropospheric air injection were also recorded. A sharp decrease in ozone mixing ratios occurs at the same potential temperature level as the rise in water vapor. The drop in temperature is equally sharp and aligned with the change in water vapor and ozone, albeit less prominent. The elevated water vapor, decrease in ozone mixing ratios, and lower temperatures all indicate the tropospheric origin of the measured air mass between the potential temperature levels of 365 K and 375 K. The air mass is clearly different from the air masses above and below to a degree that the profile of the water vapor peak appears to be square shaped (see Fig. 4.2b). The fresh in-mixing and the tropospheric origin of the air masses is also underlined by the small spatial extent of the enhancement. This is derived from the following two observations: first, the balloon measurement does not show any enhancement of water vapor in the descending profile, and second, no clear trace of the event can be found in the MLS measurements due to the low vertical and horizontal (cross-track) resolution at the limb tangent point of 1.5 km and 3 km, respectively. The tropospheric source of the water vapor injection for Case 1 is supported by satellite BT measurements of overshooting tops and by ERA5 displaying a local disturbance in PV and dTheta along the trajectory of the discussed air mass. The dTheta anomaly is in good agreement with the local enhanced water vapor mixing ratio in ERA5 (Fig. 4.6d - f). The BT satellite data suggest that this coinciding of the measured air mass and the convective overshooting event occurs ≈ 4 h earlier at 05:29:18 UTC further southwest, but otherwise both the re-analysis and the observational data show a convective storm moving northwards, with high-reaching cloud tops and BTs reaching as low as 205 K. Until this convective event dissolves after 22:00 UTC, the measured air parcel remains close to its center. The air mass along the trajectory starting at 149 hPa encounters a second, stronger, and more spatially distributed convective event over the northeast of Munich (southeastern Germany), in the evening at 18:19 UTC and 19:39 UTC where it also passes close to a cloud-top height reaching 202 K BT (see Fig. 4.12). The air masses continue to remain in this

4.3. Discussion

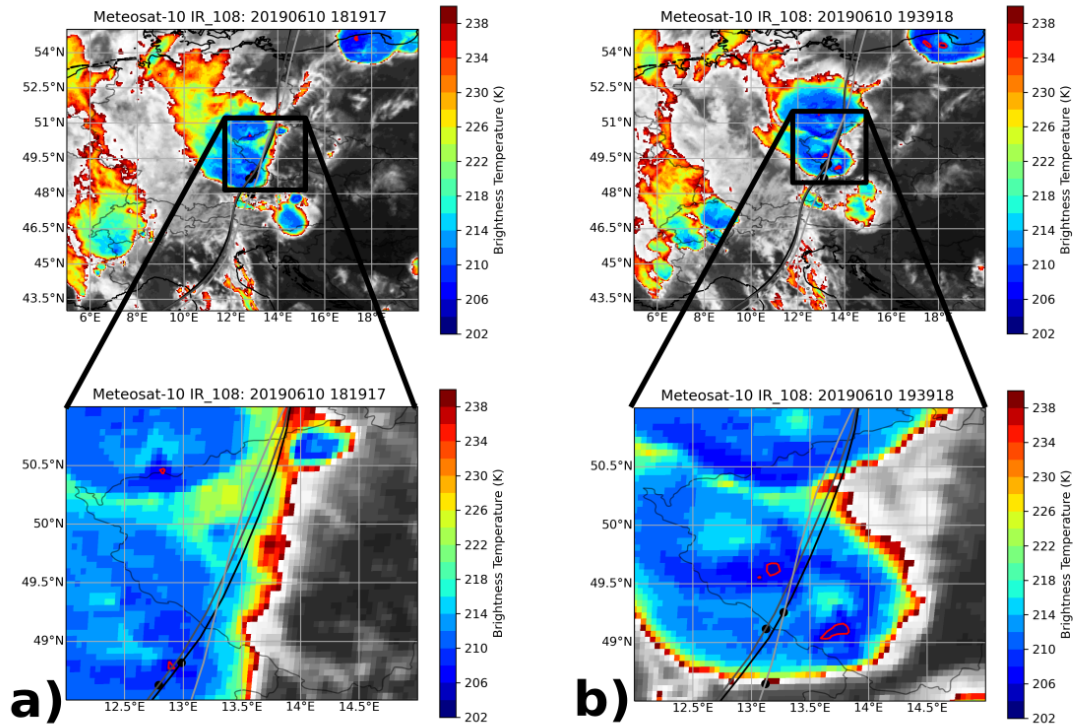


Figure 4.12: Same as Fig. 4.10 but for a different point in time. Air mass trajectories initiated at different pressure levels (144 hPa, 153 hPa and 155 hPa) are shown with gray to black lines. Air masses with BT < 209 K are marked with pink contours. Panels (a) and (c) show the satellite image at 18:19 UTC and panels (b) and (d) at 19:39 UTC on 10 June 2019.

growing convective cloud, which eventually covers the entirety of eastern Germany, until the measurement site is reached. As described in Smith et al. (2017), Dauhut et al. (2018), and Qu et al. (2020), the in-mixing of tropospheric air masses is caused by gravity waves breaking closely behind an overshooting top into the surrounding stratospheric air, which has a lower water vapor mixing ratio and a higher potential temperature. The hydro-meteors from the injection sublimate and are mixed into the stratospheric air mass on very small timescales under these strongly subsaturated conditions. It is, therefore, consistent that the additional COBALD measurement (not shown) did not detect any cloud particles in the measured profile. Additionally, the sublimating hydrometeors cool the air mass. It is very likely that the air mass descended slightly due to the decreased potential temperature after the mixing of tropospheric and stratospheric air and, therefore, reached neutral buoyancy at a lower level than was later found in the balloon profiles. This pro-

cess would not be evident in the calculated trajectories and, thus, slightly increases the inaccuracy of the presented trajectories. However, the descent of the air mass due to the adjustment of potential temperature is expected to be rather low due to the very humid conditions of the LS mixed-in tropospheric air mass. Furthermore, the existence of sublimated hydrometeors in the entrained air masses result in a relatively low amount of air that is ultimately irreversibly mixed within the LS. Case 2 shows a similar signature but differs in several aspects. First, the balloon profile measurements in Fig. 4.3a and b show that the water vapor enhancement is stronger and is located at a lower pressure level (although the level of potential temperature remains almost the same). In contrast to Case 1, only radiosonde measurements are available for Case 2, and thus, only water vapor data measured by the radiosondes can be compared for both cases. While in Case 1 the peak value is 7.0 ppmv, in Case 2 the maximum peak value reaches up to 12.1 ppmv. In addition, balloon measurements for Case 2 potentially indicate not only a stronger but also a spatially larger event, as the descending profile reveals a peak in water vapor that still reaches more than 7.5 ppmv but with a wider vertical spread. This indication is supported by the MLS measurements. For Case 2, a slight increase in MLS water vapor mixing ratios (≈ 1 ppmv) is visible after the balloon observation compared to the MLS data point that was taken before the suggested convective event (see Fig. 4.9). The development of the water vapor peak does not form a square shape when using potential temperature as a vertical coordinate, and instead forms a sharp tip after a steep water vapor increase. Slightly below this tip, a drop in temperature can be seen (Fig. 4.3b), with a similar decrease (by about 2 K) to that of Case 1. A further difference between the cases is the tropopause. While Case 1 shows a very sharp tropopause, Case 2 has a rather flat tropopause with an inversion layer at 125 hPa. In the temperature profile obtained 2 h prior to the profile with enhanced water vapor (displayed in Fig. 4.3a and b), a second tropopause is detected. Throughout the day of Case 2 (launched at 13:11 UTC and 22:00 UTC on 11 June 2019) two profiles with double tropopause were measured, which indicates a less stable atmospheric profile and possibly supports the findings of Solomon et al. (2016), who found that the overshooting convection is more likely in cases

of a present double tropopause. ERA5 also shows a difference between the two cases. Case 2 shows a higher and wider spread of CAPE values before the overshooting event throughout the day when compared to Case 1. The PV anomaly discussed in Section 4.2.4 shows a cluster of individual anomalies around the calculated trajectory instead of a single event, as in Case 1. According to the satellite data the air mass measured in Case 2 encounters a convective event once in the afternoon over Austria (see Section 4.2.6) but does not encounter a second event later, which is in contrast to Case 1. While ERA5 shows a likely overshooting event for Case 1 4 h before, and slightly northwest of the event observed by satellites, the convective event in ERA5 for Case 2 is 4 h later than the satellite observation. Overall, the ERA5 data indicates that the measured air parcels of both cases were moistened by the occurrence of an overshooting convective storm, which caused a local nonconservative PV anomaly to appear at the level of the measured air parcel. This PV signal was most likely caused by the upward displacement and narrowing of the isentropes in combination with diabatic processes and related small-scale mixing (Qu et al., 2020). The overshooting convection which moistened the measured air parcel in the lower stratosphere occurred in the north of Italy several hours before the convective event arrived at the measurement site as implied by satellite data and ERA5. However, the moistened air parcels took a similar pathway in the lower stratosphere to the convection in the troposphere before both arrived at the measurement site in eastern Germany. It is not clear from the data whether the air parcel was moistened once during the first appearance of the convective storm in the northern part of Italy or if it was moistened multiple times along the trajectory, as indicated by the satellite images over Bavaria to the south of the measurement site. In addition, the question as to when exactly water vapor was injected into the lower stratosphere remains unanswered. However, it is evident that the water vapor was injected into the lower stratosphere by convective overshooting and is not caused by another mechanism, such as, for example, the horizontal transport and the in-mixing of tropical air masses at the subtropical jet.

4.4 Conclusions

Overshooting convective events are known to inject water vapor into the lower stratosphere. However, their quantitative impact on the variability in water vapor mixing ratios in the mid-latitudes requires further investigation. A number of case studies of overshooting tops and their vertical transport of water vapor were performed above the North American continent. However, in-situ measurements over Europe are still sparse. In this study, two cases of water vapor injection into the lower stratosphere over the German-Czech border are presented. The balloon-borne in-situ measurements show water vapor enhancements in excess of the background value of 5 ppmv by 3.65 ppmv for Case 1 and 7.1 ppmv for Case 2. Both cases show clear evidence for overshooting convection and have a comparable scale to overshooting events measured in previous studies over the North American continent. The findings of the in-situ balloon-borne measurements are supported by ERA5 and by satellite data. It has to be emphasized here, that ERA5 includes the overshooting convection and moistening of the LS in both cases, which is in contrast to ERA-Interim reanalysis. The location and timing of the observation was not precisely matched by ERA5 but was, nevertheless, relatively close to the event observed in the satellite data. It is shown that the measured enhancements of water vapor at a pressure level of 149 hPa and 144 hPa, respectively, for Cases 1 and 2 were injected into the lower stratosphere several hours before the measurement took place and were horizontally transported to the measurement site. Stratospheric moistening through overshooting convection over the North American continent has already been reported (Smith et al., 2017). Here, evidence demonstrating that stratospheric moistening also occurs by overshooting convection over Europe is reported. The strength of the measured water vapor enhancement shows that the role of overshooting convection over Europe and in mid-latitudes in general as a contributor to the lower stratospheric water vapor budget might be underestimated due to the sparse in-situ data. As it is expected that the frequency and strength of extreme convective events will increase with advancing global climate change, it is crucial to thoroughly understand and quantify the impact of these events. MLS satellite measurements are not always suitable for detecting these small-

4.4. Conclusions

scale water vapor enhancements, as shown especially in one of the two cases. Thus, studies estimating the relevance of overshooting convection on the extra-tropical water vapor distribution using satellite data might underestimate their effect in general and not only over Europe. Therefore, because of the low resolution of satellite data, in-situ measurements and future satellite missions with very high vertical resolution in the UTLS are therefore required to understand the impact of such small-scale events like overshooting convection.

Chapter 5

Case study of highly enhanced water vapor mixing ratios in the stratosphere originating from forest fires

In this chapter the impact of tropopause penetrating Pyrocumulonimbus Clouds (PyroCb)s on the stratospheric humidity is analyzed using MLS and ERA5 data. For the two cases analyzed here, the aerosol loading of the impacted air masses led to a rapid rising of the air mass, which locally changed the chemical composition and dynamics of the stratosphere.

In 2017 Canada experienced 5611 forest fires with 3.4 million hectares of land burned. 1.2 million of these were located in British Columbia (Columbia, 2021). Peterson et al. (2018) classify the PyroCb caused by the fires in British Columbia (BC) during August 2017 to be of the same order of magnitude in aerosol loading in the stratosphere as the Kasatochi volcanic eruption in the year 2008. In fact they identify five individual PyroCb updrafts which occurred nearly simultaneously on 12 August 2017. On this day, the first fire broke out at 21:00 UTC and the last at 00:30 UTC and the fires were active overall for

5 h. This event is hereafter referred to as BC2017.

The meteorological situation with dry surface air masses in the beginning of August 2017 caused an intensification of annual wild fires in BC. When the upper-level cyclone with a surface cold front arrived at the west coast of North America, moist and unstable air was transported over the dry and unstable boundary layer leading to a large rising motion in the middle and upper troposphere and to the initiation of PyroCb (Peterson et al., 2018). These conditions apply well to the results shown by Peterson et al. (2017), where it is found that PyroCb "[...] development occurs when a layer of increased moisture content and instability is advected over a dry, deep, and unstable mixed layer [...]". The thickness and height of these multiple PyroCb clouds broke a record, previously hold by Australian forest fires in 2006 (NASA Earth Observatory, 2017). Kirchmeier-Young et al. (2019) investigate the attribution of this event to anthropogenic climate change and find that man-made climate change increases the probability of such events by 2 - 4 times and increased the area affected by such events by a factor of 7 - 11. With proceeding climate change this finding emphasizes the research relevance for this kind of events and its possible future influence on the stratosphere. It can be expected that the extreme wild fires as well as other extreme events will increase in strength and frequency in the future. The lifting of the BC2017 smoke plume was strong enough to reach the stratosphere as described by Khaykin et al. (2018). Peterson et al. (2017) estimate the total aerosol loading transported into the LS to be 0.1 - 0.3 Tg. As the estimated total dry mass of the burned area is about 0.02 - 0.26 Tg, the residual mass is caused by water evaporation and uptake. Cloud-Aerosol Lidar and Infrared Pathfinder Satellite Observations (CALIOP) observation show a 1 km thick aerosol layer between 14 km and 19.8 km altitude in the time frame from 24 August to 26 September, multiple weeks after the event over Southern France with a maximal optical depth value of 0.21 (Khaykin et al., 2018). Kar et al. (2019) analyzed the implications of BC2017 on the stratospheric aerosol loading by comparing the retrieved extinction coefficients averaged over middle and high northern latitudes from January 2007 to December 2017. The BC2017 event caused increased extinction coefficients reaching as high as preceding volcanic eruptions, like "Kasatochi", "Sarychev" and

"Nabro".

From 29 December 2019 to 4 January 2020 Australia experienced intense bush fires in the southern parts of the country. These fires were part of the Black Summer, a term referring to a season of strong bush fires all over the country. In total, an area of 7.4 million hectares covered mainly with forests was burned (Boer et al., 2020). This resulted in roughly 1.0 Tg of cumulative smoke which was finally transported into the stratosphere (Peterson et al., 2021). This event even exceeds the previous record-high smoke mass injection into the LS set by BC2017. Adapted from Peterson et al. (2021), this event will be referred to as Australian New Year Super Outbreak (ANYSO) in the following. The event led to the formation of multiple PyroCb outbreaks, with the two strongest happening on 31 December 2019 and 1 January 2020. The opaque cloud produced by this PyroCb event was observed by the CALIOP satellite based lidar instrument on the same day at altitudes up to 17.6 km (Khaykin et al., 2020). Further PyroCb events also took place on 4 and 7 January 2020, however they did not match the severity of the event a few days before. Hence, in the following only the PyroCb on 1 January 2020 will be investigated.

The effect of the injected aerosols by BC2017 which were transported over the entire hemisphere and entered the Asian Monsoon Anticyclone (AMA) were described by Khaykin et al. (2018); Peterson et al. (2018); Ansmann et al. (2018); Kloss et al. (2019); Yu et al. (2019); Pumphrey et al. (2020); Werner et al. (2020) and Lestrelin et al. (2021). Similarly, Boer et al. (2020); Khaykin et al. (2020); Kablick et al. (2020); Rodriguez et al. (2020); Peterson et al. (2021); Khaykin et al. (2021); Lestrelin et al. (2021) described the impact of the aerosol injection into the southern hemisphere caused by ANYSO. However, with this wild fire plume also water vapor has been injected into the stratosphere.

In this chapter, the focus is on the transport of water vapor into the LS by both events (BC2017, ANYSO) and findings already published in the mentioned studies will not be reported. Enhanced water vapor values caused by forest fires have been previously reported by Pumphrey et al. (2011a). However, none of the studied events shows such extraordinary values above the 100 hPa pressure level like the two cases BC2017 and ANYSO (see below). The plumes produced by these fires led to water vapor mixing ra-

tios in the stratosphere never seen before. Mixing ratios of up to 19 ppmv were captured by MLS satellite observations at the 100 hPa level.

Events like BC2017, ANYSO or volcanic eruptions are not considered in climate projections, however, the remarkable input of aerosol, CO, and water vapor from this events has to be investigated to understand the influence of such singular extreme events on the climate.

5.1 Methods

The MLS and ECMWF-ERA5 data are already described in section 4.1.2 and 4.1.3. In this chapter, data from the Version 4 retrieval algorithm is used. MLS Version 4 data is provided on 36 different pressure levels ranging from 316 hPa to 0.002 hPa. Here we use data at pressure levels of 121, 100, 82, 68, 46, 38, 31, 26 and 12 hPa with a vertical resolution of about 1.5 km in this altitude range. The field of view at the tangent point (measurement location) has a size of 165 km in the horizontal and 3 km in the vertical direction. The improved cloud detection scheme in order to exclude cloudy radiances in MLS V4 has significant impacts on the detection of the BS2017 event because the plume is accompanied by severe smoke and opaque clouds.

5.1.1 Plume identification

In order to identify the measurement points which are affected by the forest fires in the MLS data, the same method as introduced by Pumphrey et al. (2011a) is applied to the MLS data set starting from 1 August 2017 to the 17 October 2017. To detect the BC2017 plume in the LS, observed CO mixing ratios are used. MLS data points which fulfill the following condition are defined to be part of the BC2017 plume:

$$[CO]_x > \overline{[CO]}_{lat} + 4.2 \cdot std([CO]_{lat}) \quad (5.1)$$

The measurement point is considered to be part of the plume if its CO mixing ratio measurements exceed 4.2 times the standard deviation above the average of the respective

latitudinal band. Hereby, only data points measured at latitudes between 35 °N and 80 °N for the BC2017 case and between 10 ° and 70 °S for the ANYSO case are considered. For ANYSO, this method cannot be applied at pressure levels below 38 hPa, due to the shorter lifetime of CO in the higher stratosphere. This causes increasingly lower CO mixing ratios in the plume, with the result that condition 5.1 cannot be applied any more to detect the plume at higher altitudes. In order to still identify the plume at higher altitudes, the same method is used with water vapor as tracer instead of CO:

$$[H_2O]_x > \overline{[H_2O]_{lat}} + 4.2 \cdot std([H_2O]_{lat}). \quad (5.2)$$

5.2 Water vapor signal in the LS

The BC2017 and ANYSO events significantly impacted the mixing ratios of trace species in the stratosphere with each showing so far unobserved water vapor mixing ratio values at pressure levels up to 31 and 12 hPa, respectively. Figure 5.1a shows the timeline of MLS water vapor mixing ratios over the entire northern hemisphere at latitudes above 35 °N throughout the years 2004 to 2020 at 5 different pressure levels. Figure 5.1b shows the same time span of MLS data at latitudes between 0 ° and 70 °S at the same pressure levels. In each panel the data at the individual pressure level and the smoothed water vapor time series with an average of 500 data points within this time period are shown. The imprint of the seasonal water vapor cycle, known as the tape recorder effect, is evident with higher water vapor values during the winter months and dryer conditions during the summer months at the 100 and 68 hPa pressure levels in both hemispheres (Mote et al., 1996). In Fig. 5.1a the most prominent signature of the time line is the accumulation of extraordinary high water vapor values during August 2017, which appears at altitudes up to 38 hPa. These extraordinary values can be attributed to the BC2017 event and break all previous records of stratospheric water vapor with maximum values of 19.0 ppmv at the 100 hPa level on 25 August 2017. This exceeds the background value of 5 ppmv by 3.8 times and is 21 times outside the standard deviation. At the levels of 68 hPa and 38 hPa the maximum water vapor mixing ratio still reaches 17.2 and 11.1 ppmv, respec-

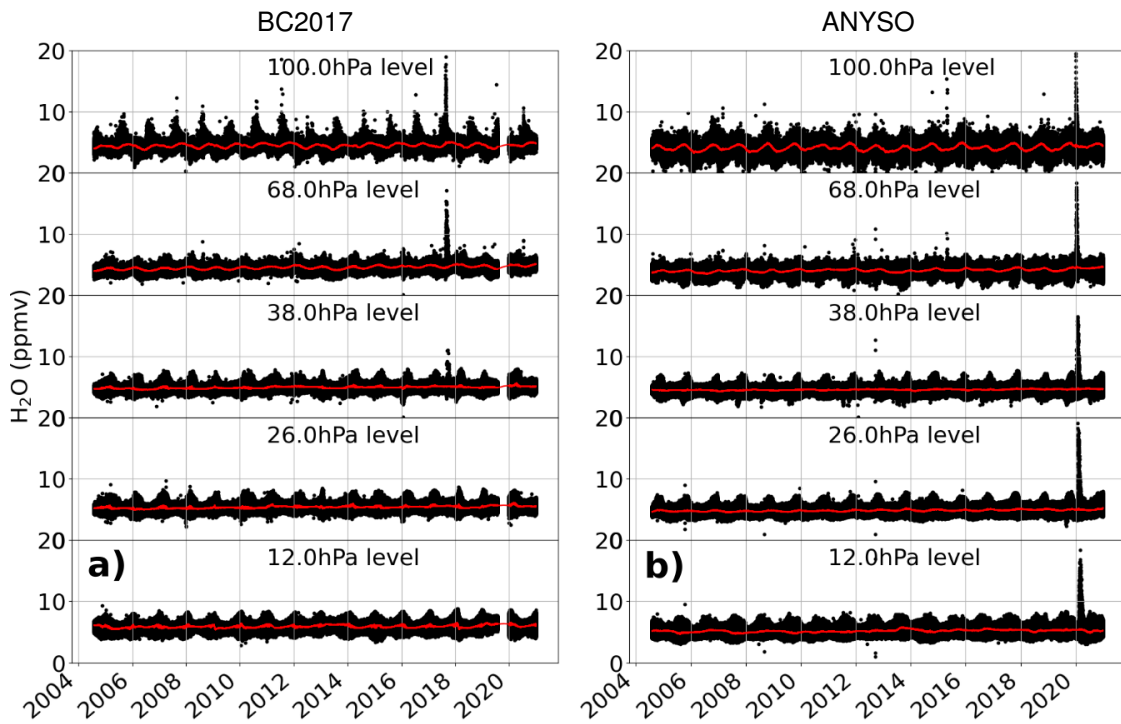


Figure 5.1: A timeline of water vapor mixing ratios measured by the MLS instrument over: a) The northern hemisphere at latitudes between 35 °N and 80 °N at 5 pressure heights b) The southern hemisphere at latitudes between 10 °S and 70 °S at the same pressure level. The red lines represent the smoothed data sets.

tively. In Fig. 5.1b a similar feature with water vapor values reaching up to 19.5 ppmv at the beginning of 2020 is found. In contrast to the BC2017 case (Fig. 5.1a), the striking peak is evident at all shown pressure levels, with values not significantly decreasing with altitude. These peak values can be attributed to the ANYSO event. The maximum water vapor values are 18.4, 16.6, 19.1 and 18.4 ppmv at the pressure levels of 68, 38, 26, and 12 hPa, respectively. The mean, standard deviation, and maximum value for each event and on each pressure level are summarized in Table 5.1. It is evident that in both cases the maximum water vapor values at the 100 hPa level reach values almost 4 times as high as the mean values and ≈ 20 times of the standard deviation. While the maximum water vapor mixing ratios in the BC2017 case decrease with decreasing pressures, the maximum water vapor mixing ratios remain at the same range until 12 hPa for the ANYSO case. It has to be mentioned, that in all figures in this chapter MLS data masked by particles are excluded from the analysis. In the BC2017 case, water vapor values could not be measured within the plume prior to 19 August 2017 due to the dense dust and ice

Table 5.1: Statistical values of stratospheric water vapor distribution for the two wild fire cases at different pressure levels. For the BC2017 event data measured between 1 July and 30 October 2017 and for the ANYSO event between 1 December 2019 and 30 March 2020 are considered. All values are given in ppmv.

BC2017				ANYSO			
level (hPa)	mean	std.	max.	level (hPa)	mean	std.	max.
100	5.1	0.7	19.00	100	4.2	0.7	19.5
68	4.5	0.5	17.2	68	4.5	0.5	18.4
38	5.1	0.3	11.1	38	4.6	0.5	16.6
26	5.5	0.3	6.8	26	4.8	0.7	19.1
12	5.8	0.4	7.2	12	5.2	0.7	18.4

cloud which formed after the forest fires. In order to reliably identify measurement points impacted by the individual wild fire events, the method described in Section 5.1.1 is used. Figure 5.2a shows all MLS measurement points between 8 August and 30 October in the Northern Hemisphere (between 35 °N and 80 °N) at the pressure levels of 100, 68, 46, 38 and 26 hPa as a tracer-tracer plot of water vapor and ozone. Figure 5.2b shows this analogously for the ANYSO case between the 1 December 2019 and 1 March 2020 in the Southern Hemisphere (between 0 °S and 70 °S) at the pressure levels of 100, 68, 38, 26 and 12 hPa, respectively. The measurement points circled in black are identified to originate from the individual forest fire plumes with the CO detection method as used by Pumphrey et al. (2011a), while all other data represent the background values. Fig. 5.3a and b show the identified data without the background values for the BC2017 and ANYSO case, respectively.

It is evident that also within the identified data points, the highest CO mixing ratios correlate with the highest water vapor mixing ratios. This method confirms that almost all above-average water vapor values can be attributed to the forest fires. One exception can be seen in the lowermost panel of Fig. 5.2b, with data at the 12 hPa level in the ANYSO case. For the BC2017 case, the impact of the fires disappears at the pressure levels below 38 hPa (see lowermost panels of Fig. 5.1a and 5.2a). At the pressure level of 26 hPa to little data points are identified to be part of the plume to be further considered. At all other pressure levels, the regression line of the measurement points identified as part of the fire plume shows a negative correlation between water vapor and ozone. Hereby,

5.2. Water vapor signal in the LS

the data at the 46 hPa pressure level stand out with not only the highest anti-correlation between the two species, but also with ozone mixing ratios in the plume (circled in black) below the range of ozone values of the remaining data set at this pressure level. This is a strong indication for the tropospheric origin of the plume. Although ozone is generated when smoke plumes are exposed to sunlight in the upper layer of the plume, the expected ozone mixing ratios are still below the usual range of ozone values at the given pressure level. At the 38 hPa pressure level the ozone mixing ratios are within the usual range of ozone mixing ratios. This suggests a mixing of the plume with surrounding air masses as also the maximum water vapor mixing ratios decrease and a wild fire impact is not traceable anymore at 26 hPa. Hence, the plume ascent is limited to an altitude between the 38 hPa and 26 hPa level.

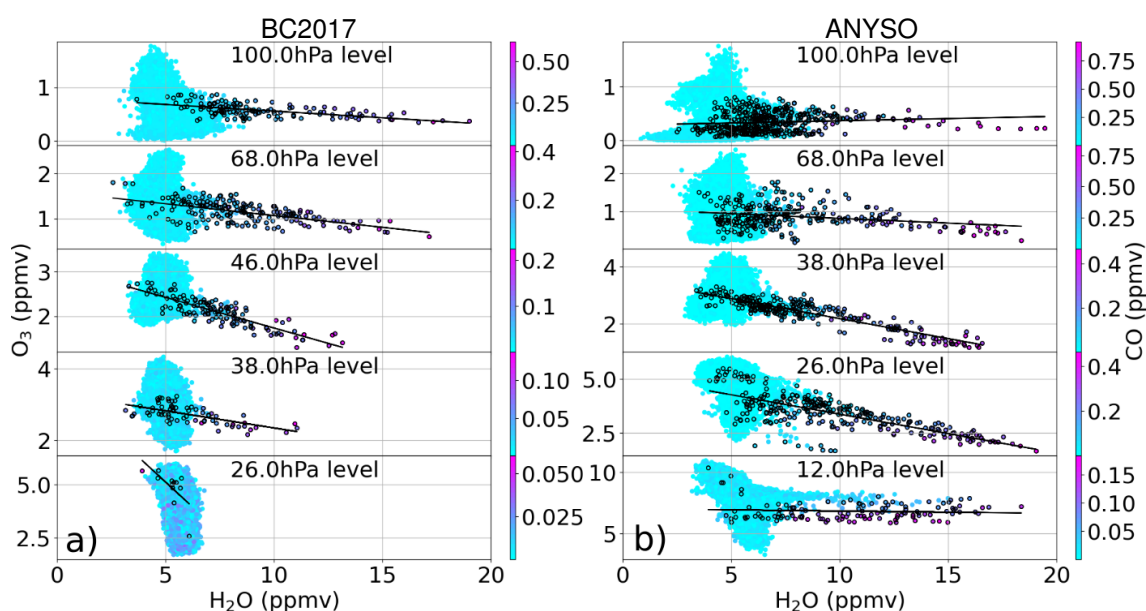


Figure 5.2: Ozone versus water vapor mixing ratios of the MLS measurement points over a) the northern hemisphere between 8 August and 30 October 2017 (BC2017) and b) the southern hemisphere between 1 December 2019 and 1 April 2020 (ANYSO). The points identified to be part of the plumes are circled in black according to Pumphrey et al. (2011a). The regression line for these points is given in black. The color code represents the mixing ratio of CO.

In the ANYSO case two water vapor peaks appear at the 12 hPa pressure level (see lowest panel of Fig. 5.2b). One is found with on average lower ozone mixing ratios (< 7.5 ppmv), the corresponding data points are represented by black circles and are

identified to originate from the wild fire by the used method, and one with on average higher ozone mixing ratios (> 7.5 ppmv) not identified by the method and hence without increased CO mixing ratios. This is displayed in Fig. D.1 in more detail showing the time-line of the ANYSO event at the individual pressure levels with CO as color code in Fig. D.1a and O_3 in Fig. D.1b, presented only for the first half of the year 2020. At the pressure level of 12 hPa one can identify two water vapor enhancements close to each other but separated by several days. The first enhancement has high CO and lower ozone mixing ratios. Vice versa for the second peak. However, in both cases the ozone mixing ratio is within the range of remaining ozone mixing ratios outside the plume, while CO is clearly exceeding the background at each pressure level. As it can be assumed that both enhancements originate from the ANYSO event, the method used by Pumphrey et al. (2011a) can not be applied here. Hence, for pressure levels above 38 hPa the identification method using water vapor mixing ratios was used (see Section 5.1.1). Additionally, it has to be stated that while the identification method is reliably marking all data points impacted by PyroCb, it can additionally include points which also have increased CO but likely originate from other sources.

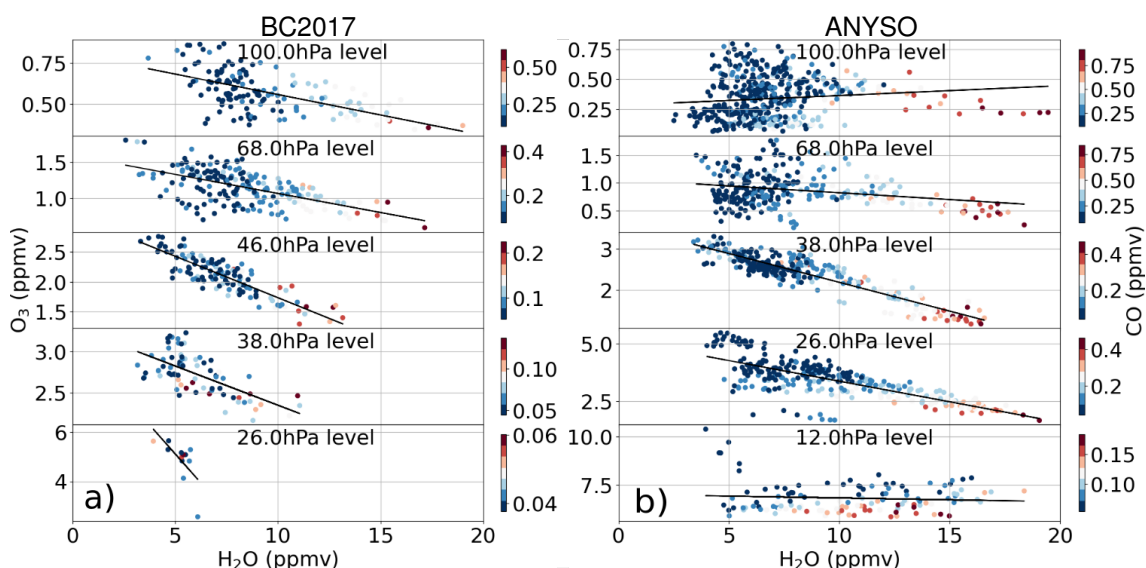


Figure 5.3: The data points identified to be in the plumes according to Pumphrey et al. (2011a), plotted as in Fig. 5.2.

5.3 Horizontal plume distribution

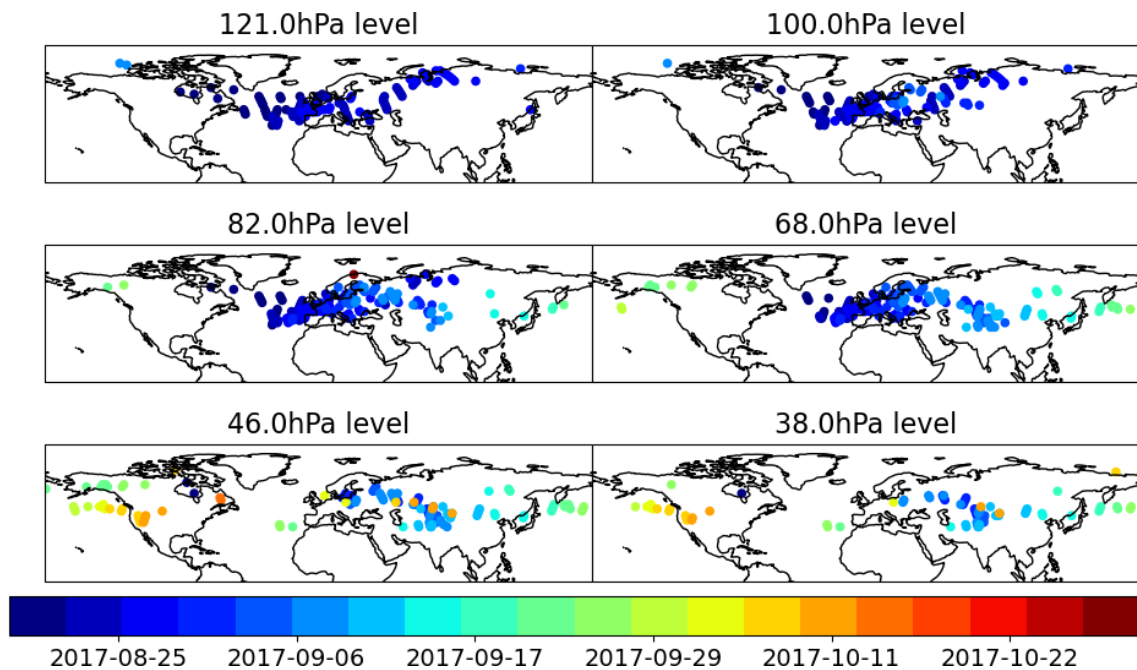


Figure 5.4: Horizontal distribution of the plume at 6 different pressure levels as measured by MLS for BC2017 from 8 August to 30 October 2017. The time of the measurement is color-coded.

Figure 5.4 shows the horizontal distribution of the marked plume produced by BC2017 over time. At the 121 and 100 hPa pressure levels the plume is traceable within the first 5 days after the outbreak of the PyroCb on 12 August 2017 while traveling horizontally eastwards from BC to central Russia. The trace of the forest fires during these days is also evident at the 82 hPa pressure level. At the 68 hPa level the plume appears after 11 days, on 23 August, over the Atlantic ocean and is evident until the 29 September after circling around the hemisphere and reappearing over BC. At the 46 and 38 hPa level the plume first appears after 15 days and remains at that level until it is mixed with the surrounding air masses and is not traceable anymore. Throughout the horizontal transport the plume splits up into two branches. At the 121 and 100 hPa pressure level one branch is first transported southward to Greece and then northward over Russia, remaining at the pressure levels between 121 and 82 hPa. It can be tracked until the first week of September. The second branch, which can be tracked above the 100 hPa pressure level, but not at

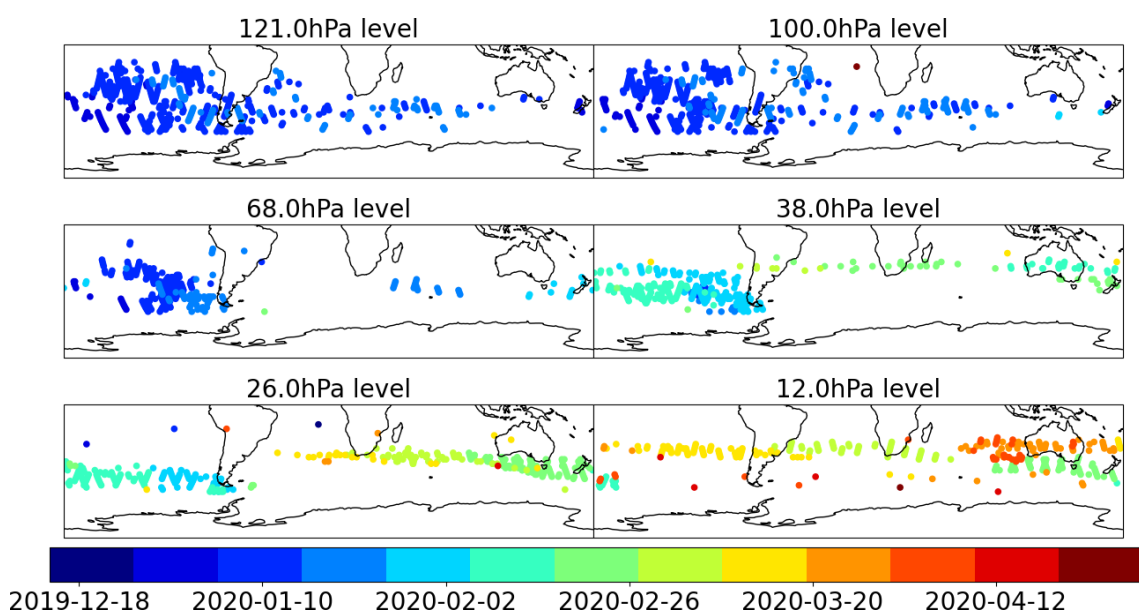


Figure 5.5: Horizontal distribution of the plume at 6 different pressure levels as measured by MLS for ANYSO from 15 December 2019 to 1 May 2020. The time of the measurement is color-coded.

the 121 hPa level, moves northwards first, over-passing Scandinavia and is then directed southward into the AMA region as described by Kloss et al. (2019). The second branch is rapidly lifted reaching a pressure level of 38 hPa with the beginning of September. There it is distributed in a narrow latitudinal band over the entire hemisphere until 24 October. These findings are in accordance with the one of Pumphrey et al. (2020), where a first split of the plume is found at the 100 hPa level 10 days after the outbreak of the fire and a second split at the pressure levels of 68 hPa and 46 hPa. At this level two branches are breaking further into two additional arms, where the first continues to move eastwards and the second reverses and starts to move westward. This event can be seen in the 46 hPa panel of Fig. 5.4. During mid-September (turquoise dots), parts of the plume are evident over China as well as over Iran. Both paths meet again over Canada at the pressure levels of 46 hPa and 38 hPa.

When considering the horizontal distribution of the wild fire plume in the ANYSO case, it is immediately evident that significantly more MLS data points are affected by the wild fire compared to the BC2017 case. While for the BC2017 case MLS has 830 data points affected by the wild fires throughout 68 days on the 6 pressure levels between 121 hPa

and 38 hPa, the ANYSO case has 2202 data points throughout 142 days. Figure 5.5 shows the horizontal distribution of the ANYSO plume with all identified measurement points starting from the 15 December 2019 to the 1 May 2020. In the top two panels displaying the measurements at 121 and 100 hPa, it is evident that within 3 weeks the plume is transported throughout the entire Southern Hemisphere (SH). The plume first appears over New Zealand on 31 December 2019. Similar to the BC2017 case the plume is first transported eastwards. At these two levels the plume consists of two parts: one part is transported eastwards remaining approximately at 40 °S and a second part of the plume appearing at the 121 and 100 hPa level is located several degrees further north at about 25 °S crossing over Brazil and is being diluted thereafter. The first branch of the plume in turn is divided into two parts. While the first subbranch is transported east on the 100 hPa level, circling around the hemisphere until it is diluted over the south of Australia in the end of January, the second part at approximately 120 °W is lifted further to 68 hPa and later up to the 26 hPa level. At these levels it is first transported further east until it reaches the southernmost tip of the American continent, where the transport reverses and is directed westwards. During this transport the plume rises and reaches the 12 hPa pressure level. At all levels between 38 hPa and 12 hPa the plume is circling westwards around the hemisphere. This reversal is caused by a change in wind direction at these upper middle stratospheric pressure levels. Figure D.3 shows exemplarily the stratospheric wind profiles at this location. Depending on the hour of the day the reversal of the wind direction is taking place between 55 hPa and 30 hPa.

5.4 Vertical plume distribution

Figure 5.6a shows the vertical distribution of the water vapor in the plume as, observed with MLS for the BC2017 case. Figure 5.6b shows the same, but as relative change of water vapor mixing ratios of each point relative to the average water vapor mixing ratios at the respective altitude and latitude. The plume caused by the BC2017 event enters the stratosphere during the night of 17 August 2017. However, the air masses containing strongly enhanced water vapor mixing ratios up to 19 ppmv are measured by

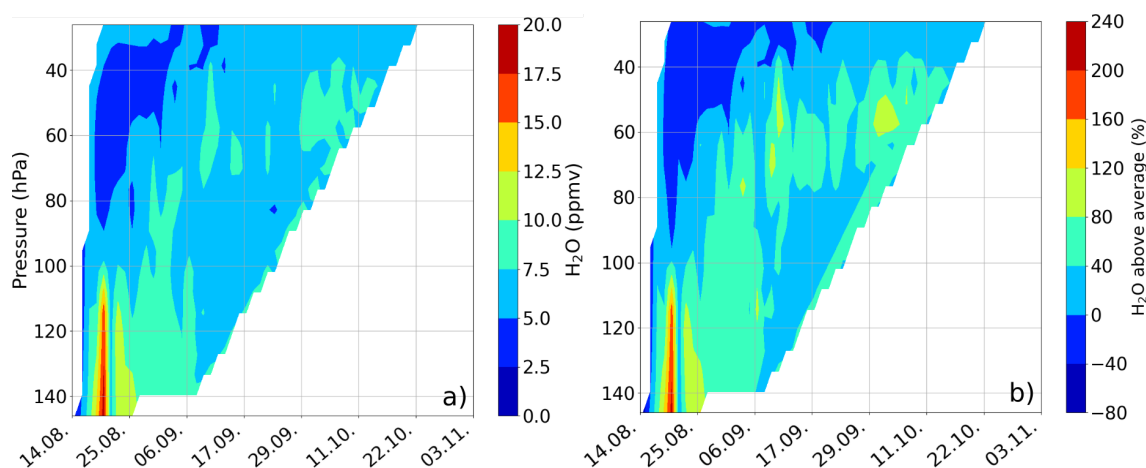


Figure 5.6: Vertical distribution of the BC2017 event. The left panel shows the absolute values of water vapor mixing ratios in the identified plume and the right panel shows the relative increase of water vapor mixing ratios compared to the average at the respective latitude.

MLS on 19 - 21 August 2017. It is evident that the plume of water vapor rapidly rises up to a pressure level of 100 hPa within a few days after the entry into the stratosphere and subsequently further rises to about 50 hPa, where it remains until the end of the considered time period. The relative impact of this event to the water vapor background in the stratosphere (Fig. 5.6b) reaches 240% at pressure levels exceeding 100 hPa on 19 - 21 August when highest water vapor mixing ratios are measured. As the plume further rises and distributes horizontally throughout the Northern Hemisphere (NH), water vapor mixing ratios remain at values of about 10 ppmv which represents an enhancement of about 80% compared to the background value.

Figure 5.7 displays the vertical distribution for the ANYSO case. Similar to the BC2017 case, the plume caused by the Australian wild fires rises vertically up to the 100 hPa level, within a week after the event. However, it further rises to a pressure level of 40 hPa until mid-January when the ascent speed decelerates, but it is still rising to a pressure level of 12 hPa until the plume is not detectable any more in May. The absolute maximum water vapor mixing ratios found within the stratospheric plume are comparable to the BC2017 case. However, the vertical extend and the time span until the water vapor are mixed with the background exceeds the BC2017 case and, thus, more than 2.5 times more air masses were affected by the plume.

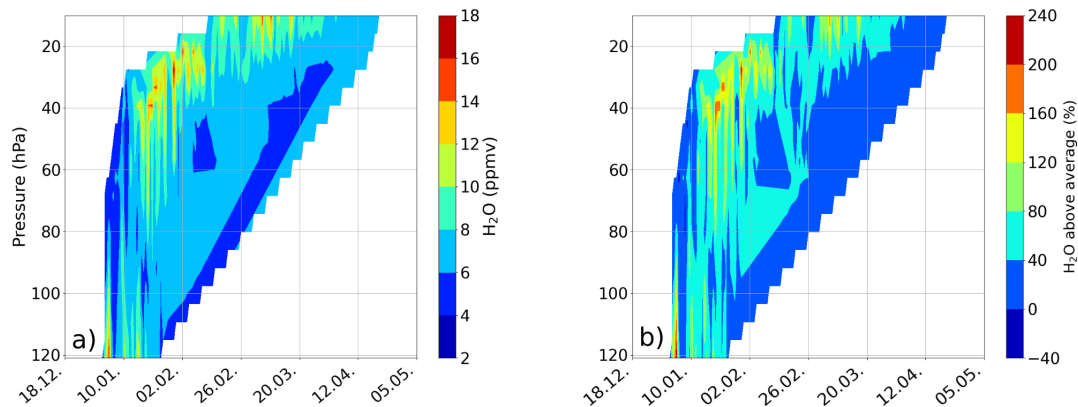


Figure 5.7: Same as Fig. 5.6 but for the ANYSO case.

5.5 PV anomalies in ECMWF ERA5

The injection of a high amount of aerosols into the stratosphere also has an effect on the local dynamics of the air masses impacted by the fire. The black carbon loading produced by the burning process changed the radiative balance which in turn led to changes in vorticity. Similar to the convective case described in Chapter 4, this results in signatures in the PV.

A zonal PV anomaly is observed in the ECMWF ERA5 data coinciding with the identified plume measured by the MLS instrument. Figure 5.8 shows the PV anomaly with contour lines and relative vorticity color-coded for the BC2017 case similar to Fig. 4.6 and 4.7 in Chapter 4. The blue lines mark a negative PV enhancement of -8 and -5 PVU in comparison to the zonal average. The anomaly in PV is appearing at the time and location of the fire plume entry into the stratosphere, on 17 August 2017, and it is consistently moving with the plume (see Fig. 5.4). The air masses influenced by the pyro-convection are associated with uncommonly low PV values at each pressure level. In contrast to the $d\Theta$ and PV anomaly correlation found in the overshooting convection case (see Chapter 4.2.4), no relevant change of the $d\Theta$ PV term is evident within the fire plumes (see Fig. D.4). The change in PV is caused by an anomaly in the relative vorticity. As can be seen in Fig. 5.8, a negative anomaly in relative vorticity coincides with the anomaly in PV. The air masses affected by the forest fire are self-organized as anti-cyclonic vortices initiated by the heating of the plume due to black carbon loading (Khaykin et al.,

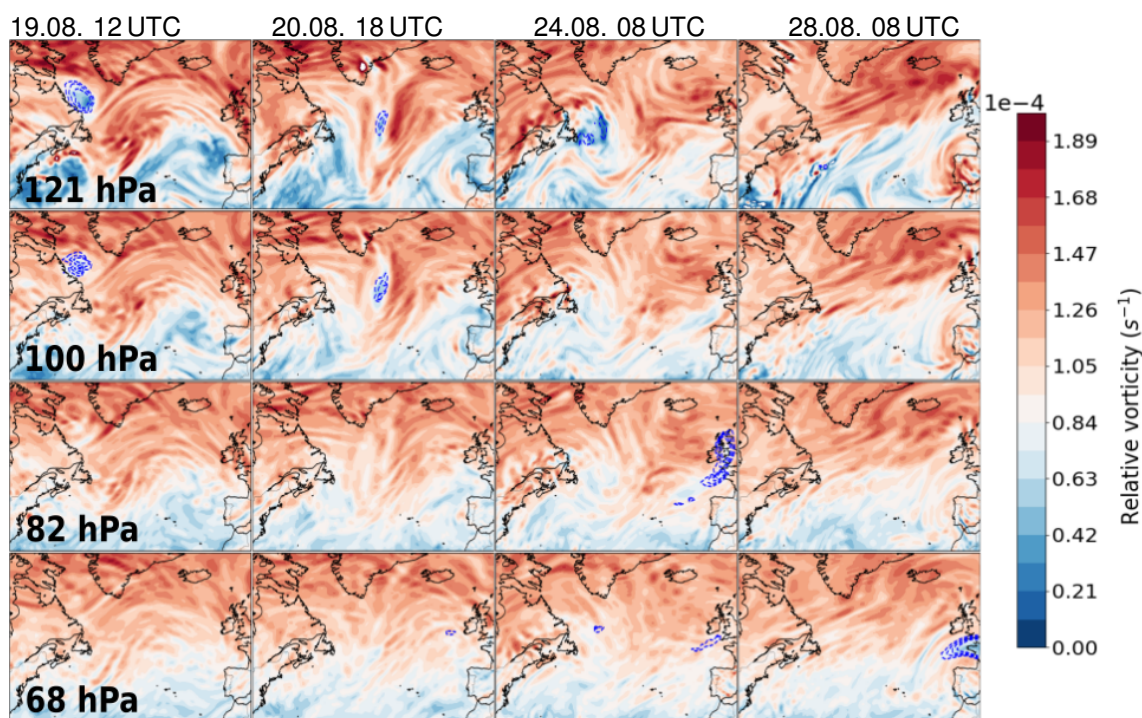


Figure 5.8: ERA5 PV anomaly shown with contour lines at -8 to -5 PVU and relative vorticity color-coded at chosen times between the 16 August 2017 and 29 August 2017 and at chosen pressure levels of 121, 100, 82 and 68 hPa for the BC2017 case.

2020; Kablick et al., 2020; Allen et al., 2020; Lestrelin et al., 2021). This vortex formation constrains the plume air and prevents dilution with the ambient air. The plume further heats up due to black carbon loading and continuous solar irradiation. Hence, the plume is self-sustaining causing the persistence of the plume.

After the first evidence of the PV anomaly at the 121 hPa level on 17 August, it rises to the 100 hPa level on 22 August and finally appears at the 68 hPa on 24 August. At this point the plume reduces its westward velocity and remains for several days over Spain and England, afterwards it splits into three parts. The anomaly moves as described in Section 5.3 with the plume. During its transport the vortex splits up two times in total as can be exemplarily seen in Fig. 5.9 at the 68 hPa level, most likely caused by the prevailing horizontal wind shear. However, while ERA5 data shows the vortex and the change in vorticity caused by BC2017, the increase in water vapor mixing ratios as seen by MLS are not evident in ERA5. Figure 5.10a and b depict water vapor mixing ratios and PV anomalies at 100 hPa on 20 and 21 August. No increase in ERA5 water vapor values is evident inside the plume which is marked by the PV anomaly. Figure 5.10c shows MLS

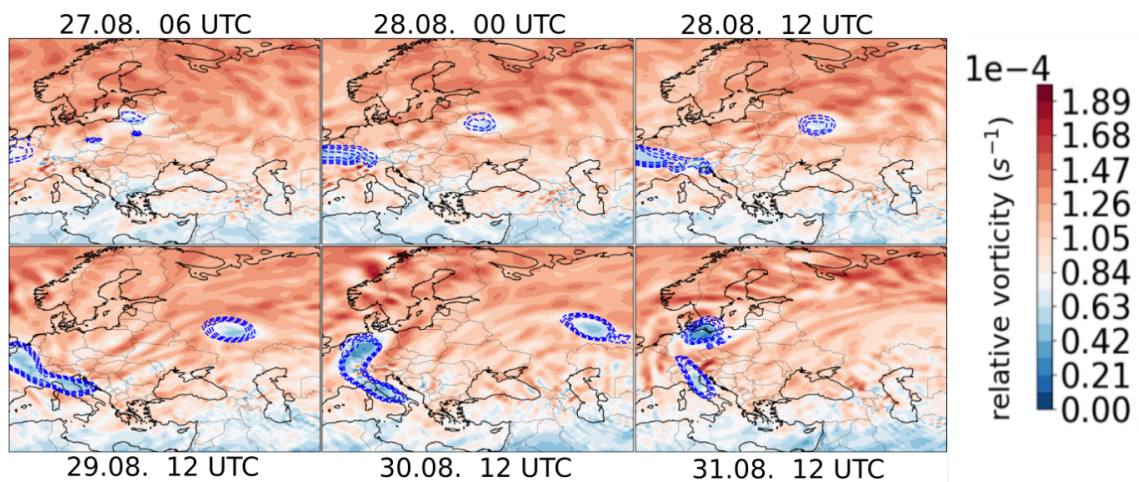


Figure 5.9: ERA5 PV anomaly shown with -8 and -5 PVU contour lines and relative vorticity color-coded at chosen times between the 27 August 2017 and 31 August 2017 at the 68 hPa level of the BC2017 case.

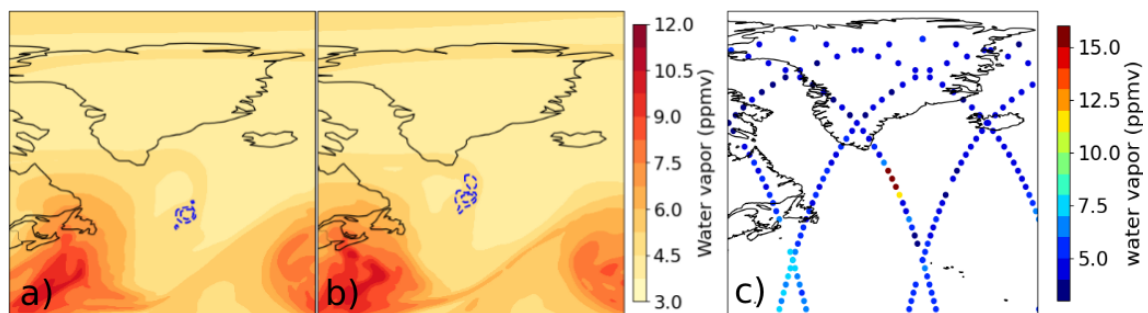


Figure 5.10: Panels a) and b) show the ERA5 water vapor mixing ratio color-coded and PV anomaly with blue contour lines at -5 to -8 PVU on 20 August and 21 August 2017 at 100 hPa for the BC2017 case. Panel c) displays the MLS water vapor measured in the time period in between these two days at the 100 hPa level.

water vapor data in the time period between these two days. It is evident that while the water vapor mixing ratios of about 7 - 10 ppmv south of Newfoundland agree reasonably well between MLS and ERA5 (lower left corner of Fig. 5.10a and b compared to lower left corner of Fig. 5.10c), the strong peak in water vapor produced by the forest fires, south of Greenland, is not evident in ERA5, while MLS shows values above 15 ppmv. However, the peak of water vapor mixing ratios in Fig. 5.10c coincides locally well with the PV anomaly shown in Fig. 5.10a and b.

The same PV anomaly is found for the ANYSO case, as shown exemplarily in Fig. 5.11 regarding relative vorticity. The anomaly also coincides well with the location of the fire plume measured with MLS. The vortex appears first on the 121 hPa pressure level on 3

January 2020 at 12 UTC and there it is detectable until 5 January. The structure appears first on 4 January at the 100 hPa level. From 6 January 18 UTC to 17 January the vortex remains around 120 °E while it is vertically evident at pressures up to 38 hPa. This agrees well with the MLS data shown in Fig. 5.7. Around 15 January the vortex in ERA5 data splits vertically, with one part remaining at the 82 hPa level and moving eastwards after crossing the tip of South America, where the relative vorticity enhances for ≈ 2 days. The second part of the vortex reaches vertically up to 38 hPa. Allen et al. (2020) found that the anticyclonic circulation reached a velocity of 15 m s^{-1} around the in diameter approximately 1000 km large vortex.

ERA5 data show a local minimum in ozone inside the vortex which persists throughout the lifetime of the vortex for both, the BC2017 and the ANYSO case. The ERA5 ozone mixing ratios are shown in Fig. 5.12a and b at the 68 hPa pressure level for both cases, respectively. Khaykin et al. (2020) suggest a combination of the tropospheric origin of the air mass inside the vortex and ozone-depleting chemistry in the smoke loaded plume as explanation for the negative ozone anomaly. While in the BC2017 case the local ozone minimum is about 0.6 ppmv, it is about 1 ppmv in the ANYSO case. Figure D.5 shows the change in ozone inside of the plume as measured by MLS. In agreement with ERA5, MLS ozone shows a decrease at altitudes above 80 hPa. The minimum decline is at about 75 % at the 38 hPa pressure level which roughly agrees with the change shown in ERA5 data (Fig. 5.12).

Similar to the BC2017 case, ERA5 does not show any change in water vapor mixing ratios related to the wild fire plume of ANYSO (not explicitly shown). It can be assumed that water vapor is treated differently in ERA5 than ozone. While ozone is only assimilated from satellite data, water vapor is simulated in the reanalysis which do not represent the vertical transport processes of such extreme and rare cases as the two PyroCbs described here.

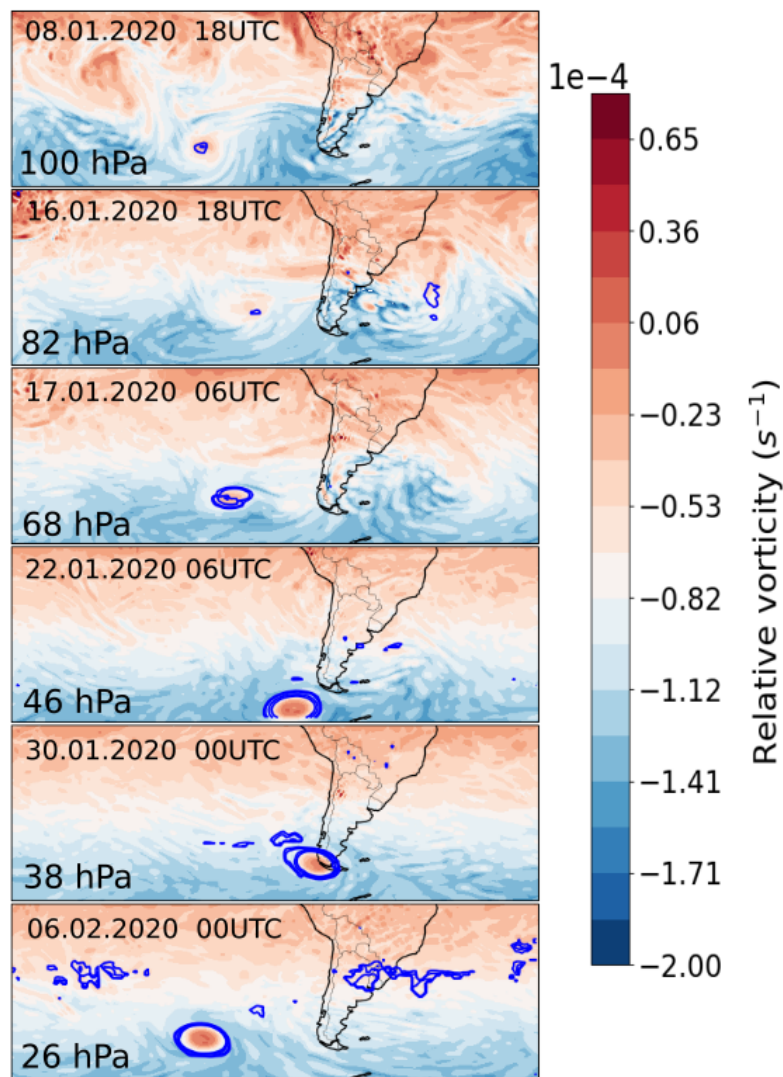


Figure 5.11: ERA5 relative vorticity color-coded with PV anomaly contours at 8, 10, 15 and 20 PVU, at chosen times between the 4 January and 6 February 2020, and at pressure levels of 100, 82, 68, 46, 38 and 26 hPa for the ANYSO case.

5.6 Summary and conclusion

Two wild fire events in the past 5 years had a so far unobserved impact on the stratosphere. High aerosol loadings from both events are comparable to major volcanic eruptions and transport a large amount of chemicals originating from the fires into the stratosphere which apart from that is dynamically separated from the troposphere. The plume of air impacted by the forest fires was identified by a method introduced by Pumphrey et al. (2011a). The increased CO and H₂O mixing ratios measured by MLS coincide with ERA5 PV and relative vorticity anomalies yielding a comprehensive picture of the indi-

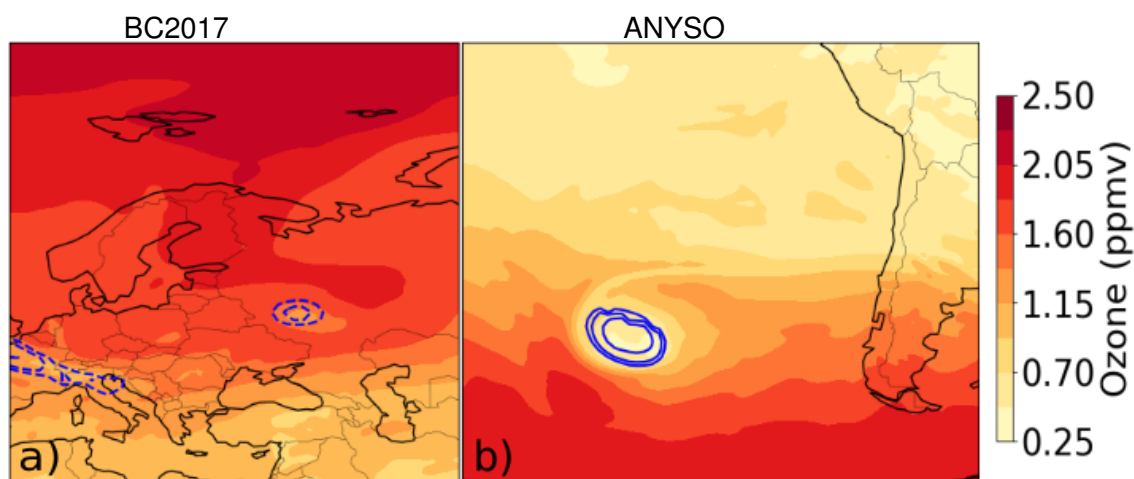


Figure 5.12: ERA5 ozone mixing ratios at the 68 hPa pressure level a) on 29 August 2017 for the BC2017 case with PV anomaly contours at -12, -8 and -6 PVU in blue (dashed) and b) on 15 January 2020 for the ANYSO case with PV anomaly contours at 6, 8 and 12 PVU in blue (solid).

vidual plumes. While ERA5 does not show the observed water vapor anomaly related to each of the wild fire cases, a negative ozone anomaly is evident in ERA5 for both cases. Through the continuous heating of the black carbon aerosols inside the individual plumes, the air masses could pass the barrier between the troposphere and stratosphere and rise to pressure levels of 38 hPa and 12 hPa, respectively. The radiative absorbance of the plumes leads to the formation of a vortex preventing the plume from dilution into the surrounding air, sustaining further heating and rising of the plume.

In both cases similar maximum water vapor mixing ratios at 100 hPa of 19 and 20 ppmv were reached. In the BC2017 case, the PyroCb took place on 12 August 2017 and increased water vapor mixing ratios were first observed in the stratosphere by MLS on 17 August 2017 above Hudsonbai (northeast of Canada) together with an anomaly in relative vorticity and PV as the ERA5 reanalysis data shows. The BC2017 plume was evident for 68 days using CO as a tracer in the MLS measurements between the pressure levels of 121 hPa and 38 hPa. This exceeds the stratospheric lifetime of CO by 8 days defined by Mauzerall et al. (1998) at 12 km altitude. However, the BC2017 plume rose to altitudes above 20 km. This can be explained by a high concentration of black carbon which can alter the photo-chemical reaction rate of CO and OH.

In the ANYSO case, the fire plume is evident for 142 days, starting at 31 December 2019

5.6. Summary and conclusion

to 21 April 2020 at pressure levels between 121 and 12 hPa in the MLS data as well as in ERA5. The plume produced by ANYSO survived significantly longer and had a significantly higher aerosol loading (Khaykin et al., 2020). Another difference to the BC2017 case is the strength and the vertical and horizontal extend of the vortex which maintained a more stable development without multiple splits. At the 12 hPa level the plume shows an unexpected signature with two branches. On showing on average higher ozone values than the other. These branches are also appearing temporally separated at the MLS 12 hPa pressure level. The reason for this, is yet to be identified.

BC2017 and ANYSO are two cases of wild fires within the last 5 years which produced PyroCbs strong enough to inject moist tropospheric air into the stratosphere. This could have significant influence on the water vapor distribution and lead to further implications for the radioactive budget of the stratosphere. Not only the extraordinary water vapor mixing ratio values inside the plume, but also the surprisingly long time period until the air masses in the plume are mixed in with the surrounding air, give reason to consider these kind of events as a significant interference of stratospheric composition and dynamics. As the probability for severe wild fires, like BC2017 and ANYSO, will increase in the future, caused by the ongoing anthropogenic climate change, there is a great need for further studies on PyroCbs.

Chapter 6

Summary and outlook

Water vapor is one of the most relevant greenhouse gases in the atmosphere. Its monitoring and accurate measurement is hence highly relevant for further understanding of the on-going climate change, especially in the Upper Troposphere/ Lower Stratosphere region. This work focuses on instrument tests and advancement of a balloon-borne water vapor instrument as well as on four detailed process case studies of extra-tropical troposphere-to-stratosphere transport of water vapor.

The first two cases are based on the balloon-borne cryogenic frost-point hygrometer (CFH). They focus on the transport of water vapor caused by overshooting convection of a summer storm. Balloon-borne measurements were used to capture the small scale impact of the wave-breaking related mixing of tropospheric air into the dry stratosphere caused by an overshooting top of two meso-scale convective systems which crossed over Germany on two consecutive days, on 10 and 11 June 2019. The measurements show an increase of water vapor mixing ratio up to 6 and 7 ppmv above the background level at pressure levels of 149 and 144 hPa, respectively. Both enhancements are clearly found in the lowermost stratosphere with 40 K of potential temperature above the thermal tropopause. These values are comparable to Smith et al. (2017) and show the relevance of overshooting events not only over Northern America but also over Europe. The air masses captured by the balloon-borne measurement show in both cases a drop of temperature at the level of the water vapor enhancement and in the earlier case diluted ozone

values. The impact of these overshooting events is also evident in ERA5 reanalysis and satellite data. ERA5 water vapor shows enhanced mixing ratios together with enhanced potential vorticity values along backward trajectories of the measured air mass. The change of potential vorticity originates from local changes of the vertical potential temperature gradient triggered by the overshooting convection itself. Brightness temperature data from the geostationary Meteosat-10 satellite show cloud top temperatures along the air mass trajectories with values more than 6 K below the tropopause temperature measured by the balloon radiosonde. This finding strongly supports the evidence of an overshooting event causing the in-mixing of tropospheric air masses into the stratosphere.

Future balloon-borne observations have to be based on a new cooling concept for the CFH. The frost-point-mirror instrument currently requires the cooling agent R-23 in order to cool the mirror and obtain the frost-point of the sampled air. With the ban of the gas due to its high greenhouse potential, an alternative had to be found in order to continue this kind of high-precision measurements. The thesis presents possibilities for alternative cooling agents. A combination of dry ice and ethanol is found to be a realistic replacement for R-23 and could be used in future field studies after adjusting the PID controller of the CFH. The implementation of a copper plate in order to increase the cooling rate and hence to improve the performance of the CFH is successfully tested.

The second two case studies, discussed in Chapter 5, show two events of vigorous wild fires causing water vapor transport into the stratosphere. The analyses are not based on the CFH instrument but on the MLS satellite instrument. The first event occurred in Canada in August 2017 (BC2017) and the second one in Australia between December 2019 and January 2020 (ANYSO). Both cases also lead to so far unseen aerosol loadings in the stratosphere, which are comparable to aerosol loadings after volcanic eruptions. The air masses impacted by the forest fires were heated due to radiative absorption of the high black carbon loading and quickly rose to higher altitudes crossing the tropopause and reaching pressure levels of 38 hPa in the BC2017 case and 12 hPa in the ANYSO case. The air masses contained not only combustion products but also high amount of water vapor. These exceptionally high water vapor values remarkably stand out of the

MLS satellite based water vapor time series of the stratosphere. Maximum water vapor mixing ratios at 100 hPa reach values of 19 ppmv and 20 ppmv, respectively. The air masses affected by the wild fires can be tracked using a method by Pumphrey et al. (2011a), which marks elevated CO values within the plume. In the ANYSO case however, the wild fire plume survived longer than the stratospheric lifetime of CO and, hence, water vapor has to be used as a tracer for the plume.

In both cases, the plume orbited the respective hemisphere within a few weeks. ERA5 potential vorticity data shows anomalies which coincide with the plume measured by MLS. The disturbance in the potential vorticity field is found to be caused by a change of relative vorticity. Continuous heating of the plume induces the formation of a stable vortex which in turn prevents in-mixing of the plume with the surrounding air and leads to the long lifetime of both plumes in the stratosphere. However, ERA5 does not show any enhancement of water vapor, while a negative anomaly in ozone mixing ratios is evident in ERA5 for both cases. The local ozone minimum is most likely caused by a combination of the tropospheric origin of the air masses and by local ozone depleting chemistry inside the vortex.

Two different transport processes of tropospheric air masses crossing the tropopause are discussed in detail in this work. Both transport significant amounts of water vapor into the stratosphere, causing an anomaly in potential vorticity structure. While in the case of overshooting convection the spatial extent of the water vapor enhancement is limited and barely detectable by the MLS satellite, water vapor enhancements caused by the two wild fires are not only detected by MLS but also break any before-seen record of water vapor measurements at stratospheric pressure levels. While the air masses transported by the regular convection into the Upper Troposphere/ Lower Stratosphere region roughly remain at the injected pressure levels, air masses which originated from the wild fires quickly rise to high altitudes after crossing the tropopause and are traceable for a long time period as mixing with surrounding air is prevented by a self-induced vortex. This leads to a negative potential vorticity anomaly in contrast to the convective cases which have a positive potential vorticity anomaly. ERA5 shows water vapor enhance-

ments which correlate well with the balloon measurements, whereas no change of ERA5 water vapor is found in the pyro-convective cases. In summary, both types of convection show the similarity to transport moist tropospheric air masses into the stratosphere, but with different underlying dynamics. However, one aspect is similar for both: with proceeding climate change the conditions favorable for both, extreme convective events and wild fires, are increasing in frequency and it is expected that in the future stronger and more frequent convective and pyro-convective events will occur. It can be assumed that the into the stratosphere transported water vapor will be further fostering global warming leading to a positive feedback loop. The further study of the global impact on both transport processes is hence needed.

As is shown in this work, ECMWF ERA5 data is able to resolve the impact of small scale convective overshooting and Pyrocumulonimbus on the stratosphere. Hence, it is possible to recognize the small-scale changes in the atmospheric structure, which are described in Qu et al. (2020), not only based on sparse local measurements but also on a global scale. It would be of great impact to understand how the frequency and strength of overshooting events changed over the past decades in order to understand what could be expected for the future. The changes in occurrence and severity of convective events might show different behavior in different parts of the globe and respective analyses would strengthen the understanding of its positive feedback importance within the progressing climate change.

List of Figures

2.1	Schematic of convection.	12
2.2	CAPE in a Skew-T diagram.	16
2.3	Dry air entrainment in a convective system.	17
2.4	Schematic of a quall line.	18
2.5	Schematic of a supercell structure.	20
3.1	"Large payload" used for balloon measurements.	24
3.2	Weather balloon and payload launch.	25
3.3	Correlation of CFH and RS41 humidity data	27
3.4	Ozone profiles evaluated with different methods.	30
3.5	Schematic of the CFH instrument	32
3.6	Enthalpy of R-23, CO ₂ , and N ₂ in dependance on temperature.	35
3.7	N ₂ phase diagram.	36
3.8	CO ₂ -ethanol mixture in atmpsheric chamber	37
3.9	Test flights with two CFH	38
3.10	Comparison CFH-23 and CFH-CO ₂ ; flight 25 April 2020	39
3.11	Frostpoint comparison CFH-R23 and CFH-CO ₂ , 1st test	40
3.12	Picture of the copper plate mounted to the cold-finger of the CFH-CO ₂	40
3.13	Comparison CFH-R23 and CFH-CO ₂ ; 22 June 2020	41
3.14	Frostpoint comparison CFH-R23 and CFH-CO ₂ , 2nd test	41
4.1	Schematic of the overshooting measurement strategy	47
4.2	Profiles measured before and after the convective event (Case 1)	54

4.3	Profiles measured before and after the convective event (Case 2)	55
4.4	Climatology of 8 O ₃ profiles measured during spring and summer 2018-2020.	56
4.5	ERA5 ozone mixing ratio at a pressure level of 148 hPa on 11 June 2019 .	57
4.6	ECMWF ERA5 data for Case 1	60
4.7	ECMWF ERA5 data for Case 2	61
4.8	Trajectory of the measured air mass for Case 1 with MLS data	63
4.9	Trajectory of the measured air mass for Case 2 with MLS data	65
4.10	Brightness temperature from Meteosat-10 for Case 1	66
4.11	Brightness temperature from Meteosat-10 for Case 2	67
4.12	Brightness temperature from Meteosat-10 for Case 1 at 18:19 UTC	70
5.1	Timeseries of MLS stratospheric water vapor	80
5.2	H ₂ O and O ₃ tracer-tracer correlation for BC2017 and ANYSO.	82
5.3	BC2017 and ANYSO data as H ₂ O and O ₃ tracer-tracer correlation.	83
5.4	Horizontal distribution of the BC2017 plume.	84
5.5	Horizontal distribution of the ANYSO plume.	85
5.6	Vertical distribution of the BC2017 event.	87
5.7	Vertical distribution of the ANYSO event.	88
5.8	ERA5 PV anomaly and relative vorticity for BC2017.	89
5.9	ERA5 PV anomaly and relative vorticity for BC2017 at 68 hPa.	90
5.10	ERA5 PV anomaly and water vapor compared to MLS.	90
5.11	ERA5 relative vorticity for ANYSO.	92
5.12	Ozone mixing ratios for BC2017 and ANYSO.	93
A.1	Schematic of forces acting on a weather balloon.	125
B.1	Dependence of thermal conductivity of copper on temperature.	127
B.2	Temperature of the cooling agents during the flight on the 25 April 2020. . .	128
B.3	Temperatures of both cooling agents during the flight on the 22 June 2020.	128
C.1	Ozone profiles in Clams simulations	129

D.1 Water vapor in 2020 in the SH with CO and O₃ color-coded 130

D.2 Plume identification for the ANYSO case using water vapor as tracer. . . . 131

D.3 Profile of the horizontal wind component. 132

D.4 ERA5 PV anomalies and dTheta for the BC2017 case. 133

D.5 Vertical distribution of change in ozone in the ANYSO plume. 134

List of Tables

3.1	Statistical evaluation of both CFH comparison flights.	42
5.1	Statistical impact of wild fire cases on stratospheric water vapor.	81

List of abbreviations and acronyms

ANYSO	Australian New Year Super Outbreak	77
AMA	Asian Monsoon Anticyclone	77
BC	British Columbia	75
BT	Brightness Temperature	64
CALIOP	Cloud-Aerosol Lidar and Infrared Pathfinder Satellite Observations	76
CAPE	Convective Available Potential Energy	14
CC	Clausius–Clapeyron equation	6
CCN	Cloud Condensation Nuclei	13
CFH	Cryogenic Frost-point Hygrometer	30
CIN	Convective Inhibition	15
CLaMS	Chemical Lagrangian Model for the Stratosphere	49
COBALD	Compact Optical Backscatter Aerosol Detector	23
CPT	Cold Point Tropopause	19
CT	Chemical Tropopause	20
DT	Dynamical Tropopause	20
ECC	Electrochemical Concentration Cell	23
ECMWF	European Centre for Medium-Range Weather Forecasts	48
EL	Equilibrium Level	14
ESA	European Space Agency	31
ERA5	fifth generation of ECMWF atmospheric global reanalysis	45
EU	European Union	33
FIR	Far-Infrared Range	31

FIRMOS	Far-Infrared Radiation Mobile Observation System	31
FORUM	Far-infrared Outgoing Radiation Understanding and Monitoring	31
FZJ	Forschungszentrum Jülich	45
GHz	Gigahertz	48
GPS	Global Positioning System	24
GRUAN	Global Climate Observing System Reference Upper-Air Network.....	23
IOP	Intense Operational Phase	44
IR	Infrared	64
LED	Light-Emitting Diode	30
LFC	Level of Free Convection	14
LRT	Lapse Rate Tropopause.....	19
LS	Lower Stratosphere	4
MCS	Mesoscale Convective System	18
MLS	Microwave Limb Sounder	45
MOSES	Modular Observation Solutions for Earth Systems.....	4
NA	North American continent	8
NCAR	National Center for Atmospheric Research	37
NH	Northern Hemisphere	87
OT	Overshooting Top	19
PCF	Pump flow Correction Factor	28
PID	Proportional–Integral–Derivative controller	31
PV	Potential Vorticity	20
PVU	Potential Vorticity Units.....	20
PyroCb	Pyrocumulonimbus Clouds	75
R-23	Trifluoromethane, also known as Fluoroform	4
RH	Relative Humidity	26
SEAC4RS	Studies of Emissions, Atmosoheric Composition, Clouds and Climate	
	Coupling by Regional Surveys	68
SH	Southern Hemisphere.....	86

SHADOZ	Southern Hemisphere ADditional OZonesondes	27
TTL	Tropical Tropopause Layer	5
UTC	Coordinated Universal Time	48
UTLS	Upper Troposphere / Lower Stratosphere	5
WMO	World Meteorological Organization	19

Bibliography

- Allen, D. R., Fromm, M. D., Kablick, G. P., and Nedoluha, G. E.: Smoke with induced rotation and lofting (SWIRL) in the stratosphere, *Journal of the Atmospheric Sciences*, 77, 4297–4316, <https://doi.org/10.1175/JAS-D-20-0131.1>, 2020.
- Anderson, J., Wilmouth, D., Smith, J., and Sayers, D.: UV Dosage levels in summer: increased risk of Ozone loss from convectively injected water vapour, *Science*, 337, <https://doi.org/10.1126/science.1222978>, 2012.
- Andreae, M. O., Rosenfeld, D., Artaxo, P., Costa, A. A., Frank, G. P., Longo, K. M., and Silva-Dias, M. A.: Smoking Rain Clouds over the Amazon, *Science*, 303, 1337–1342, <https://doi.org/10.1126/science.1092779>, 2004.
- Ansmann, A., Baars, H., Chudnovsky, A., Mattis, I., Veselovskii, I., Haarig, M., Seifert, P., Engelmann, R., and Wandinger, U.: Extreme levels of Canadian wildfire smoke in the stratosphere over central Europe on 21-22 August 2017, *Atmospheric Chemistry and Physics*, 18, 11 831–11 845, <https://doi.org/10.5194/acp-18-11831-2018>, 2018.
- Balshi, M. S., McGuire, A. D., Duffy, P., Flannigan, M., Walsh, J., and Melillo, J.: Assessing the response of area burned to changing climate in western boreal North America using a Multivariate Adaptive Regression Splines (MARS) approach, *Global Change Biology*, 15, 578–600, <https://doi.org/10.1111/j.1365-2486.2008.01679.x>, 2009.
- Berg, P., Moseley, C., and Haerter, J. O.: Strong increase in convective precipitation in response to higher temperatures, *Nature Geoscience*, 6, 181–185, <https://doi.org/10.1038/ngeo1731>, 2013.
- Berkeley Earth: 2021 Temperature Report, URL <http://berkeleyearth.org/global-temperature-report-for-2021/>, 2021.
- Boer, G.: Climate change and the regulation of the surface moisture and energy budgets, *Climate Dynamics*, 8, 225–239, 1993.

- Boer, M. M., Resco de Dios, V., and Bradstock, R. A.: Unprecedented burn area of Australian mega forest fires, *Nature Climate Change*, 10, 170, <https://doi.org/10.1038/s41558-020-0710-7>, 2020.
- Bond, D., Orville, E., and Boccippio, J.: NO_x production by lightning over the continental data from are in accordance assuming a NO production rate molecules for each CG and produce than despite study, *Journal of Geophysical Research*, 106, 27 701–27 710, 2001.
- Bozem, H., Fischer, H., Gurk, C., Schiller, C. L., Parchatka, U., Koenigstedt, R., Stickler, A., Martinez, M., Harder, H., Kubistin, D., Williams, J., Eerdeken, G., and Lelieveld, J.: Influence of corona discharge on the ozone budget in the tropical free troposphere: A case study of deep convection during GABRIEL, *Atmospheric Chemistry and Physics*, 14, 8917–8931, <https://doi.org/10.5194/acp-14-8917-2014>, 2014.
- Brabec, M., Wienhold, F. G., Luo, B. P., Vömel, H., Immler, F., Steiner, P., Hausammann, E., Weers, U., and Peter, T.: Particle backscatter and relative humidity measured across cirrus clouds and comparison with microphysical cirrus modelling, *Atmospheric Chemistry and Physics*, 12, 9135–9148, <https://doi.org/10.5194/acp-12-9135-2012>, 2012.
- Browning, K. A.: Air Motion and Precipitation Development in Severe Convective Storms, p. 228, URL <https://spiral.imperial.ac.uk/bitstream/10044/1/13642/2/Browning-KA-1962-PhD-Thesis.pdf>, 1962.
- Browning, K. A. and Ludlam, F. H.: Airflow in convective storms, Tech. rep., 1961.
- Carvil, J.: Mechanical Engineer's Data Handbook, Elsevier Ltd, 1 edn., 1993.
- Clements, C. B., Lareau, N. P., Kingsmill, D. E., Bowers, C. L., Camacho, C. P., Bagley, R., and Davis, B.: Observations from the Fire Zone the RAPID deployments to wildfires experiment (RaDFIRE), *Bulletin of the American Meteorological Society*, 99, 2539–2559, <https://doi.org/10.1175/BAMS-D-17-0230.1>, 2018.
- Columbia, G. o. B.: Wildfire Season Summary, URL <https://www2.gov.bc.ca/gov/content/safety/wildfire-status/about-bcws/wildfire-history/wildfire-season-summary>, 2021.
- Cooney, J. W., Bowman, K. P., Homeyer, C. R., and Fenske, T. M.: Ten Year Analysis of Tropopause-Overshooting Convection Using GridRad Data, *Journal of Geophysical Research: Atmospheres*, 123, 329–343, <https://doi.org/10.1002/2017JD027718>, 2018.

- Cooray, V., Rahman, M., and Rakov, V.: On the NO_x production by laboratory electrical discharges and lightning, *Journal of Atmospheric and Solar-Terrestrial Physics*, 71, 1877–1889, <https://doi.org/10.1016/j.jastp.2009.07.009>, 2009.
- Damoah, R., Spichtinger, N., Servranckx, R., Fromm, M., Eloranta, E. W., Razenkov, I. A., James, P., Shulski, M., Forster, C., and Stohl, A.: A case study of pyro-convection using transport model and remote sensing data, *Atmospheric Chemistry and Physics*, 6, 173–185, <https://doi.org/10.5194/acp-6-173-2006>, 2006.
- Dauhut, T., Chaboureau, J. P., Haynes, P. H., and Lane, T. P.: The mechanisms leading to a stratospheric hydration by overshooting convection, *Journal of the Atmospheric Sciences*, 75, 4383–4398, <https://doi.org/10.1175/JAS-D-18-0176.1>, 2018.
- De Groot, W. J., Flannigan, M. D., and Cantin, A. S.: Climate change impacts on future boreal fire regimes, *Forest Ecology and Management*, 294, 35–44, <https://doi.org/10.1016/j.foreco.2012.09.027>, 2013.
- DeCaria, A. J., Pickering, K. E., Stenchikov, G. L., and Ott, L. E.: Lightning-generated NO_x and its impact on tropospheric ozone production: A three-dimensional modeling study of a Stratosphere-Troposphere Experiment: Radiation, Aerosols and Ozone (STERAO-A) thunderstorm, *Journal of Geophysical Research D: Atmospheres*, 110, 1–13, <https://doi.org/10.1029/2004JD005556>, 2005.
- Del Genio, A. D., Yao, M. S., and Jonas, J.: Will moist convection be stronger in a warmer climate?, *Geophysical Research Letters*, 34, 1–5, <https://doi.org/10.1029/2007GL030525>, 2007.
- Deshler, T., Mercer, J. L., Smit, H. G., Stubi, R., Levrat, G., Johnson, B. J., Oltmans, S. J., Kivi, R., Thompson, A. M., Witte, J., Davies, J., Schmidlin, F. J., Brothers, G., and Sasaki, T.: Atmospheric comparison of electrochemical cell ozonesondes from different manufacturers, and with different cathode solution strengths: The Balloon Experiment on Standards for Ozonesondes, *Journal of Geophysical Research Atmospheres*, <https://doi.org/10.1029/2007JD008975>, 2008.
- Dessler, A. E., Zhang, Z., and Yang, P.: Water-vapor climate feedback inferred from climate fluctuations, 2003-2008, *Geophysical Research Letters*, 35, 10–13, <https://doi.org/10.1029/2008GL035333>, 2008.
- Dessler, A. E., Schoeberl, M. R., Wang, T., Davis, S. M., and Rosenlof, K. H.: Stratospheric

- water vapor feedback, *Proceedings of the National Academy of Sciences*, 110, <https://doi.org/10.1073/pnas.1310344110>, 2013.
- Dessler, A. E., Schoeberl, M. R., Wang, T., Davis, S. M., Rosenlof, K. H., and Vernier, J. P.: Variations of stratospheric water vapor over the past three decades, *Journal of Geophysical Research Atmospheres*, 119, <https://doi.org/10.1002/2014JD021712>, 2014.
- Dirksen, R. J., Sommer, M., Immler, F. J., Hurst, D. F., Kivi, R., and Vömel, H.: Reference quality upper-air measurements: GRUAN data processing for the Vaisala RS92 radiosonde, *Atmospheric Measurement Techniques*, 7, 4463–4490, <https://doi.org/10.5194/amt-7-4463-2014>, 2014.
- Dirksen, R. J., Bodeker, G. E., Thorne, P. W., Merlone, A., Reale, T., Wang, J., Hurst, D. F., Demoz, B. B., Gardiner, T. D., Ingleby, B., Sommer, M., Von Rohden, C., and Leblanc, T.: Managing the transition from Vaisala RS92 to RS41 radiosondes within the Global Climate Observing System Reference Upper-Air Network (GRUAN): A progress report, *Geoscientific Instrumentation, Methods and Data Systems*, 9, 337–355, <https://doi.org/10.5194/gi-9-337-2020>, 2020.
- Doswell III, C. A.: *Severe Convective Storms*, 2001.
- Doswell III, C. A.: Historical Overview of Severe Convective Storms Research, *Electronic J. Severe Storms Meteor*, 2, 1–25, 2007.
- Ertel, H.: Ein neuer hydrodynamischer Erhaltungssatz, *Die Naturwissenschaften*, 30, 543–544, <https://doi.org/10.1007/BF01475602>, 1942.
- EU: Verordnung (EU) Nr. 517/2014 des Europäischen Parlaments und des Rates vom 16. April 2014 über fluoridierte Treibhausgase und zur Aufhebung der Verordnung (EG) Nr. 842/2006, *Amtsblatt der Europäischen Union (L 150)*, 2014, 195 – 230, 2014.
- Feng, Z., Leung, L. R., Hagos, S., Houze, R. A., Burleyson, C. D., and Balaguru, K.: More frequent intense and long-lived storms dominate the springtime trend in central US rainfall, *Nature Communications*, 7, 1–8, <https://doi.org/10.1038/ncomms13429>, 2016.
- Fischer, H., De Reus, M., Traub, M., Williams, J., Lelieveld, J., De Gouw, J., Warneke, C., Schlager, H., Minikin, A., Scheele, R., and Siegmund, P.: Deep convective injection of boundary layer air into the lowermost stratosphere at midlatitudes, *Atmospheric Chemistry and Physics*, 3, 739–745, <https://doi.org/10.5194/acp-3-739-2003>, 2003.

- Forster, P. M. F. and Shine, K. P.: Stratospheric water vapour changes as a possible contributor to observed stratospheric cooling, *Geophysical Research Letters*, <https://doi.org/10.1029/1999GL010487>, 1999.
- Fromm, M., Lindsey, D. T., Servranckx, R., Yue, G., Trickl, T., Sica, R., Doucet, P., and Godin-Beekmann, S.: The untold story of pyrocumulonimbus, *Bulletin of the American Meteorological Society*, 91, 1193–1209, <https://doi.org/10.1175/2010BAMS3004.1>, 2010.
- Fujita, T. T.: *Manual of Downburst Identification*, pp. 51–67, 1978.
- Fujita, T. T.: Principle of Stereoscopic Height Computations and their Applications to Stratospheric Cirrus over Severe Thunderstorms, *Journal of the Meteorological Society of Japan. Ser. II*, 60, 355–368, https://doi.org/10.2151/jmsj1965.60.1_355, 1982.
- Gottelman, A., Hoor, P., Pan, L. L., Randel, W. J., Hegglin, M. I., and Birner, T.: The extratropical upper troposphere and lower stratosphere, *Rev. Geophys.*, 49, <https://doi.org/10.1029/2011RG000355>, 2011.
- Gillett, N. P., Weaver, A. J., Zwiers, F. W., and Flannigan, M. D.: Detecting the effect of climate change on Canadian forest fires, *Geophysical Research Letters*, 31, <https://doi.org/10.1029/2004GL020876>, 2004.
- Hansen, J. E.: A slippery slope: How much global warming constitutes "dangerous anthropogenic interference"? An editorial essay, *Climatic Change*, 68, 269–279, <https://doi.org/10.1007/s10584-005-4135-0>, 2005.
- Hegglin, M. I., Brunner, D., Wernli, H., Schwierz, C., Martius, O., Hoor, P., Fischer, H., Parchatka, U., Spelten, N., Schiller, C., Krebsbach, M., Weers, U., Staehelin, J., and Peter, T.: Tracing troposphere-to-stratosphere transport above a mid-latitude deep convective system, *Atmospheric Chemistry and Physics*, 4, 741–756, <https://doi.org/10.5194/acp-4-741-2004>, 2004.
- Hegglin, M. I., Boone, C. D., Manney, G. L., and Walker, K. A.: A global view of the extratropical tropopause transition layer from Atmospheric Chemistry Experiment Fourier Transform Spectrometer O₃, H₂O, and CO, *Journal of Geophysical Research Atmospheres*, 114, 1–18, <https://doi.org/10.1029/2008JD009984>, 2009.
- Hegglin, M. I., Plummer, D. A., Shepherd, T. G., Scinocca, J. F., Anderson, J., Froidevaux, L., Funke, B., Hurst, D., Rozanov, A., Urban, J., Von Clarmann, T., Walker, K. A., Wang, H. J.,

- Tegtmeier, S., and Weigel, K.: Vertical structure of stratospheric water vapour trends derived from merged satellite data, *Nature Geoscience*, <https://doi.org/10.1038/NGEO2236>, 2014.
- Herring, S. C., Hoerling, M. P., Kossin, J. P., Peterson, T. C., and Stott, P. A.: Explaining Extreme Events of 2014 From a climate perspective, *Bulletin of the American Meteorological Society*, 96, 35–40, 2015.
- Herring, S. C., Hoerling, M. P., Peterson, T. C., and Stott, P. A.: Explaining Extreme Events of 2019 from a Climate Perspective Special, *Bulletin of the American Meteorological Society*, 95, S1–S96, <https://doi.org/10.1175/1520-0477-95.9.s1.1>, 2021.
- Hersbach, H., Bell, B., Berrisford, P., Hirahara, S., Horányi, A., Muñoz-Sabater, J., Nicolas, J., Peubey, C., Radu, R., Schepers, D., Simmons, A., Soci, C., Abdalla, S., Abellan, X., Balsamo, G., Bechtold, P., Biavati, G., Bidlot, J., Bonavita, M., De Chiara, G., Dahlgren, P., Dee, D., Diamantakis, M., Dragani, R., Flemming, J., Forbes, R., Fuentes, M., Geer, A., Haimberger, L., Healy, S., Hogan, R. J., Hólm, E., Janisková, M., Keeley, S., Laloyaux, P., Lopez, P., Lupu, C., Radnoti, G., de Rosnay, P., Rozum, I., Vamborg, F., Villaume, S., and Thépaut, J. N.: The ERA5 global reanalysis, *Quarterly Journal of the Royal Meteorological Society*, 146, 1999–2049, <https://doi.org/10.1002/qj.3803>, 2020.
- Hoinka, K. P.: The tropopause: Discovery, definition and demarcation, <https://doi.org/10.1127/metz/6/1997/281>, 1997.
- Homeyer, C. R. and Kumjian, M. R.: Microphysical characteristics of overshooting convection from polarimetric radar observations, *Journal of the Atmospheric Sciences*, 72, 870–891, <https://doi.org/10.1175/JAS-D-13-0388.1>, 2015.
- Homeyer, C. R., McAuliffe, J. D., and Bedka, K. M.: On the development of above-anvil cirrus plumes in extratropical convection, *Journal of the Atmospheric Sciences*, 74, 1617–1633, <https://doi.org/10.1175/JAS-D-16-0269.1>, 2017.
- Jauhiainen, H., Survo, P., Lehtinen, R., and Lentonen, J.: Radiosonde RS41 and RS92 key differences and comparison test results in different locations and climates, in: *TECO 2014*, pp. 2–6, 2014.
- Jensen, E. J., Pan, L. L., Honomichl, S., Diskin, G. S., Krämer, M., Spelten, N., Günther, G., Hurst, D. F., Fujiwara, M., Vömel, H., Selkirk, H. B., Suzuki, J., Schwartz, M. J., and Smith, J. B.: Assessment of Observational Evidence for Direct Convective Hydration of the Lower

- Stratosphere, *Journal of Geophysical Research: Atmospheres*, 125, 1–12, <https://doi.org/10.1029/2020JD032793>, 2020.
- Johnson, B. J., Oltmans, S. J., Vömel, H., Smit, H. G. J., Deshler, T., and Kröger, C.: Electrochemical concentration cell (ECC) ozonesonde pump efficiency measurements and tests on the sensitivity to ozone of buffered and unbuffered ECC sensor cathode solutions, *Journal of Geophysical Research Atmospheres*, <https://doi.org/10.1029/2001JD000557>, 2002.
- Jost, H. J., Drdla, K., Stohl, A., Pfister, L., Loewenstein, M., Lopez, J. P., Hudson, P. K., Murphy, D. M., Cziczo, D. J., Fromm, M., Bui, T. P., Dean-Day, J., Gerbig, C., Mahoney, M. J., Richard, E. C., Spichtinger, N., Pittman, J. V., Weinstock, E. M., Wilson, J. C., and Xueref, I.: In-situ observations of mid-latitude forest fire plumes deep in the stratosphere, *Geophysical Research Letters*, 31, 1–5, <https://doi.org/10.1029/2003GL019253>, 2004.
- Kablick, G., Fromm, M., Miller, S., Partain, P., Peterson, D., Lee, S., Zhang, Y., Lambert, A., and Li, Z.: The Great Slave Lake PyroCb of 5 August 2014: Observations, Simulations, Comparisons With Regular Convection, and Impact on UTLS Water Vapor, *Journal of Geophysical Research: Atmospheres*, 123, 12,332–12,352, <https://doi.org/10.1029/2018JD028965>, 2018.
- Kablick, G. P., Allen, D. R., Fromm, M. D., and Nedoluha, G. E.: Australian PyroCb Smoke Generates Synoptic-Scale Stratospheric Anticyclones, *Geophysical Research Letters*, 47, <https://doi.org/10.1029/2020GL088101>, 2020.
- Kar, J., Lee, K. P., Vaughan, M. A., Tackett, J. L., Trepte, C. R., Winker, D. M., Lucker, P. L., and Getzewich, B. J.: CALIPSO level 3 stratospheric aerosol profile product: Version 1.00 algorithm description and initial assessment, *Atmospheric Measurement Techniques*, 12, 6173–6191, <https://doi.org/10.5194/amt-12-6173-2019>, 2019.
- Kasischke, E. S. and Turetsky, M. R.: Recent changes in the fire regime across the North American boreal region - Spatial and temporal patterns of burning across Canada and Alaska, *Geophysical Research Letters*, 33, <https://doi.org/10.1029/2006GL025677>, 2006.
- Kawai, Y., Katsumata, M., Oshima, K., Hori, M. E., and Inoue, J.: Comparison of Vaisala radiosondes RS41 and RS92 launched over the oceans from the Arctic to the tropics, *Atmospheric Measurement Techniques*, 10, 2485–2498, <https://doi.org/10.5194/amt-10-2485-2017>, 2017.
- Khaykin, S., Legras, B., Bucci, S., Sellitto, P., Isaksen, L., Tencé, F., Bekki, S., Bourassa, A., Rieger, L., Zawada, D., Jumelet, J., and Godin-Beekmann, S.: The 2019/20 Australian wildfires

- generated a persistent smoke-charged vortex rising up to 35 km altitude, *Communications Earth & Environment*, 1, 1–12, <https://doi.org/10.1038/s43247-020-00022-5>, 2020.
- Khaykin, S. M., Godin-Beekmann, S., Hauchecorne, A., Pelon, J., Ravetta, F., and Keckhut, P.: Stratospheric Smoke With Unprecedentedly High Backscatter Observed by Lidars Above Southern France, *Geophysical Research Letters*, 45, 1639–1646, <https://doi.org/10.1002/2017GL076763>, 2018.
- Khaykin, S. M., Moyer, E., Krämer, M., Clouser, B., Bucci, S., Lykov, A., Afchine, A., Cairo, F., Formanyuk, I., Mitev, V., Rolf, C., Singer, C., Spelten, N., Volkov, V., and Yushkov, V.: Persistence of moist plumes from overshooting convection in the Asian monsoon anticyclone, pp. 1–27, 2021.
- Khordakova, D., Rolf, C., Groöß, J.-U., Müller, R., Konopka, P., Wieser, A., Krämer, M., and Riese, M.: A case study on the impact of severe convective storms on the water vapor mixing ratio in the lower mid-latitude stratosphere observed in 2019 over Europe, *Atmospheric Chemistry and Physics*, 22, 1059–1079, <https://doi.org/10.5194/acp-22-1059-2022>, 2022.
- Kirchmeier-Young, M. C., Gillett, N. P., Zwiers, F. W., Cannon, A. J., and Anslow, F. S.: Attribution of the Influence of Human-Induced Climate Change on an Extreme Fire Season, *Earth's Future*, 7, 2–10, <https://doi.org/10.1029/2018EF001050>, 2019.
- Klanner, L., Höveler, K., Khordakova, D., Perfahl, M., Rolf, C., Trickl, T., and Vogelmann, H.: A powerful lidar system capable of 1h measurements of water vapour in the troposphere and the lower stratosphere as well as the temperature in the upper stratosphere and mesosphere, *Atmospheric Measurement Techniques*, 14, 531–555, <https://doi.org/10.5194/amt-14-531-2021>, 2021.
- Kloss, C., Berthet, G., Sellitto, P., Ploeger, F., Bucci, S., Khaykin, S., Jégou, F., Taha, G., Thomason, L. W., Barret, B., Le Flochmoen, E., Von Hobe, M., Bossolasco, A., Bègue, N., and Legras, B.: Transport of the 2017 canadian wildfire plume to the tropics via the asian monsoon circulation, *Atmospheric Chemistry and Physics*, 19, 13547–13567, <https://doi.org/10.5194/acp-19-13547-2019>, 2019.
- Komhyr, W.: Operations handbook - ozone measurements to 40-km altitude with model 4A electrochemical concentration cell (ECC) ozonesondes (used with 1680-MHz-radiosondes), URL <https://www.osti.gov/biblio/6966940>, 1986.

- Komhyr, W. D., Barnes, R. A., Brothers, G. B., Lathrop, J. A., and Opperman, D. P.: Electrochemical concentration cell ozonesonde performance evaluation during STOIC 1989, *Journal of Geophysical Research*, 100, 9231–9244, <https://doi.org/10.1029/94JD02175>, 1995.
- Kotsakis, A., Morris, G. A., Lefer, B., Jeon, W., Roy, A., Minschwaner, K., Thompson, A. M., and Choi, Y.: Ozone production by corona discharges during a convective event in DISCOVER-AQ Houston, *Atmospheric Environment*, 161, 13–17, <https://doi.org/10.1016/j.atmosenv.2017.04.018>, 2017.
- Krebsbach, M., Schiller, C., Brunner, D., Günther, G., Hegglin, M. I., Mottaghy, D., Riese, M., Spelten, N., and Wernli, H.: Seasonal cycles and variability of O₃ and H₂O in the UT/LMS during SPURT, *Atmospheric Chemistry and Physics*, 6, 109–125, <https://doi.org/10.5194/acp-6-109-2006>, 2006.
- Kunz, A., Konopka, P., Müller, R., and Pan, L. L.: Dynamical tropopause based on isentropic potential vorticity gradients, *Journal of Geophysical Research Atmospheres*, 116, 1–13, <https://doi.org/10.1029/2010JD014343>, 2011a.
- Kunz, A., Konopka, P., Müller, R., and Pan, L. L.: Dynamical tropopause based on isentropic potential vorticity gradients, *Journal of Geophysical Research Atmospheres*, 116, 1–13, <https://doi.org/10.1029/2010JD014343>, 2011b.
- Labitzke, K. G.: *Die Stratosphäre - Phänomene, Geschichte, Relevanz*, Springer Berlin Heidelberg, 1 edn., 1999.
- Laboratory, G. M.: Trends in Atmospheric Carbon Dioxide, URL <https://gml.noaa.gov/ccgg/trends/global.html>, 2021.
- Lenderink, G. and Van Meijgaard, E.: Increase in hourly precipitation extremes beyond expectations from temperature changes, *Nature Geoscience*, 1, 511–514, <https://doi.org/10.1038/ngeo262>, 2008.
- Lestrelin, H., Legras, B., Podglajen, A., and Salihoglu, M.: Smoke-charged vortices in the stratosphere generated by wildfires and their behaviour in both hemispheres: Comparing Australia 2020 to Canada 2017, *Atmospheric Chemistry and Physics*, 21, 7113–7134, <https://doi.org/10.5194/acp-21-7113-2021>, 2021.
- Livesey, N. J., Read, W. G., A. Wagner, P., Froidevaux, L., Lambert, A., L. Manney, G., Valle, L. F., Pumphrey, H. C., Santee, M. L., Schwartz, M. J., Wang, S., Fuller, R. A., Jarnot, R. F., Knosp,

- B., and Martinez, E.: Version 4.2x Level data quality and description document, Tech. rep., URL <http://disc.gsfc.nasa.gov/>, 2017.
- Lüthi, D., Le Floch, M., Bereiter, B., Blunier, T., Barnola, J. M., Siegenthaler, U., Raynaud, D., Jouzel, J., Fischer, H., Kawamura, K., and Stocker, T. F.: High-resolution carbon dioxide concentration record 650,000-800,000 years before present, *Nature*, 453, 379–382, <https://doi.org/10.1038/nature06949>, 2008.
- Masson-Delmotte, V., Zhai, P., Pirani, A., Connors, S. L., Péan, C., Berger, S., Caud, N., Chen, Y., Goldfarb, L., Gomis, M. I., Huang, M., Leitzell, K., Lonnoy, E., Matthews, J., Maycock, T. K., Waterfield, T., Yelekçi, O., Yu, R., Zhou, B., and (eds.): IPCC: Climate Change 2021: The Physical Science Basis, Cambridge University Press. In Press., p. 42, URL <https://www.ipcc.ch/report/ar6/wg1/>, 2021.
- Mauzerall, D. L., Logan, J. A., Jacob, D. J., Anderson, B. E., Blake, D. R., Bradshaw, J. D., Heikes, B., Sachse, G. W., Singh, H., and Talbot, B.: Photochemistry in biomass burning plumes and implications for tropospheric ozone over the tropical South Atlantic, *Journal of Geophysical Research Atmospheres*, 103, 8401–8423, <https://doi.org/10.1029/97JD02612>, 1998.
- McKenna, D. S., Grooß, J. U., Günther, G., Konopka, P., Müller, R., Carver, G., and Sasano, Y.: A new Chemical Lagrangian Model of the Stratosphere (CLaMS) 2. Formulation of chemistry scheme and initialization, *Journal of Geophysical Research Atmospheres*, 107, <https://doi.org/10.1029/2000JD000113>, 2002.
- Mersereau, D.: What Is a Supercell Thunderstorm?, URL <http://thevane.gawker.com/what-is-a-supercell-thunderstorm-1564133584>, 2014.
- Minschwaner, K., Kalnajs, L. E., Dubey, M. K., Avallone, L. M., Sawaengphokai, P. C., Edens, H. E., and Winn, W. P.: Observation of enhanced ozone in an electrically active storm over Socorro, NM: Implications for ozone production from corona discharges, *Journal of Geophysical Research Atmospheres*, 113, 1–7, <https://doi.org/10.1029/2007JD009500>, 2008.
- Minschwaner, K., Manney, G. L., Livesey, N. J., Pumphrey, H. C., Pickett, H. M., Froidevaux, L., Lambert, A., Schwartz, M. J., Bernath, P. F., Walker, K. A., and Boone, C. D.: The photochemistry of carbon monoxide in the stratosphere and mesosphere evaluated from observations by the Microwave Limb Sounder on the Aura satellite, *Journal of Geophysical Research Atmospheres*, 115, 1–9, <https://doi.org/10.1029/2009JD012654>, 2010.

- Mote, P. W., Rosenlof, K. H., McIntyre, E., Carr, E. S., Gille, J. C., Holton, R., Kinnersley, S., Pumphrey, H. C., Russell, M., and Wal, J. W.: An atmospheric tape recorder ' The imprint of tropical tropopause temperatures on stratospheric water vapor s observed phase lag agrees with the phase lag calculated assuming advection by the The phase agreement confirms the overall robustness of the calc, *Journal of Geophysical Research*, 101, 3989–4006, 1996.
- MunichRE: Risks posed by natural disasters, URL <http://berkeleyearth.org/global-temperature-report-for-2021/>, 2021.
- Murphy, D. M. and Koop, T.: Review of the vapour pressures of ice and supercooled water for atmospheric applications, <https://doi.org/10.1256/qj.04.94>, 2005.
- NASA Earth Observatory: Record-Breaking Smoke Over Canada, URL <https://earthobservatory.nasa.gov/images/90759/record-breaking-smoke-over-canada>, 2017.
- Nash, J., Oakley, T., Vömel, H., and Wei, L.: World Meteorological Organization Instruments and observing methods Report No. 107, Tech. rep., 2010.
- Newell, R. E.: Transfer through the tropopause and within the stratosphere, *Quarterly Journal of the Royal Meteorological Society*, 89, 167–204, <https://doi.org/10.1002/qj.49708938002>, 1963.
- Oltmans, S. J., Vomel, H., Hofmann, D. J., Rosenlof, K. H., and Kley, D.: The increase in stratospheric water vapor from balloonborne, frostpoint hygrometer measurements at Washington, D.C., and Boulder, Colorado, *Geophysical Research Letters*, 27, 3453–3456, <https://doi.org/10.1029/2000GL012133>, 2000.
- Pachauri, R. K. and Meyer, L.: Climate Change 2014 Synthesis Report Managing the Risks of Extreme Events and Disasters to Advance Climate Change Adaptation: Special Report of the Intergovernmental Panel on Climate Change, IPCC, 9781107025, 3–22, <https://doi.org/10.1017/CBO9781139177245.003>, 2014.
- Palchetti, L., Barucci, M., Belotti, C., Bianchini, G., Cluzet, B., D'Amato, F., Del Bianco, S., Di Natale, G., Gai, M., Khordakova, D., Montori, A., Oetjen, H., Rettinger, M., Rolf, C., Schuetttemeyer, D., Sussmann, R., Viciani, S., Vogelmann, H., and Wienhold, F. G.: Observations of the downwelling far-infrared atmospheric emission at the Zugspitze observatory, *Earth System Science Data*, 13, 4303–4312, <https://doi.org/10.5194/essd-13-4303-2021>, 2021.

- Pall, P., Allen, M. R., and Stone, D. A.: Testing the Clausius-Clapeyron constraint on changes in extreme precipitation under CO₂ warming, *Climate Dynamics*, 28, 351–363, <https://doi.org/10.1007/s00382-006-0180-2>, 2007.
- Pan, L. L., Hintsala, E. J., Stone, M., Weinstock, E. M., and Randel, W. J.: The seasonal cycle of water vapor and saturation vapor mixing ratio in the extratropical lowermost stratosphere, *Journal of Geophysical Research*, 105, 26 519–26 530, 2000.
- Peterson, D. A., Hyer, E. J., Campbell, J. R., Solbrig, J. E., and Fromm, M. D.: A conceptual model for development of intense pyrocumulonimbus in western North America, *Monthly Weather Review*, 145, 2235–2255, <https://doi.org/10.1175/MWR-D-16-0232.1>, 2017.
- Peterson, D. A., Campbell, J. R., Hyer, E. J., Fromm, M. D., Kablick, G. P., Cossuth, J. H., and DeLand, M. T.: Wildfire-driven thunderstorms cause a volcano-like stratospheric injection of smoke, *npj Climate and Atmospheric Science*, 1, 1–8, <https://doi.org/10.1038/s41612-018-0039-3>, 2018.
- Peterson, D. A., Fromm, M. D., McRae, R. H., Campbell, J. R., Hyer, E. J., Taha, G., Camacho, C. P., Kablick, G. P., Schmidt, C. C., and DeLand, M. T.: Australia’s Black Summer pyrocumulonimbus super outbreak reveals potential for increasingly extreme stratospheric smoke events, *npj Climate and Atmospheric Science*, 4, 1–16, <https://doi.org/10.1038/s41612-021-00192-9>, 2021.
- Peterson, T. C., Stott, P. A., and Herring, S.: Explaining extreme events of 2011 from a climate perspective, *Bulletin of the American Meteorological Society*, 95, S1–S96, <https://doi.org/10.1175/1520-0477-95.9.s1.1>, 2012.
- Phoenix, D. B. and Homeyer, C. R.: Simulated Impacts of Tropopause-Overshooting Convection on the Chemical Composition of the Upper Troposphere and Lower Stratosphere, *Journal of Geophysical Research: Atmospheres*, <https://doi.org/10.1029/2021jd034568>, 2021.
- Pumphrey, H., Schwartz, M., Santee, M., Kablick III, G., Fromm, M., and Livesey, N.: Stratospheric pollution from Canadian forest fires, *Atmospheric Chemistry and Physics*, pp. 1–19, <https://doi.org/10.5194/acp-2020-840>, 2020.
- Pumphrey, H. C., Santee, M. L., Livesey, N. J., Schwartz, M. J., and Read, W. G.: Microwave Limb Sounder observations of biomass-burning products from the Australian bush

- fires of February 2009, *Atmospheric Chemistry and Physics*, 11, 6285–6296, <https://doi.org/10.5194/acp-11-6285-2011>, 2011a.
- Pumphrey, H. C., Santee, M. L., Livesey, N. J., Schwartz, M. J., and Read, W. G.: Microwave Limb Sounder observations of biomass-burning products from the Australian bush fires of February 2009, *Atmospheric Chemistry and Physics*, 11, 6285–6296, <https://doi.org/10.5194/acp-11-6285-2011>, 2011b.
- Qu, Z., Huang, Y., Vaillancourt, P. A., Cole, J. N., Milbrandt, J. A., Yau, M. K., Walker, K., and De Grandpré, J.: Simulation of convective moistening of the extratropical lower stratosphere using a numerical weather prediction model, *Atmospheric Chemistry and Physics*, 20, 2143–2159, <https://doi.org/10.5194/acp-20-2143-2020>, 2020.
- Randel, W. J., Wu, F., Russell, J. M., Roche, A., and Waters, J. W.: Seasonal cycles and QBO variations in stratospheric CH₄ and H₂O observed in UARS HALOE data, *Journal of the Atmospheric Sciences*, 55, 163–185, [https://doi.org/10.1175/1520-0469\(1998\)055<0163:SCAQVI>2.0.CO;2](https://doi.org/10.1175/1520-0469(1998)055<0163:SCAQVI>2.0.CO;2), 1998.
- Ravikumar, D. K., Than, Y., Xu, W., and Longtin, J.: Thermal considerations in the cryogenic regime for the BNL double ridge higher order mode waveguide, *Physical Review Accelerators and Beams*, 20, 1–7, <https://doi.org/10.1103/PhysRevAccelBeams.20.093201>, 2017.
- Reed, R. J.: A study of a characteristic type of upper-level frontogenesis, *Journal of meteorology*, 148, 148–162, 1954.
- Reinartz, T.: Radiosonden: Von (Daten-) Jägern zu Gejagten, URL https://www.dwd.de/DE/wetter/thema{}_des{}_tages/2020/6/29.html, 2020.
- Ricaud, P., Barret, B., Attié, J. L., Motte, E., Le Flochmoën, E., Teysseire, H., Peuch, V. H., Livesey, N., Lambert, A., and Pommereau, J. P.: Impact of land convection on troposphere-stratosphere exchange in the tropics, *Atmospheric Chemistry and Physics*, 7, 5639–5657, <https://doi.org/10.5194/acp-7-5639-2007>, 2007.
- Riese, M., Ploeger, F., Rap, A., Vogel, B., Konopka, P., Dameris, M., and Forster, P.: Impact of uncertainties in atmospheric mixing on simulated UTLS composition and related radiative effects, *Journal of Geophysical Research Atmospheres*, <https://doi.org/10.1029/2012JD017751>, 2012.

- Robrecht, S., Vogel, B., Grooß, J. U., Rosenlof, K., Thornberry, T., Rollins, A., Krämer, M., Christensen, L., and Müller, R.: Mechanism of ozone loss under enhanced water vapour conditions in the mid-latitude lower stratosphere in summer, *Atmospheric Chemistry and Physics*, 19, 5805–5833, <https://doi.org/10.5194/acp-19-5805-2019>, 2019.
- Robrecht, S., Vogel, B., Tilmes, S., and Müller, R.: Potential of future stratospheric ozone loss in the mid-latitudes under climate change and sulfate geoengineering, *Atmospheric Chemistry and Physics*, pp. 1–40, <https://doi.org/10.5194/acp-2020-747>, 2020.
- Rodriguez, B., Lareau, N. P., Kingsmill, D. E., and Clements, C. B.: Extreme Pyroconvective Updrafts During a Megafire, *Geophysical Research Letters*, 47, 1–9, <https://doi.org/10.1029/2020GL089001>, 2020.
- Rolf, C., Vogel, B., Hoor, P., Afchine, A., Günther, G., Krämer, M., Müller, R., Müller, S., Spelten, N., and Riese, M.: Water vapor increase in the lower stratosphere of the Northern Hemisphere due to the Asian monsoon anticyclone observed during the TACTS/ESMVal campaigns, *Atmospheric Chemistry and Physics*, 18, 2973–2983, <https://doi.org/10.5194/acp-18-2973-2018>, 2018.
- Romps, D. M.: Response of tropical precipitation to global warming, *Journal of the Atmospheric Sciences*, 68, 123–138, <https://doi.org/10.1175/2010JAS3542.1>, 2011.
- Rosenfeld, D., Fromm, M., Trentmann, J., Luderer, G., Andreae, M. O., and Servranckx, R.: The Chisholm firestorm: Observed microstructure, precipitation and lightning activity of a pyro-cumulonimbus, *Atmospheric Chemistry and Physics*, 7, 645–659, <https://doi.org/10.5194/acp-7-645-2007>, 2007.
- Rosenlof, H. and Kley, D.: Stratospheric water vapor increases over the past half-century, *Geophysical Research Letters*, 28, 1195–1198, 2001.
- Schoeberl, M. R., Douglass, A. R., Hilsenrath, E., Bhartia, P. K., Beer, R., Waters, J. W., Gunson, M. R., Froidevaux, L., Gille, J. C., Barnett, J. J., Levelt, P. F., and DeCola, P.: Overview of the EOS aura mission, *IEEE Transactions on Geoscience and Remote Sensing*, 44, 1066–1072, <https://doi.org/10.1109/TGRS.2005.861950>, 2006.
- Seinfeld, J. and Pandis, S.: *Atmospheric Chemistry and Physics From Air Pollution to Climate Change*, Wiley, 3 edn., 2016.

- Smit, H. G. J., Straeter, W., Johnson, B. J., Oltmans, S. J., Davies, J., Tarasick, D. W., Hoegger, B., Stubi, R., Schmidlin, F. J., Northam, T., Thompson, A. M., Witte, J. C., Boyd, I., and Posny, F.: Assessment of the performance of ECC-ozonesondes under quasi-flight conditions in the environmental simulation chamber: Insights from the Juelich Ozone Sonde Intercomparison Experiment (JOSIE), *Journal of Geophysical Research Atmospheres*, <https://doi.org/10.1029/2006JD007308>, 2007.
- Smith, J. B., Wilmouth, D. M., Bedka, K. M., Bowman, K. P., Homeyer, C. R., Dykema, J. A., Sargent, M. R., Clapp, C. E., Leroy, S. S., Sayres, D. S., Dean-Day, J. M., Paul Bui, T., and Anderson, J. G.: A case study of convectively sourced water vapor observed in the overworld stratosphere over the United States, *Journal of Geophysical Research: Atmospheres*, <https://doi.org/10.1002/2017JD026831>, 2017.
- Solomon, D. L., Bowman, K. P., and Homeyer, C. R.: Tropopause-penetrating convection from three-dimensional gridded NEXRAD data, *Journal of Applied Meteorology and Climatology*, 55, 465–478, <https://doi.org/10.1175/JAMC-D-15-0190.1>, 2016.
- Solomon, S., Rosenlof, K. H., Portmann, R. W., Daniel, J. S., Davis, S. M., Sanford, T. J., and Plattner, G.-K.: Contributions of stratospheric water vapor to decadal changes in the rate of global warming., *Science (New York, N.Y.)*, 327, 1219–23, <https://doi.org/10.1126/science.1182488>, 2010.
- Soo Lee, S., Kablick, G., Li, Z., Hoon Jung, C., Choi, Y. S., Um, J., and Jun Choi, W.: Examination of effects of aerosols on a pyroCb and their dependence on fire intensity and aerosol perturbation, *Atmospheric Chemistry and Physics*, 20, 3357–3371, <https://doi.org/10.5194/acp-20-3357-2020>, 2020.
- Stocks, B. J., Fosberg, M. A., Lynham, T. J., Mearns, L., Wotton, B. M., Yang, Q., Jin, J.-Z., Lawrence, K., Hartley, G. R., Mason, J. A., and Mckenney, D. W.: Climate Change and Forest Fire Potential in Russian and Canadian Boreal Forests, *Climatic Change*, 38, 1–13, 1998.
- Stuefer, M. and Gordon, T.: Cryogenic Frostpoint Hygrometer (CFH) Instrument Handbook, 2018.
- Survo, P., Lehtinen, R., and Kauranen, J.: SI traceability of Vaisala radiosonde RS41 sounding data- calibration and uncertainty analysis, pp. 6–9, 2014.

- Tarasick, D. W., Smit, H. G. J., Thompson, A. M., Morris, G. A., Witte, J. C., Davies, J., Nakano, T., Van Malderen, R., Stauffer, R. M., Johnson, B. J., Stübi, R., Oltmans, S. J., and Vömel, H.: Improving ECC Ozonesonde Data Quality: Assessment of Current Methods and Outstanding Issues, *Earth and Space Science*, 8, 1–27, <https://doi.org/10.1029/2019ea000914>, 2021.
- Taszarek, M., Allen, J. T., Groenemeijer, P., Edwards, R., Brooks, H. E., Chmielewski, V., and Enno, S. E.: Severe convective storms across Europe and the United States. Part I: Climatology of lightning, large hail, severe wind, and tornadoes, *Journal of Climate*, 33, 10 239–10 261, <https://doi.org/10.1175/JCLI-D-20-0345.1>, 2020.
- Thompson, A. M., Smit, H. G., Witte, J. C., Stauffer, R. M., Johnson, B. J., Morris, G., Von Der Gathen, P., Van Malderen, R., Davies, J., Piters, A., Allaart, M., Posny, F., Kivi, R., Cullis, P., Anh, N. T. H., Corrales, E., Machinini, T., DaSilva, F. R., Paiman, G., Thiong’o, K., Zainal, Z., Brothers, G. B., Wolff, K. R., Nakano, T., Stübi, R., Romanens, G., Coetzee, G. J., Diaz, J. A., Mitro, S., Mohamad, M., and Ogino, S. Y.: Ozonesonde quality assurance the josieshadowz (2017) experience, *Bulletin of the American Meteorological Society*, 100, 155–171, <https://doi.org/10.1175/BAMS-D-17-0311.1>, 2019.
- Trenberth, K. E., Dai, A., Rasmussen, R. M., and Parsons, D. B.: The changing character of precipitation, *Bulletin of the American Meteorological Society*, 84, 1205–1217+1161, <https://doi.org/10.1175/BAMS-84-9-1205>, 2003.
- Ummenhofer, C. C. and Meehl, G. A.: Extreme weather and climate events with ecological relevance: A review, *Philosophical Transactions of the Royal Society B: Biological Sciences*, 372, <https://doi.org/10.1098/rstb.2016.0135>, 2017.
- Vaisala: Radiosonde RS41-D, Tech. rep., 2020.
- Vömel, H., David, D. E., and Smith, K.: Accuracy of tropospheric and stratospheric water vapor measurements by the cryogenic frost point hygrometer: Instrumental details and observations, *Journal of Geophysical Research*, 112, <https://doi.org/10.1029/2006JD007224>, 2007.
- Vömel, H., Naebert, T., Dirksen, R., and Sommer, M.: An update on the uncertainties of water vapor measurements using cryogenic frost point hygrometers, *Atmospheric Measurement Techniques*, 9, 3755–3768, <https://doi.org/10.5194/amt-9-3755-2016>, 2016.
- Vömel, H., Smit, H. G., Tarasick, D., Johnson, B., Oltmans, S. J., Selkirk, H., Thompson, A. M., Stauffer, R. M., Witte, J. C., Davies, J., Van Malderen, R., Morris, G. A., Nakano, T., and

- Stübi, R.: A new method to correct the electrochemical concentration cell (ECC) ozonesonde time response and its implications for "background current" and pump efficiency, *Atmospheric Measurement Techniques*, 13, 5667–5680, <https://doi.org/10.5194/amt-13-5667-2020>, 2020.
- von Ehrenfried, M.: *Stratospheric Balloons*, Springer International Publishing, <https://doi.org/10.1007/978-3-030-68130-2>, 2021.
- Voss, H. D., Ramm, N. A., and Dailey, J.: *Understanding High-Altitude Balloon Flight Fundamentals*, 74, 74–83, URL <http://ukhas.org.uk/guides:balloon>.
- Wallace, J. M. and Hobbs, P. V.: *Atmospheric Science: An Introductory Survey*, Academic Press, 2006.
- Walsh, J. E., Ballinger, T. J., Euskirchen, E. S., Hanna, E., Mård, J., Overland, J. E., Tangen, H., and Vihma, T.: Extreme weather and climate events in northern areas: A review, *Earth-Science Reviews*, 209, 103324, <https://doi.org/10.1016/j.earscirev.2020.103324>, 2020.
- Wang, P. K.: Moisture plumes above thunderstorm anvils and their contributions to cross-tropopause transport of water vapor in midlatitudes, *Journal of Geophysical Research: Atmospheres*, 108, 1–15, <https://doi.org/10.1029/2002jd002581>, 2003.
- Waters, J. W., Froidevaux, L., Harwood, R. S., Jarnot, R. F., Pickett, H. M., Read, W. G., Siegel, P. H., Cofield, R. E., Filipiak, M. J., Flower, D. A., Holden, J. R., Lau, G. K., Livesey, N. J., Manney, G. L., Pumphrey, H. C., Santee, M. L., Wu, D. L., Cuddy, D. T., Lay, R. R., Loo, M. S., Perun, V. S., Schwartz, M. J., Stek, P. C., Thurstans, R. P., Boyles, M. A., Chandra, K. M., Chavez, M. C., Chen, G. S., Chudasama, B. V., Dodge, R., Fuller, R. A., Girard, M. A., Jiang, J. H., Jiang, Y., Knosp, B. W., Labelle, R. C., Lam, J. C., Lee, K. A., Miller, D., Oswald, J. E., Patel, N. C., Pukala, D. M., Quintero, O., Scaff, D. M., Van Snyder, W., Tope, M. C., Wagner, P. A., and Walch, M. J.: The Earth Observing System Microwave Limb Sounder (EOS MLS) on the aura satellite, *IEEE Transactions on Geoscience and Remote Sensing*, 44, 1075–1092, <https://doi.org/10.1109/TGRS.2006.873771>, 2006.
- Watson, K. M.: *Thermodynamics of the Liquid State: Generalized Prediction of Properties*, *Industrial and Engineering Chemistry*, 35, 398–406, 1943.
- Weber, U. and Schuetze, C.: MOSES: A novel observing system for highly dynamic events, in: *EGU General Assembly Conference Abstracts*, *EGU General Assembly Conference Abstracts*, p. 13650, 2019.

- Weinstock, E. M., Pittman, J. V., Sayres, D. S., Smith, J. B., Anderson, J. G., Wofsy, S. C., Xueref, I., Gerbig, C., Daube, B. C., Pfister, L., Richard, E. C., Ridley, B. A., Weinheimer, A. J., Jost, H. J., Lopez, J. P., Loewenstein, M., and Thompson, T. L.: Quantifying the impact of the North American monsoon and deep midlatitude convection on the subtropical lowermost stratosphere using in situ measurements, *Journal of Geophysical Research Atmospheres*, 112, 1–16, <https://doi.org/10.1029/2007JD008554>, 2007.
- Werner, F., Schwartz, M. J., Livesey, N. J., Read, W. G., and Santee, M. L.: Extreme Outliers in Lower Stratospheric Water Vapor Over North America Observed by MLS: Relation to Overshooting Convection Diagnosed From Colocated Aqua-MODIS Data, *Geophysical Research Letters*, 47, <https://doi.org/10.1029/2020GL090131>, 2020.
- Whidou: Conceptual vertical cross-section of a trailing stratiform Mesoscale convective storm flow structure:, URL <https://commons.wikimedia.org/w/index.php?curid=38535781>, 2015.
- Wiegleb, G.: Feuchtemessung in Gasen, pp. 575–624, Springer Fachmedien Wiesbaden, Wiesbaden, https://doi.org/10.1007/978-3-658-10687-4_10, 2016.
- Wilhelm, J., Mohr, S., Punge, H. J., Mühr, B., Schmidberger, M., Daniell, J. E., Bedka, K. M., and Kunz, M.: Severe thunderstorms with large hail across Germany in June 2019, *Weather*, pp. 228–237, <https://doi.org/10.1002/wea.3886>, 2020.
- WMO: Atmospheric ozone 1985, 1985.
- Yu, P., Toon, O. B., Bardeen, C. G., Zhu, Y., Rosenlof, K. H., Portmann, R. W., Thornberry, T. D., Gao, R.-s., Davis, S. M., Wolf, E. T., Gouw, J. D., and Peterson, D. A.: Persistent Plume, 590, 587–590, 2019.
- Zahn, A., Brenninkmeijer, C. A. M., and Velthoven, P. F. J. V.: Passenger aircraft project CARIBIC 1997–2002, Part I: the extratropical chemical tropopause, *Atmospheric Chemistry and Physics Discussions*, 4, 1091–1117, <https://doi.org/10.5194/acpd-4-1091-2004>, 2004.
- Zahn, A., Christner, E., Velthoven, P. F. J., and Brenninkmeijer, C. A. M.: Processes controlling water vapor in the upper troposphere/lowermost stratosphere: An analysis of 8years of monthly measurements by the IAGOS-CARIBIC observatory, *Journal of Geophysical Research: Atmospheres*, 175, 238, <https://doi.org/10.1038/175238c0>, 2014.

Appendix A

Theory of balloon-launching operations and buoyancy

In order to understand how much Helium has to be filled in to the balloon one has to consider the concept of buoyancy already mentioned in Chapter 2. Equation 2.2 shows buoyancy in dependence of temperature, as for ambient tropospheric air temperature governs the density of the air following the general gas equation:

$$p \cdot V = n \cdot R \cdot T \quad (\text{A.1})$$

which equals to

$$p = \rho \cdot R_s \cdot T \quad (\text{A.2})$$

where p is pressure, V is volume, n is the amount of substance in units of mol, R is the general gas constant and R_s is the specific gas constant, T is temperature and ρ is the density. Given the same volume of a gas, the driving difference between two gases at the same pressure and temperature is the density. Hence, one can define buoyancy as:

$$F_B = (m_a - m_g) \cdot g \quad (\text{A.3})$$

with g being the acceleration of gravity, m_a the mass of air per cubic meter and m_g the mass of helium per cubic meter. The force pulling the balloon down can be accounted for with the mass of the balloon itself as well as the payload attached to the balloon m_G . The force which moves the

balloon upwards can then be described as the buoyancy force F_L as:

$$F_L = F_B - (m_G \cdot g). \quad (\text{A.4})$$

Another force acting on the balloon is the friction force of the air surrounding the balloon, also called the drag force F_D .

$$F_D = \frac{1}{2} \cdot C_D \cdot A_b \cdot \rho_a \cdot v^2 \quad (\text{A.5})$$

where C_D is the drag constant ($= 0.3$ for the balloon), A_b is the aerial cross section of the balloon with $A_b = \pi \cdot (D^2/4)$ (with D being the diameter of the balloon), ρ_a is the density of the ambient air and v the vertical velocity. For a steady state between the buoyancy force and the drag force one

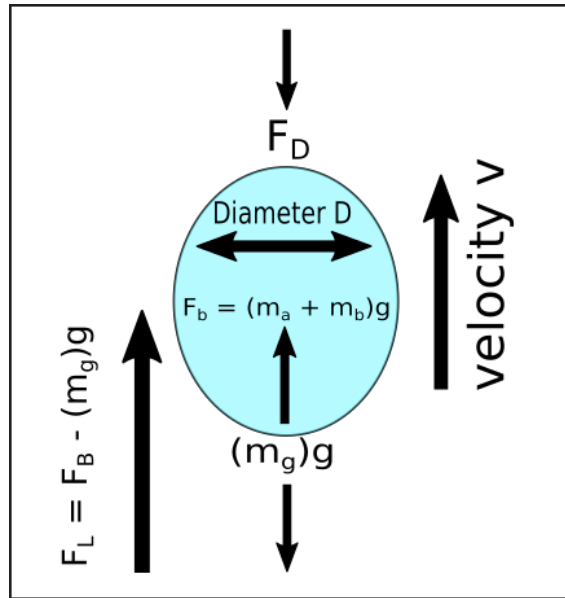


Figure A.1: schematic of forces acting on a weather balloon.

can solve in respect of velocity v of the balloon, using equations A.3, A.4 and A.5 as well as the definition of the volume of the balloon $V_B = 1/6\pi D^3$ and the definition of the density $\rho = m/V$, and derive following formula:

$$v = \sqrt{\frac{\pi D^3 (\rho_a - \rho_b) \frac{g}{6} - (m_B + m_p)g}{C_D \rho_a \pi \frac{D^2}{8}}} \quad (\text{A.6})$$

with ρ_b being the density of the gas inside the balloon. Figure A.1 schematically illustrates the forces. Accordingly, in order to adjust the ascending speed of the balloon, assuming a known mass of the payload, the diameter of the balloon before launch has to be calculated and the

appropriate amount of gas has to be filled (Voss et al.). The most frequently used balloon start is performed using 150 g - 200 g rubber balloons with a radiosonde attached in a 20 m - 50 m distance to the balloon. The radiosonde has a weight of 100 g - 200 g in dependence on the manufacturer. Assuming a balloon launch with a 200 g balloon and a 150 g payload and a desired ascend rate of 5 m/s, 125 g of Helium would be needed. In the field however, it might be easier to use the free lift F_L in order to define the right amount of gas which has to be filled into the balloon.

Appendix B

Supplements for Chapter 3

The following figures are supplementary material for Chapter 3.

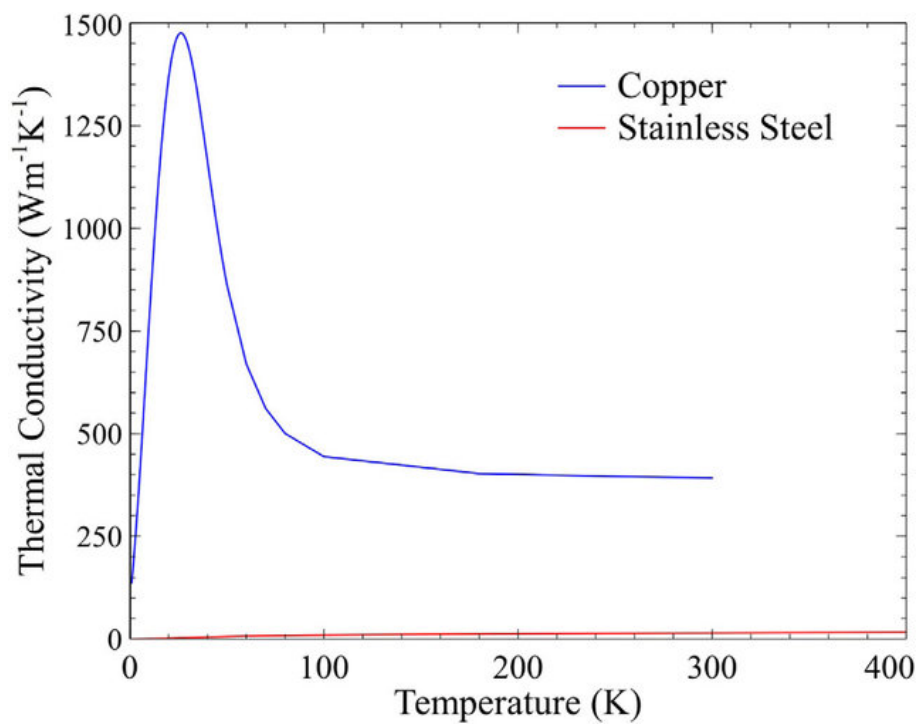


Figure B.1: Dependence of thermal conductivity of copper on temperature (Ravikumar et al., 2017).

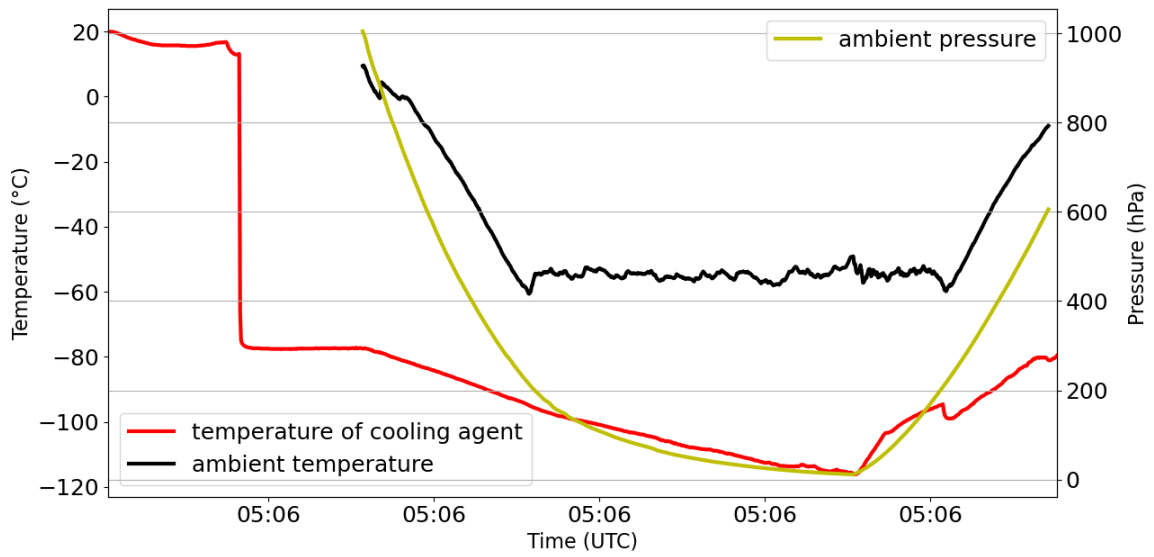


Figure B.2: Temperature of the new cooling agents during the flight on the 25 April 2020. The temperature of the ethanol-CO₂ mixture is given in red. The ambient temperature is given in black and the pressure in yellow.

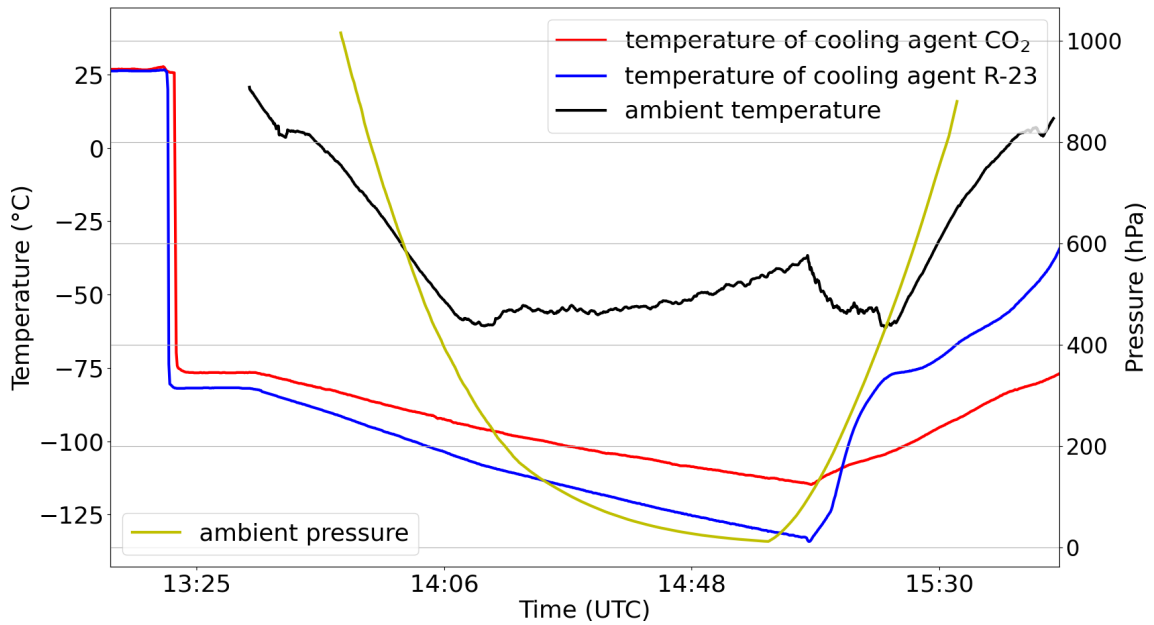


Figure B.3: Temperature of both cooling agents during the flight on the 22 June 2020. The temperature of the ethanol-CO₂ mixture is given in red, the temperature of the R23 is given in blue. The ambient temperature is given in black and the pressure in yellow.

Appendix C

Supplements for Chapter 4

The following figures are supplementary materials for Chapter 4.

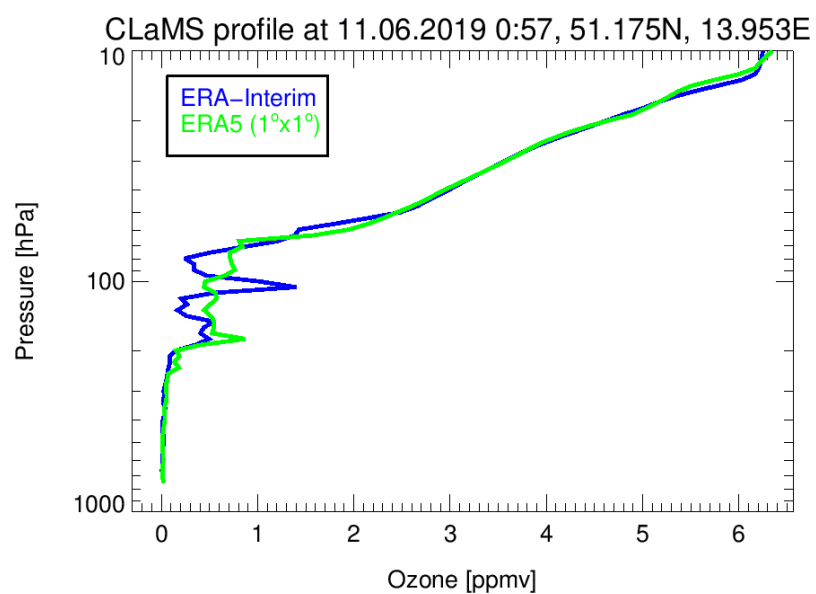


Figure C.1: Ozone enhancement in the CLaMS model driven with ERA5 (green) and ERA-interim (blue) interpolated at the time and location of the balloon measurement.

Appendix D

Supplements for Chapter 5

The following figures are supplementary materials for Chapter 5.

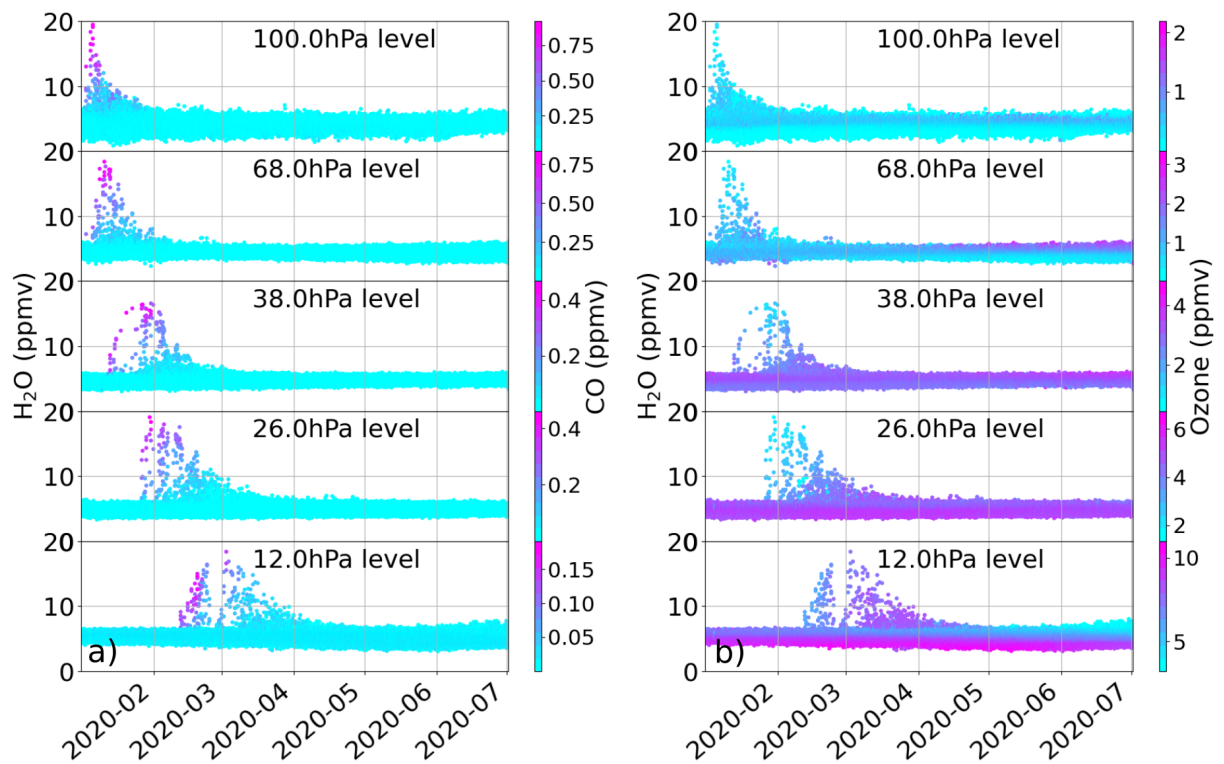


Figure D.1: Water vapor mixing ratios in 2020 in the SH with a) CO and b) ozone color-coded with the focus on the water vapor enhancement caused by ANYSO.

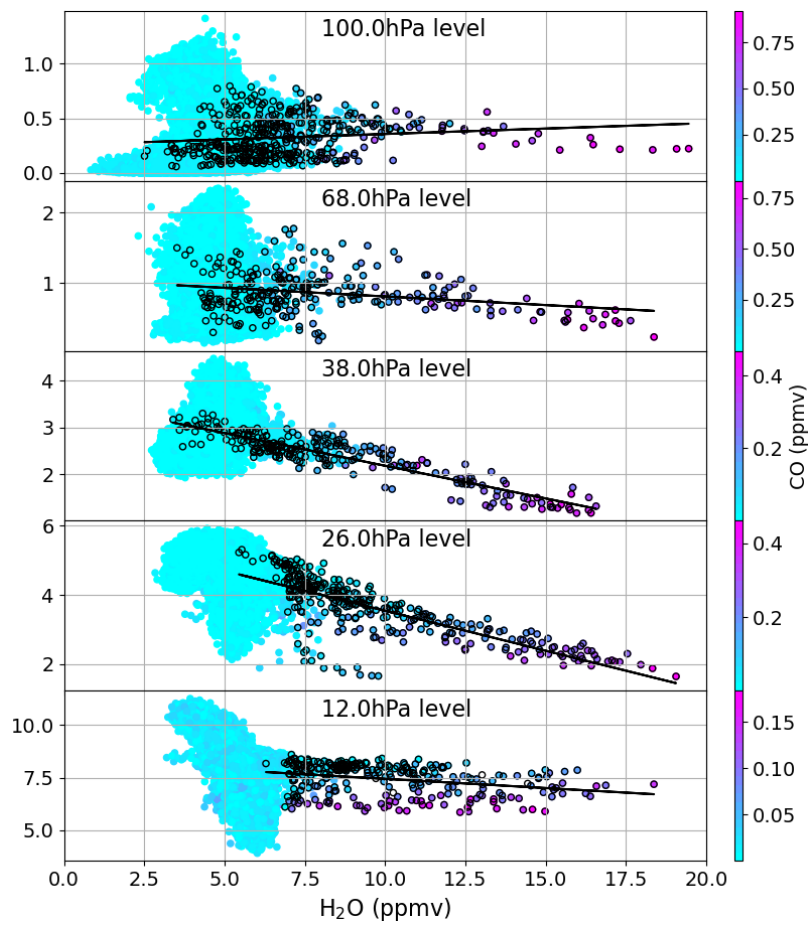


Figure D.2: Same as Fig. 5.2 but for the pressure levels 26 and 12 hPa water vapor was used as identification tracer as described in Section 5.1.1.

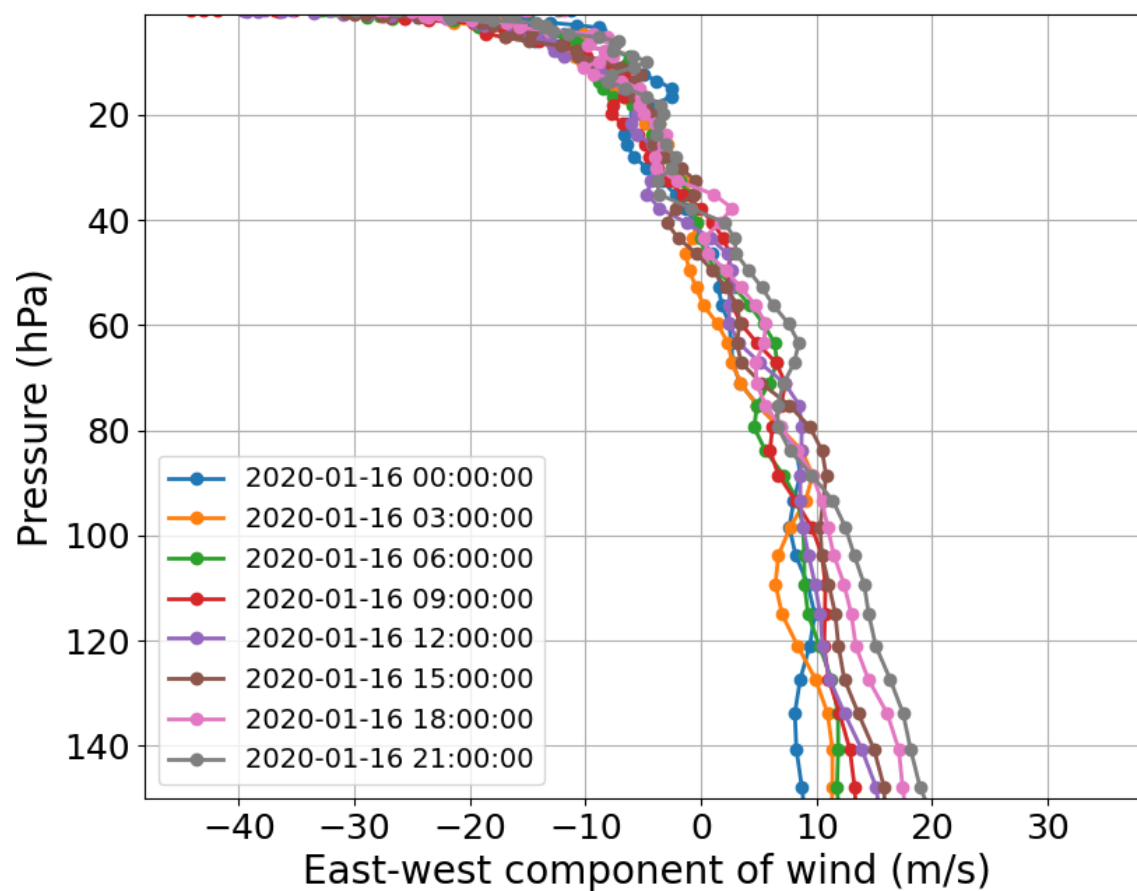


Figure D.3: Profile of the east-west wind component exemplary on the 16 January 2020 at 60°S and 70°W between pressures of 200 and 0.01 hPa from ECMWF ERA5 data.

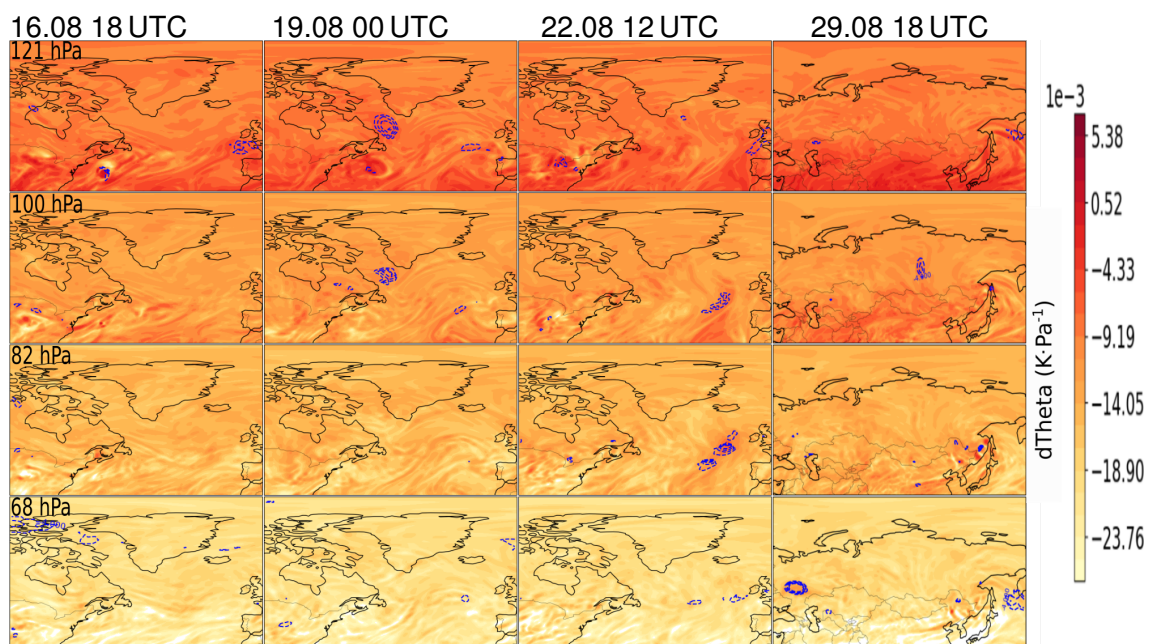


Figure D.4: ERA5 $d\Theta$ data with PV anomaly as contour lines between 16 and 29 August 2017 for the BC2017 case.

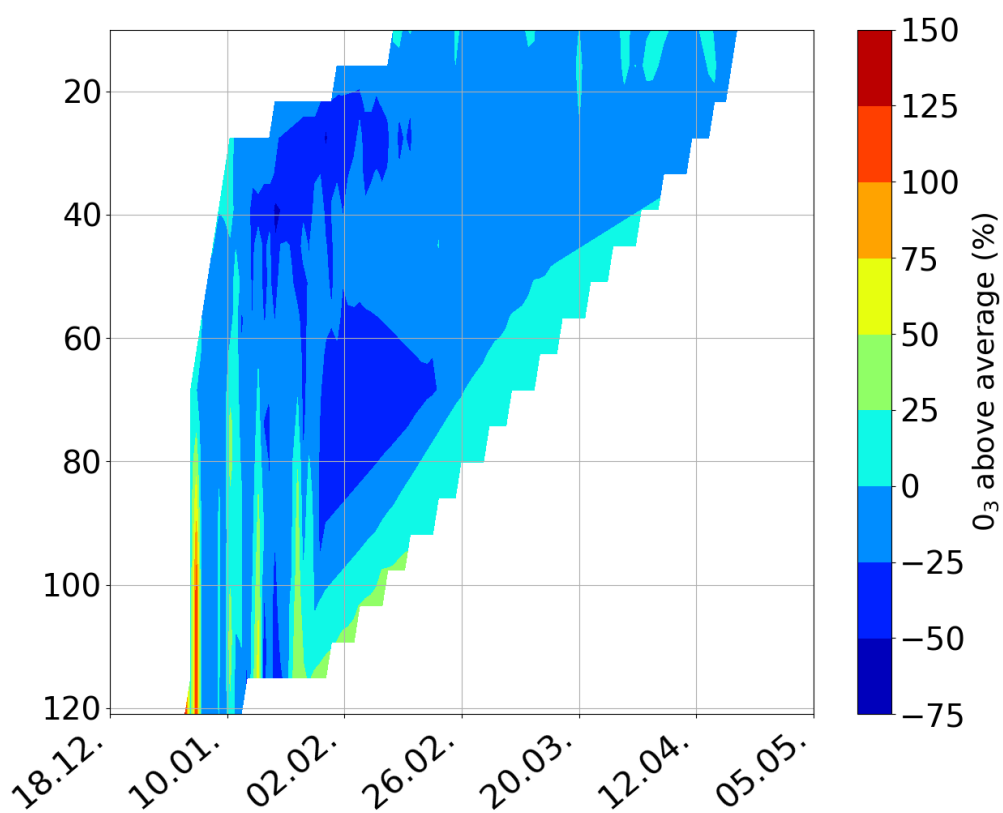


Figure D.5: Vertical distribution of changes in the ozone mixing ratios compared to the average at the respective latitude in the ANYSO plume, as measured by MLS.

Acknowledgments

After completing this work, I would like to thank multiple people who played a significant role for the completion of this work in various ways. First of all, I would like to thank my supervisor Christian Rolf, who played the major role for the initiation and completion of this work. I had the extraordinary luck to start my PhD project with a fully planned and organized work schedule and already settled campaign plan which were both very realistic and structured. I was always fully supported by my supervisor and he always had open doors for all my questions and concerns. He guided me through the preparation of the Khordakova et al. (2022) paper as well as this thesis, and took the time to precisely direct me into the right direction. I would also like to thank the entire 'water vapor and clouds' working group for practical support throughout the work, as well as the entire IEK-7 staff for a pleasant and supportive environment where everyone is open to questions and was happy to discuss any scientific questions I had. Here, I would especially like to thank Prof. Martin Riese for the work at the institute and reviewing the publication and this thesis. I also thank Dr. Rolf Müller, Dr. Paul Konopka and Dr. Jens-Uwe Grooß for the active participation and discussion over upcoming questions during this work.

I further would like to thank the Helmholtz Association for the possibility to work within the MOSES framework in collaboration with multiple other Helmholtz-research centers. Particularly, I would like to thank the members of the KIT-TRO group of the "Karlsruher Institute für Technologie", and especially Martin Kohler and Dr. Andreas Wieser, for consistent support during the measurement campaign at any time of the day. Here, I would also like to separately mention my gratitude to Dr. Inga Melnyk and Dr. Maximilian Seuß for a spontaneous hands-on support during a night-time measurement, which later turned out to be the basis for a central part of this work. Great thanks also go to Dr. Inga Melnyk, Dr. Jonas Bühler and Fanny Wischnewski for the attentive proofreading of this thesis and the redistribution of many commata.

Additionally, I would like to thank HITEC for the useful seminars on soft-skills in scientific work, as well as the built up of a network which led to lots of amusing but also fruitful discussions

between the participants. This network also led to multiple friendships and adventures which formed valuable memories. Many thanks go to my friends and family who always supported and encouraged me, and accompanied me on the journey to finishing this thesis.